

Politecnico di Torino

Master of Science in Energy and Nuclear Engineering A.y. 2024/2025 Graduation Session October 2025

Thermal-Hydraulic Benchmarking:

A Comparative Study between DASSH and CFD

Supervisors: Candidate:

Raffaella Testoni Matteo Credito Antonio Froio

Abstract

Designing the core of a nuclear reactor requires a continuous interaction between neutronics and thermal-hydraulics due to their intrinsic coupling. In neutronics, the neutron fluence rate determines the distribution of fission power inside the core, which in turn affects the fuel temperature and ultimately the entire temperature field. Conversely, thermodynamic parameters from thermal-hydraulics strongly influence cross sections, impacting the neutron flux distribution. This mutual dependence necessitates iterative coupling between the two analyses to achieve consistent and physically accurate results.

Accurate and reliable thermal-hydraulic codes are essential for predicting reactor behavior, ensuring effective heat removal, and maintaining safe operation. These codes provide sufficient fidelity to capture complex thermal phenomena within reactor cores while remaining computationally efficient, thereby supporting iterative reactor core design processes.

Among the available tools, the Ducted Assembly Steady-State Heat Transfer Software (DASSH), developed at Argonne National Laboratory, is a finite-volume, first-order subchannel code designed to perform steady-state coolant and fuel pin temperature calculations for full reactor cores composed of hexagonal ducted assemblies.

In this study, DASSH is benchmarked against Computational Fluid Dynamics (CFD) simulations. Meaningful benchmarking requires accurate representation of inter-assembly heat transfer, a phenomenon that strongly affects subchannel temperature distributions. While DASSH employs modeling assumptions to reduce computational expense, its predictive capability is carefully evaluated using CFD as a reference to quantify accuracy and uncertainties.

The benchmarking highlights the current capabilities and limitations of DASSH, providing insights into its applicability and guiding potential improvements for future development.

Acknowledgements

Throughout this year, I have been fortunate to have many people accompany me on my journey. Some stayed from the beginning, some joined in the middle, and some came and went. To all of them, I am deeply grateful.

First and foremost, I want to thank my family—my mother and father—for their patience, for tolerating my temperament, and for always giving me the freedom to make my own choices while believing in me. I am also grateful to my close relatives, who, despite seeing me only occasionally, always show joy and warmth when we meet and spend time together.

I would like to thank my friends who have made this journey memorable. In particular, my university colleagues, many of whom have become close friends, especially the group "I Tarallini Toroidali," with whom I shared both happy and challenging moments throughout the year. To my roommates in Turin, thank you for the laughter and unforgettable experiences—I will surely miss them.

I also want to thank my brothers in life, Chri and Ri, who, even though life has taken us on different paths at times, have always been there from day one. To my friends from Gavi and nearby towns, with whom I grew up, thank you for the joy of returning home and enjoying life together in the countryside. To all my other friends, whether mentioned or not, if you have cared about me and shared part of this journey with me, please know that you are in my thoughts and included in these thanks—you have been an important part of my journey.

I am also deeply grateful to my professors, especially my supervisor, for giving me the opportunity to undertake this thesis and for all the guidance and support provided along the way.

Lastly, I want to thank myself—for believing in me, for working hard, for persevering even on difficult days, for striving to give more than I receive, for trying to do what is right, and for simply being myself.

Table of Contents

Li	st of	Figur	es	IV
Li	st of	Table	${f s}$	VI
A	crony	yms		VII
1	Intr	oduct	ion	1
2	SFI	R: Con	cepts, Evolution and Prospects	6
	2.1	Gener	ration IV reactors	6
	2.2	Histor	rical SFR Design Concepts	9
		2.2.1	EBR-II	10
		2.2.2	The French Trilogy: RAPSODIE, PHÉNIX and SUPER-	
			PHÉNIX	
		2.2.3	Worldwide SFRs experience	
	2.3	Curre	nt State and Future Prospects	
		2.3.1	The ABR-1000: design, objective and roadmap	
		2.3.2	Status and outlook of SFR programs in Europe and Asia	32
3	$Th\epsilon$		Hydraulic Modeling of DASSH	40
	3.1	System	m description	40
	3.2	Physic	cs Modeled in DASSH	
		3.2.1	Energy conservation law	
		3.2.2	Correlation built in DASSH	
		3.2.3	Duct walls treatment	
		3.2.4	Numerical stability	
		3.2.5	Energy balance modeling	
	3.3		earison with CFD: Advantages and Limitations	
		3.3.1	Fundamental Differences Between DASSH and CFD	
		$3\ 3\ 2$	Limitations	58

4	Ben	chmar	king of DASSH: Case Studies	60
	4.1	Case S	Study 1	60
		4.1.1	System Description	60
		4.1.2	DASSH model	64
		4.1.3	STAR CCM+ model	65
		4.1.4	Results	70
		4.1.5	Conclusion	76
	4.2	Case S	Study 2	77
		4.2.1	Fuel Assembly Description	78
		4.2.2	DASSH Model	79
		4.2.3	STAR-CCM+ Model	80
		4.2.4	Results	84
5	Con	clusio	ns	88
Bi	bliog	graphy		90

List of Figures

1.1	Possibles approaches path to thermal hydraulic analysis[2]	4
2.1	Schematic diagrams of the six Generation IV reactor concepts[3]	9
2.2	EBR-II reactor design[7]	12
2.3	EBR-II primary tank flow path sketch[6]	13
2.4	Core assemblies arrangement	14
2.5	Sample MARK-II Subassembly Configuration	16
2.6	Mark-II assembly elevation section	18
2.7	Phénix reactor vessel scheme[9]	20
2.8	General layout of the PHÉNIX reactor core[10]	21
2.9	Plant overview of the ABR-1000	28
2.10	ABR-1000 primary system	29
2.11	ABR-1000 core layout	30
2.12	Internal layouts of ABR-1000 metal and oxide fuel assemblies	32
3.1	Dimensions and definitions applied to single-ducted assembly	41
3.2	Inter-assembly gap subchannel configuration and indexing	43
3.3	Subchannel adjacency for interior-type subchannels, for the other	
0.4	types the approach is the same.	43
3.4	Two distinct coolant flow regions in a hexagonal ducted assembly:	4.0
0.5	interior pin bundle and peripheral duct region	46
3.5	Summary of DASSH Correlations [22]	51
3.6	Disagreement in meshing schemes between neighboring assemblies .	53
4.1	Temperature-dependent sodium properties compared with the con-	
	stant reference values used in the study. The equation used are the	
	$4.13,4.14, 4.15 \text{ and } 4.16 \ldots \ldots \ldots \ldots \ldots \ldots$	62
4.2	Thermal conductivity profile depending on temperature	64
4.3	Overview of the resulting mesh	67
4.4	Mesh focus	68
4.5	Outlet temperature distribution obtained with DASSH	71

4.6	Outlet temperature distribution obtained with STAR-CCM+	71
4.7	Outlet temperature distribution in assembly 1 obtained with DASSH.	72
4.8	Outlet temperature distribution in assembly 2 obtained with DASSH.	72
4.9	Outlet temperature distribution in assembly 1 obtained with CFD.	73
4.10	Outlet temperature distribution in assembly 2 obtained with CFD.	73
4.11	Axial temperature profile along the assemblies obtained with STAR-	
	CCM+	76
4.12	Applied parabolic power distribution along the active core length	79
4.13	Mesh of the fuel assembly used for CFD simulations	81
4.14	Front mesh result	81
4.15	Detailed view of the prism layer mesh	82
4.16	Outlet temperature distribution predicted by DASSH	84
4.17	Outlet temperature distribution predicted by STAR-CCM+	85
4.18	Comparison of temperature profiles at heights of 2.058 m, 2.693 m,	
	and 3.327 m	86

List of Tables

2.1	Design Parameters of EBR-II Subassembly Elements at 20 °C	17
2.2	ABR-1000 Main Design Parameters	27
2.3	Comparison of Subassembly Design Parameters for ABR-1000[18] .	31
2.4	Historical Sodium-Cooled Fast Reactor Programs (Part 1)	35
2.5	Historical Sodium-Cooled Fast Reactor Programs (Part 2)	36
2.6	SFR projects currently operating	37
2.7	SFRs under development	38
4.1	Geometric parameters for Type 1 and Type 2 assemblies	61
4.2	Thermophysical properties of sodium and HT9	61
4.3	Meshing parameters for the inlet region	67
4.4	Grid independence results for the first case study	68
4.5	Grid convergence and extrapolated results for the first case study .	70
4.6	DASSH outlet temperature	74
4.7	Case study comparison of outlet temperatures	75
4.8	Case study comparison of inter-assembly heat transfer	75
4.9	Midplane temperature comparison between DASSH and CFD	75
4.10	Midplane heat transfer comparison between DASSH and CFD	76
4.11	Main geometrical features of the selected fuel assembly	78
4.12	Grid independence results	82
4.13	Results for grid independence analysis (directed mesh, h_{char} considered)	84
4.14	Comparison of outlet temperature results between DASSH and CFD	
	(STAR-CCM+)	85

Acronyms

ABR

Advanced Burner Reactor

ANL

Argonne Natioanl Laboratory

ARC

Argonne Reactor Computation

BN

Bystrie neytrony (Fast Neutron)

CEA

French Alternative Energies and Atomic Energy Commission

CEFR

China Experimental Fast Reactor

CFD

Computational Fluid Dynamics

CFR

China Fast Reactor

DASSH

Ducted Assembly Steady-State Heat Transfer Software

DNS

Direct Numerical Simulation

DOE

United State Department of Energy

DRACS

Direct Reactor Auxiliary Cooling System

EBR

Experimental Bredeer Reactor

EURATOM

European Atomic Energy Community

FBTR

ast Breeder Test Reactor

GFR

Gas-cooled Fasr Reactor

GIF

Generation IV International Forum

GNEP

Global Nuclear Energy Partnership

IFR

Integral Fast Reactor

IHX

Intermediate Heat Exchanger

INCOT

In-Core instrument Test

INSAT

Instrumented Subassembly Test

LES

Large Eddy Simulation

LFR

Lead-cooled Fast Reactor

LMFR

Liquid Metal Fast Reactor

LWR

Light Water Reactor

MOX

Mixed-OXide

MSR

Molten Salt Reactor

PFBR

Prototype Fast Breeder Reactor

RANS

Reynolds Averaged Navier-Stokes

SCWR

 ${\bf Super Critical\text{-}Water\text{-}cooled\ Reactor}$

\mathbf{SFR}

Sodium-cooled Fast Reactor

SHRT

Shutdown Heat Removal Test

SMFR

Small Modular Fast Reactor

SST

Shear Stress Transport

TRISO

TRi-structural ISOtropic particle fuel

\mathbf{VHTR}

 $\label{temperature reactor} Very-high-temperature\ reactor$

VTR

Versatile Test Reactor

Chapter 1

Introduction

A thorough understanding of the thermohydraulic behavior of fuel pins and assemblies under both steady-state and transient conditions is essential for the safe and stable operation of nuclear reactors. Thermohydraulic analysis is an important aspect of nuclear power plant evaluation, which includes the prediction of reactor core behavior, characterization of temperature distributions, assessment of hydraulic properties, and determination of operational and peak power levels of fuel assemblies. A key challenge lies in demonstrating that, under all operating conditions, the thermal and mechanical parameters of the coolant and structural materials remain within safe and acceptable limits, which is fundamental for reliable long-term operation.

Achieving this level of insight requires extensive experimental and theoretical investigations into core thermohydraulics. Over the past decade, significant progress has been made in the thermohydraulic design and operation of Liquid Metal Fast Reactors (LMFRs) in countries with active fast reactor programs, improving safety, reliability, and performance. Among LMFRs, Sodium-cooled Fast Reactors (SFRs) have obtained particular attention due to the unique thermohydraulic properties of liquid sodium. Its high thermal conductivity and low density enable efficient heat removal and high power density, making SFRs a promising technology for advanced nuclear systems. Understanding the thermohydraulic behavior of nuclear reactor cores is therefore essential for optimizing design, ensuring safety, and managing transient scenarios effectively.

The development of thermohydraulic simulation tools for fast reactors requires a deep understanding of their unique design, technological, and physical characteristics. These considerations are integral to the formulation of accurate and reliable computational methodologies capable of capturing the complex flow and heat transfer phenomena occurring within the reactor core:

• Design features: Fast reactor cores are primarily composed of a central fuel

region and surrounding blanket zones, both arranged using hexagonal fuel assemblies. Each subassembly typically consists of a tightly packed array of fuel pins, often configured as a triangular lattice. The presence of helical wire wraps around the fuel pins introduces a helical motion to the coolant, promoting enhanced mixing and the formation of preferential flow paths. This geometric feature, while beneficial for thermal performance, adds complexity to the prediction of local flow distributions. Additionally, small gaps between adjacent assemblies allow cross-flow, further complicating the flow dynamics within the core. Spatial variations in local thermohydraulic behavior can occur as a result of the different types of assemblies which characterize the core.

- Technological features: Fast reactors typically employ liquid metal coolants such as sodium or lead, which are characterized by a low specific heat capacity and high thermal conductivity. These properties result in a rapid increase in the coolant temperature, but only a minimal temperature gradient across the fuel pin cladding. Although advantageous for efficient heat removal, these characteristics require precise modeling to ensure safe thermal margins.
- Physical features: Power generation within the core is highly non-uniform and influenced by several factors, including the configuration of the fuel zones, the presence of blankets and shielding materials, the geometry of the reactor, and the status of reactivity control systems. To achieve a robust thermohydraulic prediction of assembly behavior, computational models must account for a range of core-specific complexities such as inter, edge and corner subchannel exchange of mass, momentum and energy, complex internal geometry, mechanical deformations, heat transfer inducing axial and radial power gradients, boundary conditions, sensitivity of input parameters and uncertainties.

Generally, thermohydraulic analysis of fuel pin bundles can be categorized into three distinct methodological families, each offering a different level of detail and complexity as showed in Figure 1.1:

- 1. Local numerical approach. It is based on solving the full system of differential equations, typically in the Reynolds-averaged form, to directly predict local flow and thermal features within the assembly. From these local results, integral parameters such as friction factor and heat transfer coefficient can be evaluated. These methods offer high spatial resolution but require detailed geometric modeling of the pin bundle, making them computationally demanding. As a result, they are often restricted to simplified steady-state conditions in simple smooth bundles.
- 2. Subchannel numerical approach. This kind of analysis operates at the scale of the coolant channels formed between neighboring fuel pins. It resolves key

hydrodynamic and thermal phenomena at a finer level than porous models but avoids the full complexity of local methods. The computational domain aligns with the actual subchannel geometry, allowing the prediction of average coolant velocities and temperatures in each channel. It provides a practical balance between accuracy and computational cost, and is widely used for core design and safety evaluations. It is able of capturing macro scale phenomena in reference to the subchannels while still describes micro scale effects related to bundle dimension.

3. Porous body model numerical approach. It provides a macroscopic representation of flow and heat transfer by averaging over scales significantly larger than those of individual subchannels. This result in lower spatial resolution which, however, enables the capture of large-scale, macro effects. It is suited for describing overall core behavior.

The main thermohydraulic codes currently under development are primarily intended to model subchannel characteristics, particularly during the early stages of reactor design, when many features are subject to continuous modification due to iterative development processes. In contrast, local approaches are mainly employed after the reactor design has been rigorously finalized, to gain a detailed understanding of the physical phenomena expected to occur within the reactor core. In this context, the Ducted Assembly Steady-State Heat Transfer (DASSH) code, currently under development at Argonne National Laboratory (ANL) and very promising, is intended to perform full-core, steady-state subchannel temperature calculations for reactors composed of ducted assemblies with wire-wrapped rod bundles. Designed to succeed the earlier SE2ANL code, DASSH introduces significant improvements in both accuracy and usability. It is being developed to integrate with the Argonne Reactor Computation (ARC) code system, where neutron and gamma heating data are provided by the transport code, DIF3D-VARIANT[1].

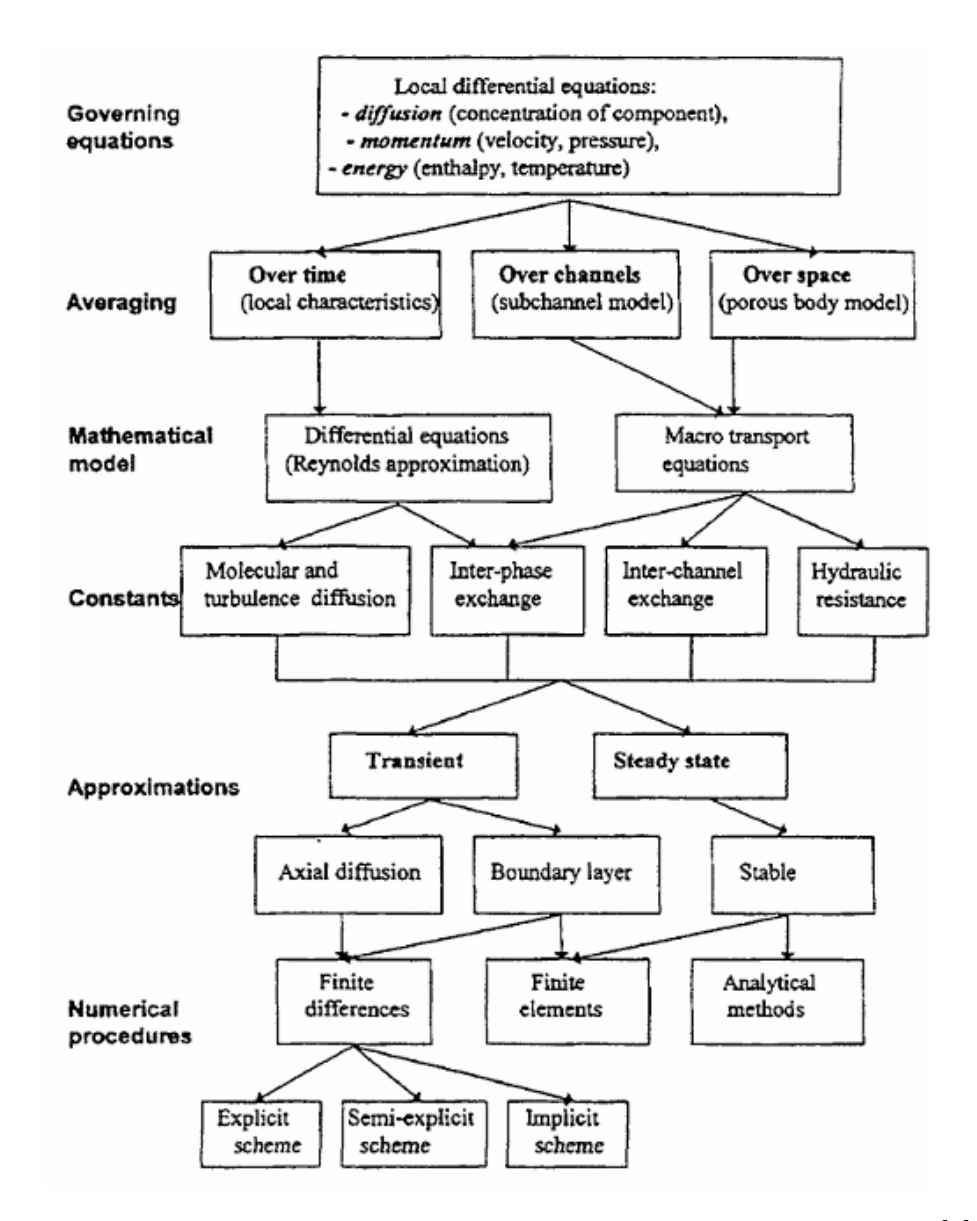


Figure 1.1: Possibles approaches path to thermal hydraulic analysis[2].

This thesis focuses on benchmarking DASSH to predict reactor behavior and assess its reliability for liquid metal reactors thermal-hydraulic analyses. Heat transfer between assemblies can be significant in reactors cooled by liquid metals or other high-conductivity coolants, particularly when strong temperature gradients are present. Accurate modeling of these effects is essential to ensure reliable predictions, especially for advanced Generation IV reactor designs.

Generation IV reactors often use liquid metal coolants such as sodium to achieve high thermal efficiency and enhanced safety. The high thermal diffusivity can amplify numerical diffusion effects, making careful validation and benchmarking of simulation tools critical for future reactor applications. This work compares DASSH predictions with those of STAR-CCM+ under steady-state conditions, highlighting the strengths, limitations, and overall reliability of DASSH for thermal-hydraulic analyses.

Chapter 2 introduces SFRs, emphasizing their historical development, worldwide deployment, and features. Chapter 3 provides an in-depth overview of DASSH, covering its physical models, numerical methods, and computational capabilities, laying the foundation for its application and verification. Chapter 4 presents the case study used for the benchmarking, comparing DASSH results with STAR-CCM+for software reliability. Finally, Chapter 5 summarizes the main findings, discusses the implications of the benchmarking study, and provides recommendations for future applications and improvements of DASSH.

Chapter 2

SFR: Concepts, Evolution and Prospects

With the aim of introducing revolutionary technology to improve fuel efficiency, minimize waste generation, enhance economic competitiveness, and adhere to rigorous safety and proliferation resistance standards, the fourth generation of nuclear reactors aspires to transform the nuclear energy sector over the next decade. These advancements focus on the following key areas:

- Sustainability: Energy generation must meet clean air targets and ensure the long-term availability of systems. Effective fuel utilization is essential to minimize nuclear waste and manage remaining waste in long-term repositories, ensuring protection for both people and the environment.
- Economics: Generation IV technologies must offer cost advantages and lower financial risk compared to other energy sources.
- Safety and reliability: High safety standards are expected through the implementation of passive safety systems, system redundancy, and other robust safety measures.
- Proliferation Resistance and Physical Protection: It is critical that these systems are unattractive for proliferation purposes and are well-protected against potential terrorist threats.

2.1 Generation IV reactors

In this context, the Generation IV International Forum (GIF), a cooperative international organization, brings together 13 countries (Argentina, Australia, Brazil,

Canada, China, France, Japan, South Korea, Russia, South Africa, Switzerland, United Kingdom, and United States), along with EURATOM, to collaborate on the development of the next generation of nuclear reactors. As part of its efforts, GIF has identified six reactor technologies as candidates for Generation IV nuclear reactors, with commercial deployment expected to begin around 2030:

• Sodium-cooled Fast Reactor.

The SFR is one of the most mature Generation IV designs, with a significant history of experimental and prototype reactors. It uses liquid sodium as a coolant and operates at atmospheric pressure, which eliminates the need for high-pressure containment systems. Sodium's excellent thermal conductivity and high boiling point (883°C) allow for high power density and efficient heat removal with relatively low flow rates. Designs include both pool-type and loop-type layouts. The typical outlet temperature is around 550°C, achieving a thermal efficiency of approximately 40%. It supports a closed fuel cycle and can function as a breeder reactor, generating more fissile material than it consumes. Reactor sizes up to 1500 MW_e are under development, and several prototypes are already in operation.

• Gas-cooled Fast Reactor.

GFR uses helium gas as a coolant and operates with a fast neutron spectrum and a closed fuel cycle. It achieves outlet temperatures of up to 850° C, making it well-suited for hydrogen production through thermochemical water splitting or high-temperature electrolysis. The reactor operates at a primary pressure of 7 MPa with a thermal efficiency of about 43%. Two reference designs are under consideration: a $600~MW_{\rm th}$ small-scale reactor and a $2400~MW_{\rm th}$ larger version to meet breeding break-even requirements.

• Lead-cooled Fast Reactor.

The LFR uses molten lead or lead-bismuth eutectic as coolant and operates in the fast neutron spectrum at atmospheric pressure. It is compatible with a closed fuel cycle and can serve as both a breeder and a minor actinide burner, contributing to waste minimization. Various reactor sizes are under consideration. The typical outlet temperature is around 550°C.

• Molten Salt Reactor.

In MSRs, nuclear fuel is dissolved in a circulating molten salt mixture typically fluorides of light metals and actinides. The design allows operation at atmospheric pressure and enables high thermal energy storage capacity. MSRs are highly adaptable, capable of operating in both thermal and fast neutron spectra, with closed fuel cycle options and breeding capabilities. The reference design produces approximately $1000\ MW_e$ with an outlet temperature of about $700^{\circ}\mathrm{C}$.

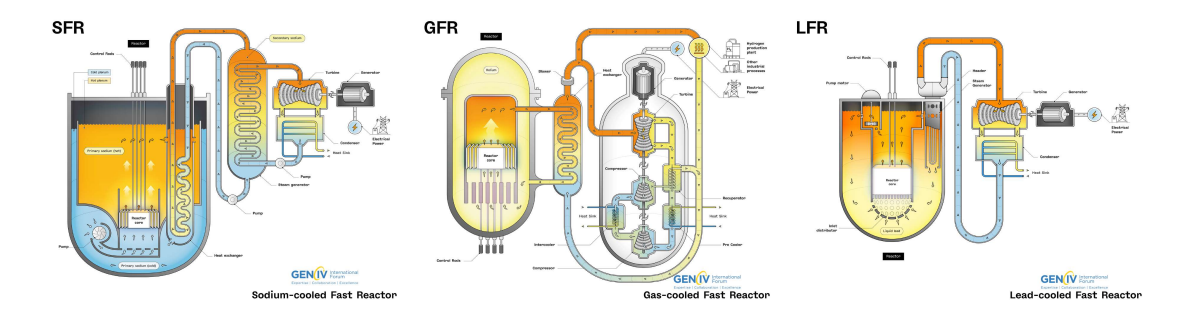
• Supercritical-Water cooled Reactor.

The SCWR is a light-water reactor (LWR) operating above the critical point of water (374°C, 22.1 MPa), allowing for higher thermal efficiencies in the range of 44–48%. Both thermal and fast neutron spectrum options are being developed, as well as open and closed fuel cycles. The outlet temperature is typically above 500°C, and various reactor sizes are under study.

• Very-high-temperature reactor.

VHTR is a graphite-moderated, helium-cooled reactor operating with a thermal neutron spectrum. It targets very high outlet temperatures, up to 1000° C, with an estimated thermal efficiency of around 50%. This makes it ideal for hydrogen production and industrial process heat. The reference thermal power is $600~MW_{\rm th}$, selected to ensure passive safety in decay heat removal. The reactor uses TRISO fuel, enabling robust fuel containment. It can support closed uranium/plutonium fuel cycles and contribute to waste minimization.

In figure 2.1 the main characteristics of the six generation IV reactors:



(a) SFR (b) GFR (c) LFR

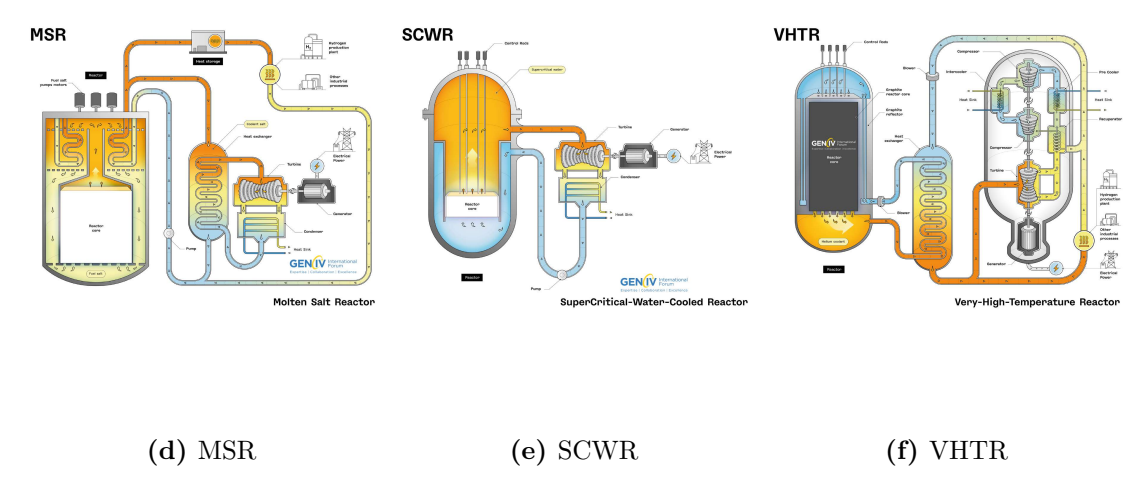


Figure 2.1: Schematic diagrams of the six Generation IV reactor concepts[3].

To be complete, in parallel with the development of Generation IV reactor technologies, there is growing interest in Small Modular Reactors (SMRs). Defined as advanced nuclear reactors with an electrical output of up to $300~MW_e$, SMRs represent an innovative design approach that emphasizes modularity, scalability, and flexibility. Their key advantages include shorter construction times, lower capital investment, enhanced inherent and passive safety features, and suitability for remote or off-grid applications. Additionally, the smaller reactor core results in lower decay heat, further contributing to simplified safety systems. SMRs exemplify how advanced design principles are already being applied in modern reactor development.

2.2 Historical SFR Design Concepts

Since the 1950s, fast reactor technology has been actively pursued and demonstrated around the world through various national advanced reactor development programs. This effort has led to the development, construction, and operation of numerous experimental and prototype SFRs.

A major milestone in the history of nuclear power came on December 20, 1951, when the Experimental Breeder Reactor I (EBR-I), located near Arco, Idaho, at the National Reactor Testing Station, became the first power plant in the world to produce electricity using atomic energy¹. Initially, it generated a very small amount of power—enough to light four 200-watt bulbs, a symbolic achievement

that marked the dawn of civilian nuclear power. The next day was generated enough energy to power the entire facility.

EBR-I was not only a groundbreaking demonstration of nuclear electricity generation but also a key contributor to fast reactor research. In 1953, it was confirmed through measurements that the reactor had successfully demonstrated the basic principle of breeding, making it the world's first breeder reactor. Later, on November 27 1962, it has been further proven its versatility by producing electricity using a plutonium core.

The reactor employed a liquid sodium-potassium (NaK) eutectic mixture as its coolant—an early example of the technologies that would become central to SFR design. It operated successfully for 12 years before being permanently shut down in December 1963[4].

These early developments laid the foundation for subsequent conceptual designs of SFRs worldwide, which continue to evolve based on the lessons learned from pioneering projects like EBR-I.

2.2.1 EBR-II

The Experimental Breeder Reactor-II (EBR-II), designed and operated by Argonne National Laboratory (ANL) in Idaho for the U.S. Department of Energy, operated from 1964 until its shutdown in 1994. It was primarily an engineering test facility intended to evaluate the feasibility of using this type of reactor for central station power generation.

The EBR-II complex consisted of several buildings, each housing key components of the plant and supporting various feasibility demonstrations. These included research on metal and oxide fuels, investigations into the passive safety features of liquid metal fast reactors (LMFRs), and other important aspects of advanced reactor technology.

Plant overview

Considered a precursor to today's Sodium-cooled Fast Reactors (SFRs), the EBR-II was a sodium-cooled fast breeder reactor developed to produce a thermal output of 62.5 MW, corresponding to an electrical output of approximately 20 MW. Figures 2.2 and 2.3 illustrate the reactor design and the corresponding flow path. It was designed as a pool-type sodium reactor, housing all primary system components within a double-walled vessel measuring nearly 8 meters in both diameter and

¹In 1954, the sovietic reactor APS-1 Obninsk will be the first nuclear power plant connected to an electricity grid providing power to residences and businesses.

height, and containing approximately 341 m³ of liquid sodium. The reactor's power conversion system comprised three cooling loops:

- Primary Sodium Loop: This loop was responsible for removing the heat generated in the reactor core. It operated with a mass flow rate of 485kg/s (approximately 0.571m³/s)[5]. Sodium entered the core at 371°C and exited at 482°C. As observed during the Heat Removal Tests SHRT-17 and SHRT-45R², the operating pressure at the discharge of primary sodium pumps 1 and 2 was approximately 2.9bar, while the pressure at the core outlet (upper plenum) was around 0.44bar[6].
- Intermediate Sodium Loop: Operating at 315 kg/s (approximately 0.371 m³/s), this loop transferred heat from the primary loop while providing isolation from the radioactive core. Sodium entered the intermediate heat exchanger at around 310°C and exited at about 460°C
- Tertiary Loop (Steam/Power Generation Loop): This loop utilized a sodium-to-water heat exchanger to produce steam for electricity generation. Operating at a steam flow rate of 32 kg/s (approximately 2.91 m³/s), the system powered a conventional superheated condensing turbine-generator setup. The feedwater entered the heat exchanger at 288°C and was converted to steam at 304°C.

²On June 20, 1984, the SHRT-17 full-power loss-of-flow test demonstrated the effectiveness of natural circulation in the EBR-II reactor. On April 3, 1986, the SHRT-45 test confirmed the role of passive reactivity feedback in bringing the reactor to decay heat power. These tests were fundamental in establishing sodium-cooled reactors as a viable foundation for future inherently safe reactor designs.

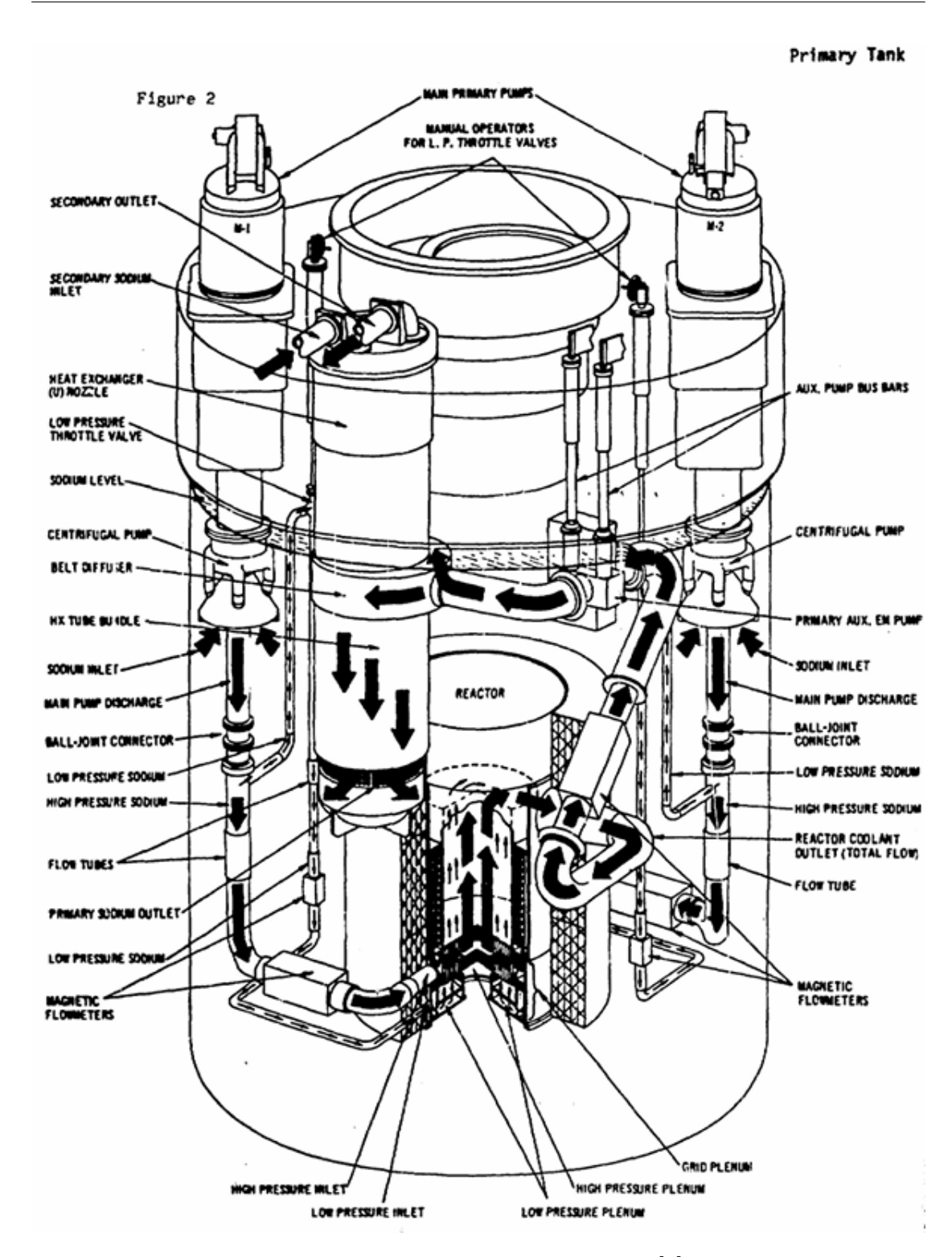


Figure 2.2: EBR-II reactor design[7].

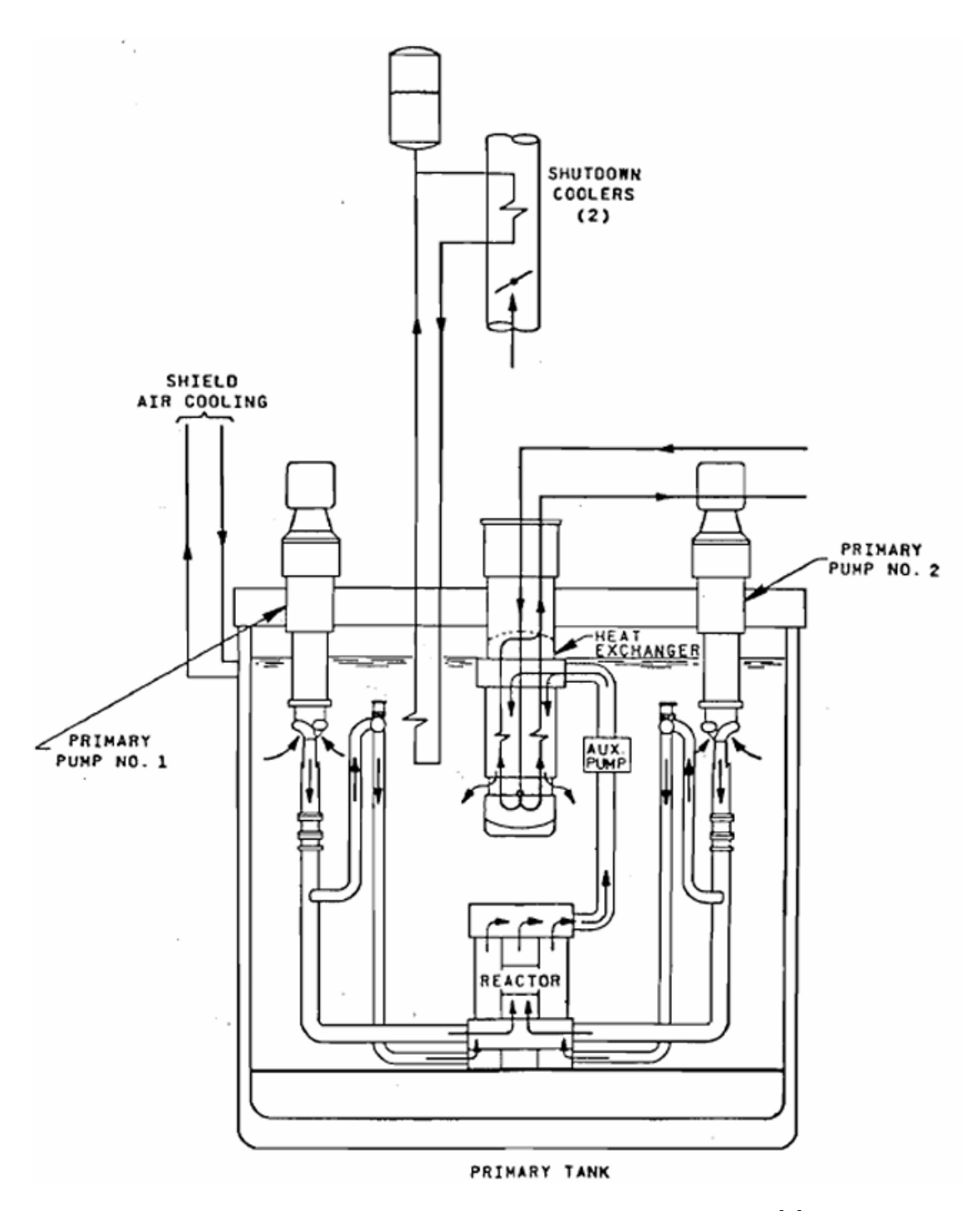


Figure 2.3: EBR-II primary tank flow path sketch[6].

Core layout

The reactor-vessel grid-plenum assembly of EBR-II accommodated a total of 637 hexagonal subassemblies, which were organized into three primary regions: the core, the inner blanket, and the outer blanket. The subassembly arrangement and the identification convention are illustrated in Figure 2.4.

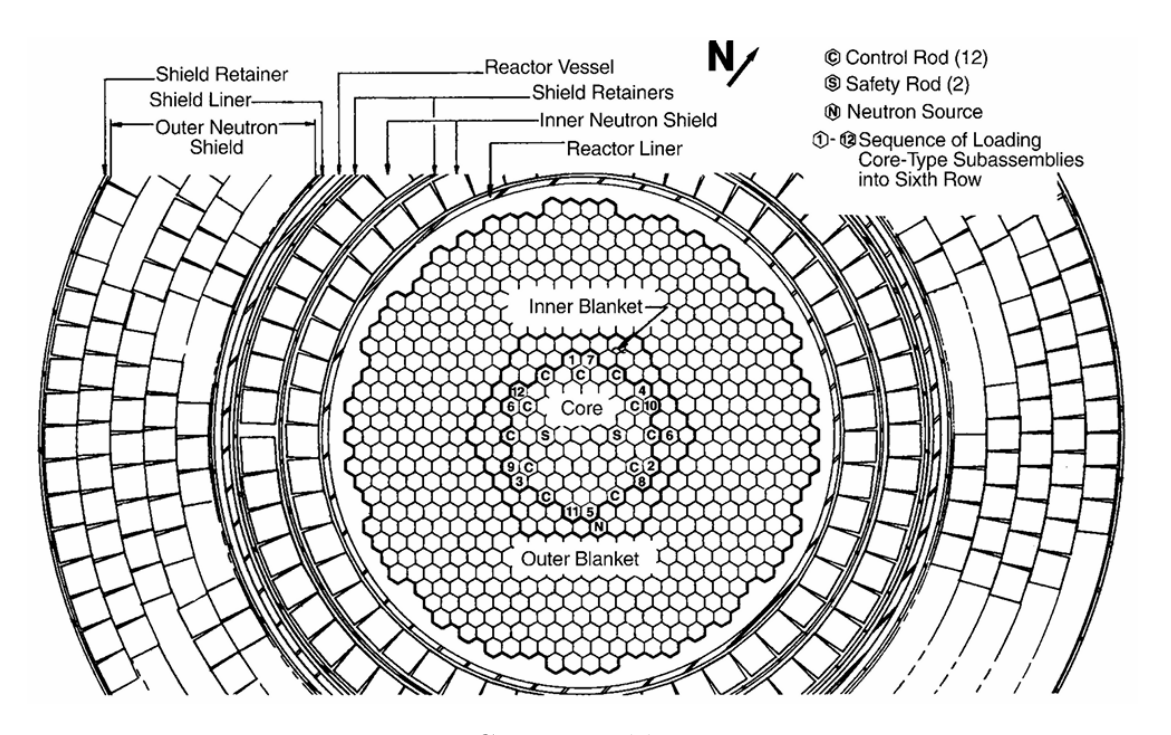


Figure 2.4: Core assemblies arrangement.

The central core region consisted of 61 subassemblies, distributed across the first five hexagonal rings. This region primarily housed driver fuel and experimental irradiation subassemblies. Specific positions within the core were designated for control and instrumentation:

- Two positions in ring 3 were occupied by safety-rod subassemblies.
- Twelve positions in ring 5 were normally allocated to control-rod subassemblies. During the SHRT-17 and SHRT-45R tests, two of these ring 5 positions were instead used for instrumented subassemblies test (INSAT), identified as XX09 and XX10. Two other positions in ring 5, also typically used for control rods, were assigned to the in-core instrument test (INCOT), designated as XY16, during the same tests.

The inner blanket region, comprising rings 6 and 7, was originally designed

to accommodate 66 blanket subassemblies. However, during the SHRT-17 and SHRT-45R heat removal tests, this configuration was altered:

- ring 6 was loaded with driver fuel and irradiation subassemblies, forming part of the expanded core configuration.
- ring 7 was filled with reflector subassemblies.

The outer blanket region included rings 8 through 16, accommodating a total of 510 subassemblies. These were configured as either blanket subassemblies or reflector subassemblies, depending on operational requirements.

Subassembly geometry

The subassemblies shared a broadly consistent external architecture, though internal configuration varied with function. Structurally, each unit was composed of three principal segments:

- 1. The upper adapter: At the upper end, a specially designed adapter allowed the subassembly to align properly within the reactor's core layout. This component, in 304SS excelent as neutron shield, was tailored to match the hexagonal cross-section of the enclosing tube and its orientation.
- 2. The center region: The central body of the subassembly was encased in a hexagonal sheath, serving both as a mechanical enclosure and a coolant flow channel. In a fuel subassembly, the region includes the upper and lower reflectors, between which the active fuel section is located.
- 3. The lower adapter: At the lower end, a bottom adapter in 304SS anchored the subassembly into position within the core support structure composed. Beyond mechanical placement, this component also regulated the inlet flow of coolant, influencing the thermal-hydraulic behavior of the assembly.

The configuration of the MARK-II fuel assembly is shown below, illustrating its main axial components, while Figure 2.6 presents the detailed geometric features.

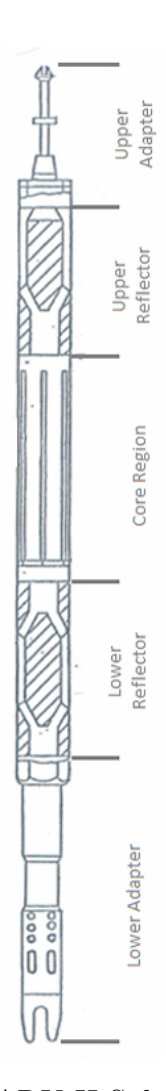


Figure 2.5: Sample MARK-II Subassembly Configuration.

Internally, each subassembly housed a specific arrangement of fuel or blanket elements—tailored in geometry and composition according to its designated role in the reactor. The internal configuration of the central section varied between subassembly types, reflecting differences in fuel composition, neutron economy, and thermal output.

For each kind, the pitch of the subassembly structure is 58.928 mm. The flat-to-flat external and internal dimensions are 58.166 mm and 56.134 mm, respectively. Fuel and blanket subassemblies use 316SS for their hexagonal ducts, while other types, such as safety and control subassemblies, employ 304SS. With a total assembly height of 2.3328 m[8], Table 2.1 summarizes the main characteristics of the subassemblies involved in the SHRT-45R test. For those subassemblies containing fuel element bundles, the elements are equipped with helical wire wraps

to maintain spacing and promote coolant flow.

Table 2.1: Design Parameters of EBR-II Subassembly Elements at 20 $^{\circ}\mathrm{C}$.

Item	Mark-	Mark-IIS	XX09	XX10	Outer
	II(A)	(C)			Blanket
Fuel alloy, wt. %	U-5Fs	U-5Fs	U-5Fs	Stainless	Depleted
				Steel	Uranium
Enrichment weight, %	67	67	67	N/A	~ 0.0
$^{235}\mathrm{U}$					
Number of Elements	91 (91)	61	59 of 61	18 of 19	19
Fuel-slug length, m	0.3429	0.3429	0.3429	N/A	1.3970
Fuel-slug diameter, mm	3.3655	3.3655	3.3655	N/A	11.0998
Cladding-wall thickness,	0.305	0.305	0.305	Solid rod	0.4570
mm					
Cladding-wall OD, mm	4.4196	4.4196	4.4196	8.81	12.5222
Element length, m	0.6108	0.5334	0.6108	0.6108	1.575
	(0.6362)	(0.6108)	(0.6494)	(0.6951)	
Restrainer height above	12.7	12.7	None	_	N/A
fuel, mm					
Sodium level above fuel,	31.75	6.35	6.35	6.35	30.48
mm	(6.35)				
Plenum gas	Inert gas	Inert gas	Inert gas	Inert gas	N/A
Cladding material	316SS	316SS	316SS	316SS	304SS
Space-wire diameter, mm	1.24	1.24	1.24	1.24	N/A
Space-wire material	316SS	316SS	316SS	316SS	N/A

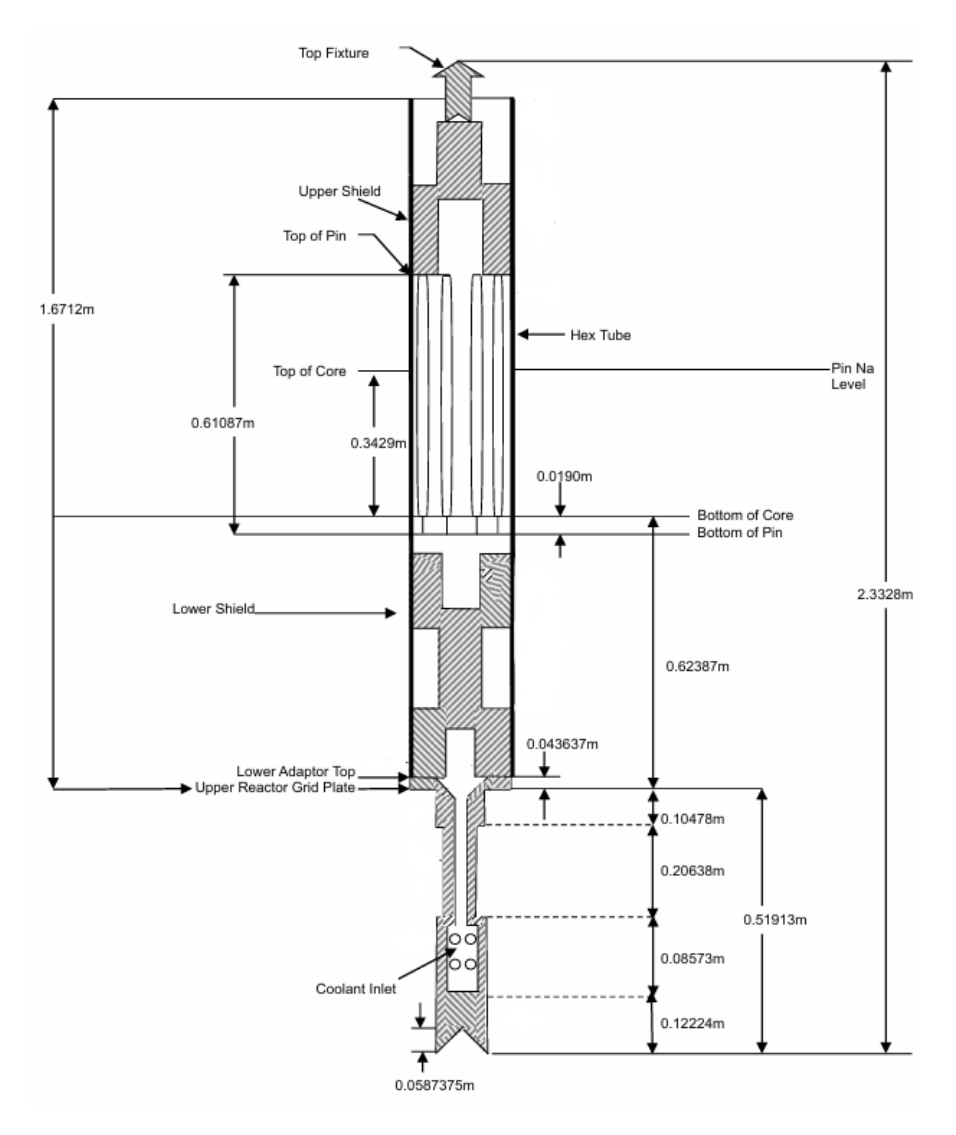


Figure 2.6: Mark-II assembly elevation section.

2.2.2 The French Trilogy: RAPSODIE, PHÉNIX and SU-PERPHÉNIX

In Europe, the development of SFRs was primarily led by France, which made a significant contribution to advancing this reactor technology. The French program is often referred to as the "French Trilogy", consisting of three major reactors: RAPSODIE, PHÉNIX, and SUPERPHÉNIX.

RAPSODIE

The first of these, RAPSODIE, was a loop-type fast reactor. Its development began in the late 1950s, and it achieved first criticality in early 1967. Initially designed as a 20MWt research reactor, its thermal power was later increased to 40MWt by 1970.

RAPSODIE featured two independent primary sodium coolant circuits, each transferring heat to a secondary sodium circuit, which then dissipated it through a sodium—air heat exchanger. The reactor was not designed for electricity generation and served purely as a research facility. The primary sodium entered the core at approximately 410°C and exited at over 500°C, depending on operational conditions.

The success of RAPSODIE provided valuable operational experience in materials behavior, system availability, fuel performance, and inherent safety. These early achievements laid the foundation for the development of more advanced reactors, leading directly to the design and construction of the PHÉNIX reactor. RAPSODIE was permanently shut down in 1983 following a series of promising end-of-life tests.

PHÉNIX

The early operational years of RAPSODIE coincided with the design studies of the PHÉNIX reactor, which achieved first criticality in 1973. The vessel design is shown in Figure 2.7 This same year also marked the beginning of conceptual work for the future SUPERPHÉNIX reactor. PHÉNIX was a pool-type fast reactor with a thermal output of approximately 565MWt and an electrical output of 255MWe.

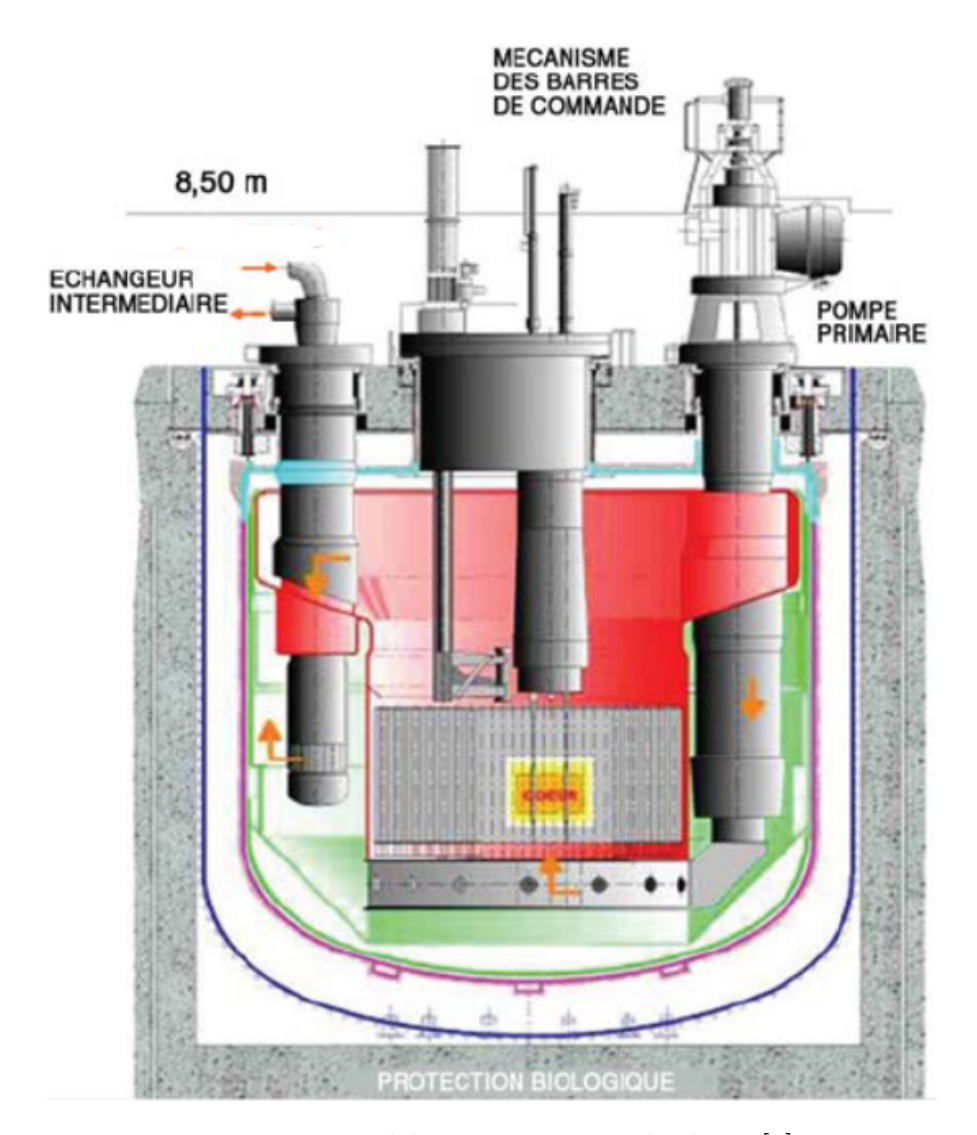


Figure 2.7: Phénix reactor vessel scheme[9].

The reactor core received primary sodium at about 400°C, which exited at 560°C. Each of the three primary sodium loops supplied coolant to the core at a flow rate of 950kg/s. The secondary sodium system operated at 700kg/s, with temperatures ranging from 350°C at the inlet of the intermediate heat exchangers to 550°C at the outlet. In the steam generation system, water entered at 246°C and exited at 376°C, with a flow rate of 210kg/s per loop. Unlike RAPSODIE, PHÉNIX incorporated reheating-type steam generators capable of driving turbine-generator systems for electricity production.

The reactor vessel measured approximately 12m in height, with a similar diameter. The core, whose configuration is shown in Figure 2.8, consisted of 103 fuel

subassemblies, each measuring approximately 4.3m in total height and containing 271 MOX fuel pins (mixed uranium-plutonium oxide). Each pin had a fuel column length of 1.793m and a fuel pellet diameter of 5.5mm, with stainless steel cladding bringing the outer diameter to 6.5mm. The assemblies included upper and lower fertile blankets and neutron shielding sections. Radially, the core was surrounded by 90 blanket subassemblies containing 61 depleted uranium oxide pins, each with a diameter of 12.15mm, and an outer neutron shielding zone designed to limit activation of the secondary sodium loops.

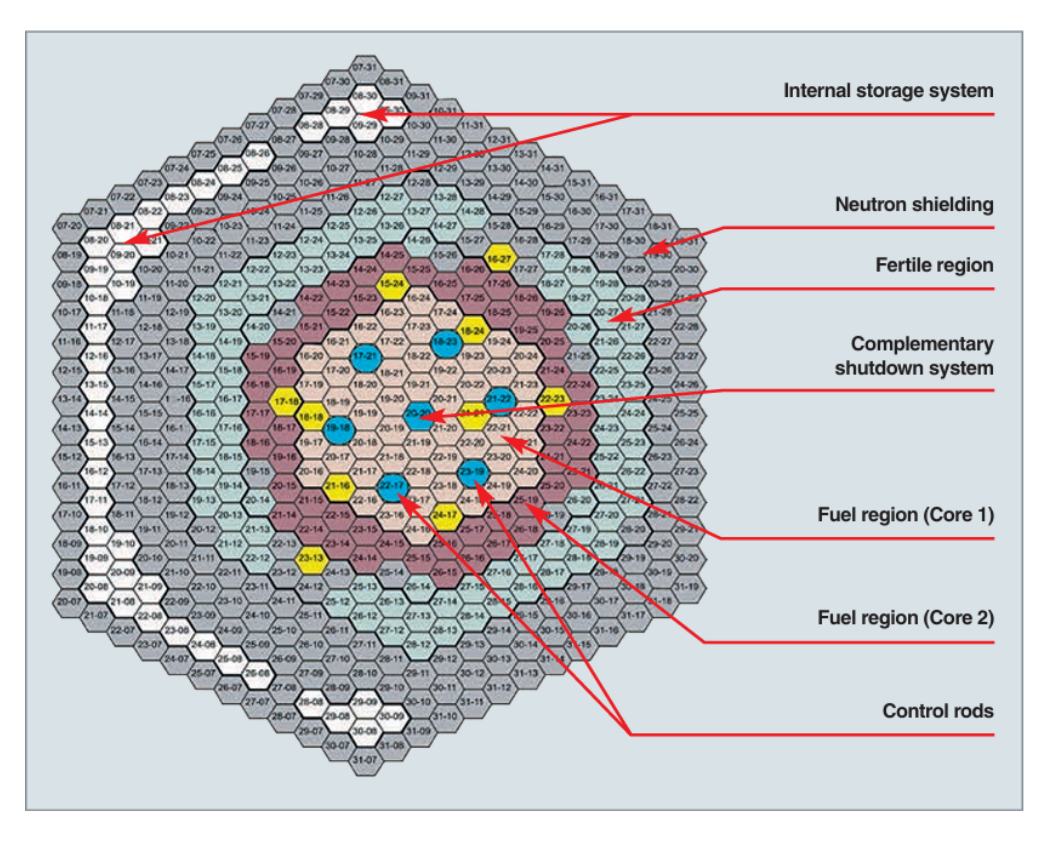


Figure 2.8: General layout of the PHÉNIX reactor core[10].

PHÉNIX was designed with the goal of improving material performance, increasing the reliability of key components (such as intermediate heat exchangers, sodium pumps, and steam generators), and demonstrating the feasibility of a closed fuel cycle through fuel reprocessing. From 1992 onward, PHÉNIX operated primarily as an irradiation facility, with power limited to 350MWt (145MWe) using only two secondary loops. Following the cancellation of the SUPERPHÉNIX project, PHÉNIX underwent a thorough safety reassessment between 1994 and 2002. The reactor operated during its final cycle from 2003 until its permanent shutdown in 2009.

SUPERPHÉNIX

SUPERPHÉNIX emerged as a flagship European fast reactor project, primarily led by France, with financial and technical collaboration from Italy and Germany. The reactor achieved first criticality in 1985. Building on the technological advancements and experience of its predecessors, SUPERPHÉNIX represented a significant scale-up and was envisioned as a prototype for future commercial deployment.

Designed with a thermal output of 3000MWt and an electrical output of 1200MWe, SUPERPHÉNIX was far larger than Phénix. Its reactor vessel had an internal diameter of 21m and a height of 19.5m. The primary system consisted of four cooling loops, each with a flow rate of 4.24t/s and sodium temperatures of 545°C in the hot leg and 395°C in the cold leg. The sodium inventory in the primary circuit was approximately 3500 tons. The secondary system also had four loops, with a combined inventory of 1500 tons and a flow rate of 3.27t/s per loop, operating between 525°C (hot leg) and 345°C (cold leg).

The steam cycle featured a flow rate of 340kg/s per loop, producing steam at 487°C and a pressure of 177bar at the turbine inlet, and exiting at 237°C after expansion. The reactor was equipped with reheating-type steam generators for efficient power conversion.

Despite its technological promise, SUPERPHÉNIX faced numerous operational challenges and was subject to significant political, economic, and media pressure throughout its lifespan. These non-technical factors led to repeated operational suspensions and, ultimately, a premature shutdown in 1997, well before the reactor could fully realize its intended objectives.

2.2.3 Worldwide SFRs experience

Research on Sodium-Cooled Fast Reactors (SFRs) has attracted significant global interest. One of the most extensive programs has been developed by Russia (USSR), beginning in 1958 with the experimental BR-5 reactor, which had a thermal capacity of 5 MWt (5000 kW). This was followed by the BR-10 and BOR-60 research reactors—the latter with a thermal capacity of 60 MWt and an electrical output of approximately 12 MWe. These three early experimental reactors laid the technological foundation for the future BN (Bystrie neytrony—"Fast Neutron") series of fast reactors.

A major milestone in the Russian fast reactor program is the BN series, all located at the Beloyarsk Nuclear Power Plant. This includes the BN-350, BN-600, and BN-800 reactors.

The BN-350, a loop-type reactor, achieved first criticality in 1972 and operated until its shutdown in 1999. It was equipped with six primary loops (inlet/outlet temperatures of $288^{\circ}\text{C}/437^{\circ}\text{C}$) and six intermediate loops with associated steam

generators. The BN-350 was particularly notable as the world's first commercial liquid-metal-cooled fast breeder reactor designed to co-generate electricity and desalinated water. It was originally designed for a thermal power of 1000 MWt, though the average thermal power during operation did not exceed 600 MWt, with a maximum of approximately 750 MWt. Consequently, the electrical output was typically between 125 and 150 MWe.

The BN-600, a pool-type reactor, began operation in 1980 and remains in service. It is designed for 1470 MWt thermal power and produces approximately 600 MWe. Sodium enters the core at around 380°C and exits at 550°C. The reactor vessel is a simple cylindrical shape, approximately 12.8 meters in diameter and 12.6 meters high. The BN-600 follows a three-loop configuration, with each primary loop handling about 2,3 kg/s of sodium flow. The reactor core is composed of around 400 hexagonal fuel assemblies, each with a flat-to-flat dimension of 96 mm and a spacing of 98 mm. Each assembly contains 127 fuel pins with an external diameter of 6.9 mm. Additionally, 27 core positions are occupied by control and safety rods. The core design has undergone three major upgrades for improved safety and operability. Fuel assemblies incorporate upper and lower axial blanket regions for breeding and shielding, while the core is radially surrounded by lateral blanket and reflector assemblies.

The most recent in the series, the BN-800, is also a pool-type reactor. It began operation in 2014 after several delays, with grid connection occurring in 2016. Designed for 2100 MWt of thermal power and producing 800 MWe, the BN-800 is the first Russian reactor of this type to actively incorporate a closed fuel cycle. It includes 560 core assemblies and 30 control rods, with an active core height of 90 cm. The BN-800 continues the key design principles of its predecessors while implementing improvements in fuel recycling and operational efficiency[11].

Beyond Russia, several other countries have pursued SFR development, each with distinct national objectives and technological strategies.

In Japan, the SFR program began with the construction of the experimental JOYO reactor, which achieved first criticality in 1977. JOYO is a loop-type reactor that originally operated at 50 MWt, and through a series of upgrades reached 140 MWt by 2003. As of 2021, it continues operation at 100 MWt. The reactor is configured with two primary cooling loops and one auxiliary system. In its latest operating mode, sodium enters the core at approximately 350°C and exits at 456°C, with a flow rate of 375kg/s per loop. The reactor core features a height of 50 cm, with a maximum of 79 fuel driver subassemblies in the core configuration [12]. JOYO was primarily developed for materials testing and irradiation studies and remains in service today. Building on this foundation, Japan developed MONJU, a prototype sodium-cooled fast breeder reactor with a design thermal power of 714 MWt and an electrical output of 280 MWe. MONJU achieved first criticality in 1994, but its operational history was short-lived due to a significant sodium leak

incident in 1995, followed by extended legal, safety, and technical setbacks. The reactor was officially decommissioned in 2016, though it represented a critical step in Japan's long-term pursuit of a closed nuclear fuel cycle.

India has also made substantial investments in fast reactor technology, as part of its "three-stage nuclear power program". This began with the Fast Breeder Test Reactor (FBTR), a 40 MWt / 13.2 MWe sodium-cooled loop-type fast reactor, fueled with a unique plutonium-rich mixed carbide fuel. Although the reactor has rarely operated at its full design capacity, it has played a key role in India's fast reactor R&D. The FBTR includes two primary and two secondary sodium loops, along with a shared steam-water circuit. It reached first criticality in 1985, and in its latest configuration, features a compact core with 68 subassemblies and a fuel height of 32 cm[13].

China has more recently emerged as a major player in fast reactor development. The China Experimental Fast Reactor (CEFR) is a pool-type SFR with a thermal power of 65 MWt and electrical output of 20 MWe. It achieved first criticality in 2010, and was connected to the grid in 2011, marking China's entry into operational fast reactor technology. The CEFR core contains 81 hexagonal fuel assemblies in its equilibrium configuration, each composed of 61 fuel pins with a diameter of 6 mm. Stainless steel is used for fuel cladding. The primary cooling system consists of two sodium loops integrated within the reactor vessel[14].

Together, these international efforts reflect the enduring global commitment to sodium-cooled fast reactors as a pathway toward sustainable nuclear energy. These reactors are especially relevant in addressing key goals such as plutonium management, closed fuel cycles, and the development of breeder reactor technologies for long-term energy security.

2.3 Current State and Future Prospects

Following decades of research and operational experience, SFRs have entered a new phase of development aimed at fulfilling the objectives of Generation IV nuclear systems.

Building on the technical foundations laid by earlier experimental and demonstration reactors, current efforts focus on scalable, commercially suitable reactor designs that incorporate passive safety features, advanced fuel cycles, and modular construction strategies.

2.3.1 The ABR-1000: design, objective and roadmap

In the United States, ANL has remained a key institution in advancing SFR concepts, despite the cancellation in 1994 of the Integral Fast Reactor (IFR) program, which aimed to develop a commercial prototype of a sodium-cooled reactor following the

excellent results achieved with EBR-II. The conceptual successor to the IFR is the Advanced Burner Reactor (ABR)—specifically the ABR-1000, a 1000 MWt sodium-cooled fast reactor core concept developed by ANL. Designed as a reference model for national R&D efforts, the ABR-1000 was created to support studies on actinide transmutation and advanced fuel cycles within the U.S. Department of Energy (DOE). It serves today as a technical benchmark for evaluating future SFR design options.

From the same IFR legacy are inspire two main SFR design which are PRISM, developed by GE Hitachi, and Natrium, developed by TerraPower in partnership with GE Hitachi.

PRISM (Power Reactor Innovative Small Module) is a pool-type, metal-fueled SFR with passive safety features and modular scalability. Originating from the U.S. Advanced Liquid Metal Reactor program of the 1980s–1990s, PRISM was conceived for both power generation and plutonium disposition. The design features a 840 MWt core producing approximately 311 MWe, using liquid sodium as coolant and a metal fuel alloy (U-Pu-Zr). Although the concept was revitalized in 2006, it has not advanced to commercialization, and active development has slowed. Nevertheless, PRISM remains a technically mature design with continued relevance, particularly for waste management and modular reactor deployment [16].

Natrium, by contrast, represents a more recent and commercially oriented evolution of SFR technology. While it draws on the same design heritage, it introduces innovations aimed at flexibility and grid integration. The reactor delivers 840 MWt of thermal power and 345 MWe through a separate power conversion system. Notably, it includes a molten salt thermal storage system that enables power peaking up to 500 MWe, supporting load-following operation. Natrium uses high-assay low-enriched uranium (HALEU) fuel and is currently being developed with great support. The first demonstration plant is under construction in Kemmerer, Wyoming, with commissioning targeted for the early 2030s[17].

In this broader context, the ABR-1000 serves as a central reference design for academic and industrial R&D on SFRs. Its design captures many of the key characteristics desired for future advanced reactors making it an ideal baseline for further analysis, development, and optimization. In the following section, the ABR-1000 reference concept will be presented in detail, forming the basis for the benchmarking and thermo-hydraulic studies carried out in this thesis.

³The IFR concept was developed by ANL starting in 1984, with a focus on improving safety and addressing proliferation concerns. It aimed to commercialize a pool-type, metal-fueled SFR with passive safety systems and an integrated fuel cycle based on pyroprocessing. From the mid-1980s, EBR-II was used as a demonstrator for the IFR program, validating key features such as passive shutdown capability and the use of metal fuel. Despite its technical success, the program was cancelled in 1994 due to changes in U.S. nuclear policy and funding priorities.[15]

Originally conceived within the framework of the Global Nuclear Energy Partnership (GNEP) in 2006, the ABR-1000 was developed to support advanced fuel cycle strategies aimed at transmuting recycled transuranics. The objective was to produce energy while simultaneously reducing the long-term radiotoxicity and decay heat of nuclear waste destined for geological repositories.

Plant Design

The reference concept, shown in Figure 2.9, available by the end of 2007, integrates key features from past fast reactor programs and adopts design parameters representative of a commercial-scale reactor, while maintaining flexibility.

The ABR-1000 is configured as a pool type SFR, in which the entire primary system(Figure 2.10) including the reactor core, four primary pumps, intermediate heat exchangers (IHXs), and the Direct Reactor Auxiliary Cooling System (DRACS) is immersed within a single reactor vessel constructed of Type 304 austenitic stainless steel. The overall height of the reactor vessel is 14.77 m. This layout minimizes the risk of coolant loss and leverages the large thermal inertia of the sodium pool to enhance system stability during transients. All penetrations are located on the top head of the vessel (referred as deck), further simplifying design and improving safety.

A structural separation between the hot and cold sodium, known as the redan, is employed to thermally isolate the outlet and inlet flows. As a result, the reactor vessel is exposed only to cold sodium, reducing thermal stresses and improving structural longevity. A guard vessel surrounds the main reactor vessel, serving as an additional passive safety feature in the unlikely event of a primary boundary breach.

In normal operation, four primary pumps draw cold sodium from the lower pool and deliver it to a core inlet plenum, which ensures uniform flow distribution through the fuel subassemblies. After passing through the core and being heated, the hot sodium exits through the outlet plenum, flows into the redan region, and then enters the intermediate heat exchangers. The pressure drop across individual fuel subassemblies depends on the fuel type. For metal fuel, the typical maximum pressure drop is approximately 3.1 bar, while for oxide fuel it increases to around 3.8 bar due to the greater pin bundle height. There, heat is transferred to a secondary sodium loop. This intermediate circuit subsequently transfers energy to a tertiary water/steam loop via four once-through helical coil steam generators, enabling the production of electricity.

The main design parameters of the ABR-1000 are summarized below in Table 2.2.

Table 2.2: ABR-1000 Main Design Parameters

Parameter	Value
Reactor Thermal Power	1000 MWt
Net Electric Output	380 MWe
Thermal Efficiency	38%
Coolant	Sodium
Flow rate	1256 kg/s
Coolant Inlet/Outlet Temperature	355°C / 510°C
Fuel Type	Metal and Oxide (startup and recycle)
Cladding / Duct Material	HT-9
Core Cycle Length	12 months
Design Plant Life	30 years (extendable to 60 years)
Reactor Vessel Dimensions	14.1 m diameter, 14.8 m height
Structural Materials	Austenitic Stainless Steel
Primary Pumps	4 Mechanical (Centrifugal) Pumps
Power Conversion System	Rankine Steam Cycle
Steam Generators	4 Once-through Helical Coil SGs

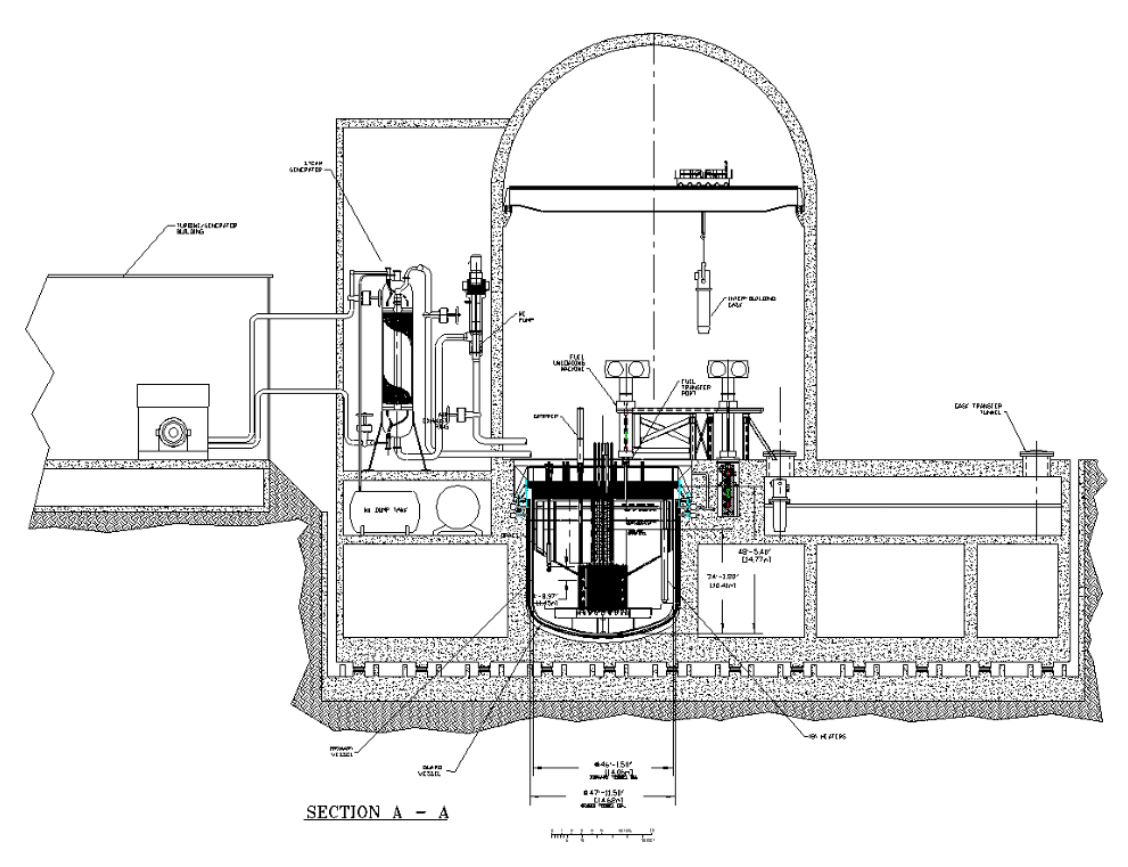


Figure 2.9: Plant overview of the ABR-1000 $\,$

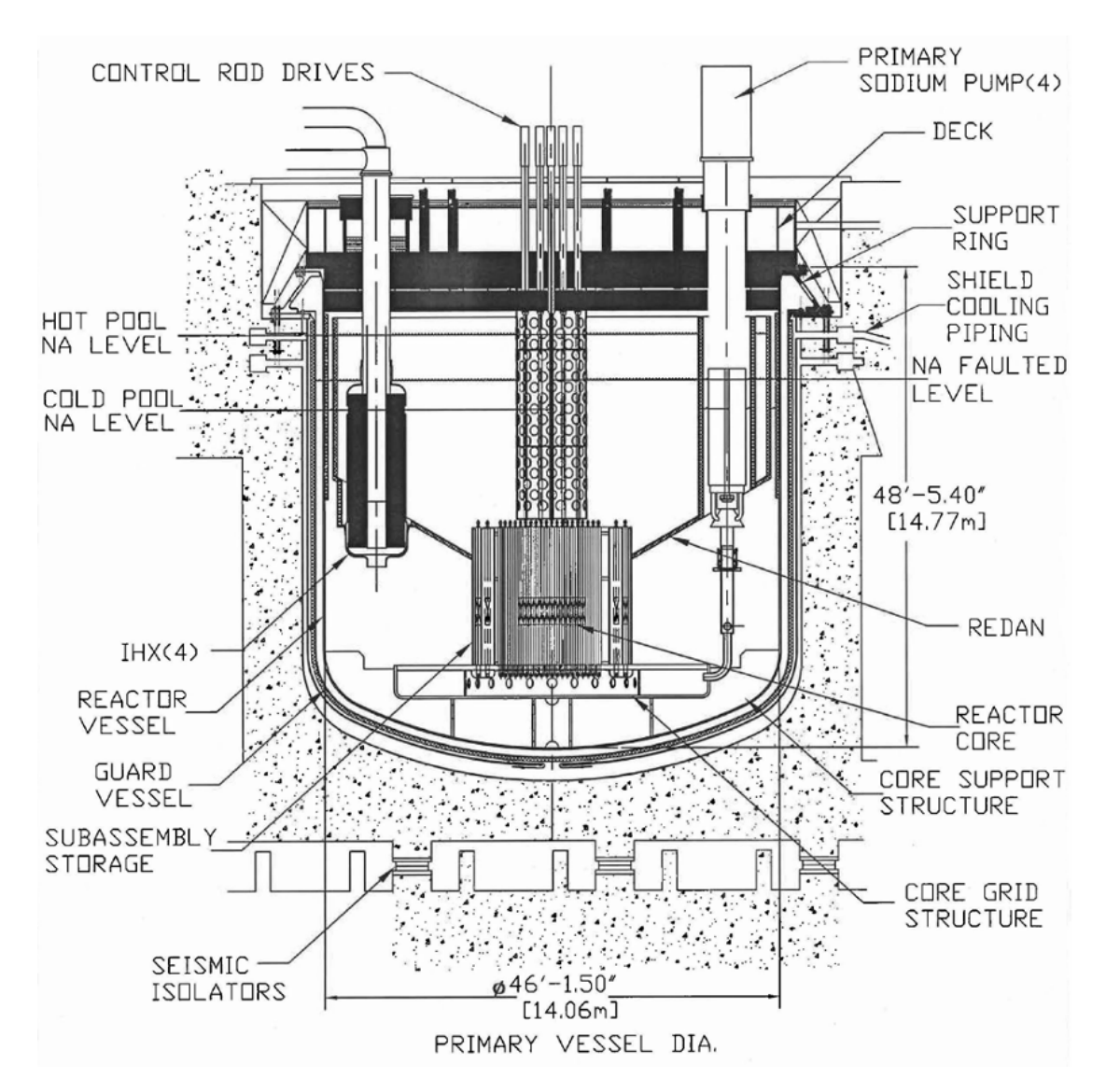


Figure 2.10: ABR-1000 primary system

Core features

The ABR-1000 core is composed of 180 fueled assemblies, divided into two enrichment zones:

- 78 assemblies in the inner core region (1 to 5 ring)
- 102 assemblies in the outer core region (6 to 8 ring)

Surrounding the core there are 114 radial reflector assemblies (in ring 9 and 10) and 66 radial shielding assemblies (in ring 12), which ensure adequate neutron

economy and structural protection. The reactor also includes 15 primary control rod assemblies (along ring 4 and 7) and 4 secondary control rod assemblies (in ring 1 and along ring 4), providing two independent, safety-grade reactivity control systems to ensure reliable shutdown under all conditions. The core was designed to accommodate two reference fuel types, with same radial layout and assembly geometry simplifying comparative analysis and design studies, which are metallic fuel composed of U-TRU-Zr (uranium-transuranic-zirconium alloy) and the classic oxide fuel form of UO₂-TRUO₂ (MOX). The structural material for cladding and ducting is HT9, a low-swelling ferritic-martensitic stainless steel, selected for its excellent high-temperature mechanical stability and irradiation resistance.

Figure 2.11 illustrates the radial configuration adopted for the ABR-1000 core.

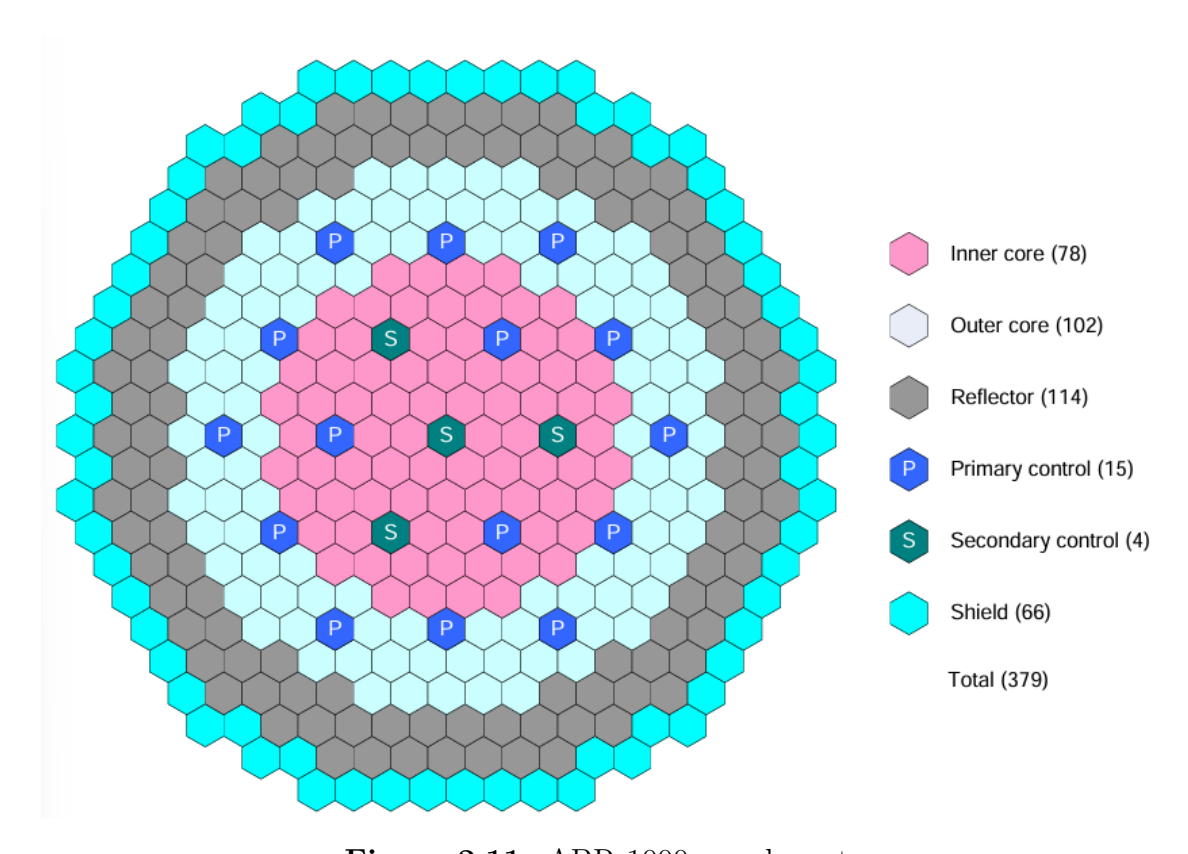


Figure 2.11: ABR-1000 core layout

Subassemblie configurations

All core subassemblies—including those for fuel, control rods, reflectors, and shielding—employ a common structural framework and maintain a uniform total length of 477.52 cm, measured from the base of the nosepiece to the top of the

handling socket. This standardized design approach simplifies fabrication and handling across the reactor core.

Although the external dimensions are consistent across all subassemblies, their internal configurations differ significantly depending on function. Variations include the number and type of pins, the fuel or absorber material, smeared density, and structural arrangements. A detailed comparison of the key design parameters for each subassembly type is presented in Table 2.3.

Table 2.3: Comparison of Subassembly Design Parameters for ABR-1000[18]

Parameter	Fuel (Oxide)	Fuel (Metal)	Reflector	Shield	Control	
Assembly Data						
Number of pins	271	271	91	19	7	
Assembly pitch (cm)	16.142	16.142	16.142	16.142	16.142	
Inter-assembly gap (cm)	0.432	0.432	0.432	0.432	0.432	
Duct flat-to-flat (cm)	15.710	15.710	15.710	15.710	15.710	
Duct thickness (cm)	0.394	0.394	0.394	0.394	0.394	
Interior duct gap (cm)	=	-	-	-	0.400	
Interior duct thickness (cm)	_	_	_	_	0.394	
Interior duct flat-to-flat (cm)	_	_	_	_	13.334	
Overall duct height (cm)	477.52	477.52	477.52	477.52	477.52	
Pin Data						
Pin material and type	MOX	U- TRU - Zr	HT9	$\mathrm{B_{4}C}$	B_4C	
Bond material	He	Na	_	$_{ m He}$	$_{ m He}$	
Pin length (cm)	381.0	332.7	381.0/332.7	381.0/332.7	112.3/86.3	
Active core height (cm)	106.7	81.3	=	81.0	_	
Pellet smeared density (% TD)	85.0	75.0	-	_	85.0	
Pellet diameter (cm)	0.627	0.557	1.541	2.553	4.193	
Cladding material	HT9	HT9	HT9	HT9	HT9	
Clad outer diameter (cm)	0.755	0.755	1.001	3.337	4.688	
Pitch-to-diameter ratio	1.180	1.180	1.001	1.001	1.029	
Cladding thickness (cm)	0.056	0.056	_	0.250	0.070	
Wire wrap diameter (cm)	0.131	0.131	_	_	0.133	
Volume Fraction at Fabrication	(%)				<u> </u>	
Fuel/Absorber	37.0	29.2	_	43.1	42.8	
Bond	2.0	9.8	-	10.1	7.6	
Structure	25.7	25.7	84.5	29.7	20.8	
Coolant	35.3	35.3	15.5	17.1	28.8	

Illustrative schematics of the metal and oxide fuel assembly layouts are provided in Figure 2.12, offering a visual comparison of their internal arrangements.

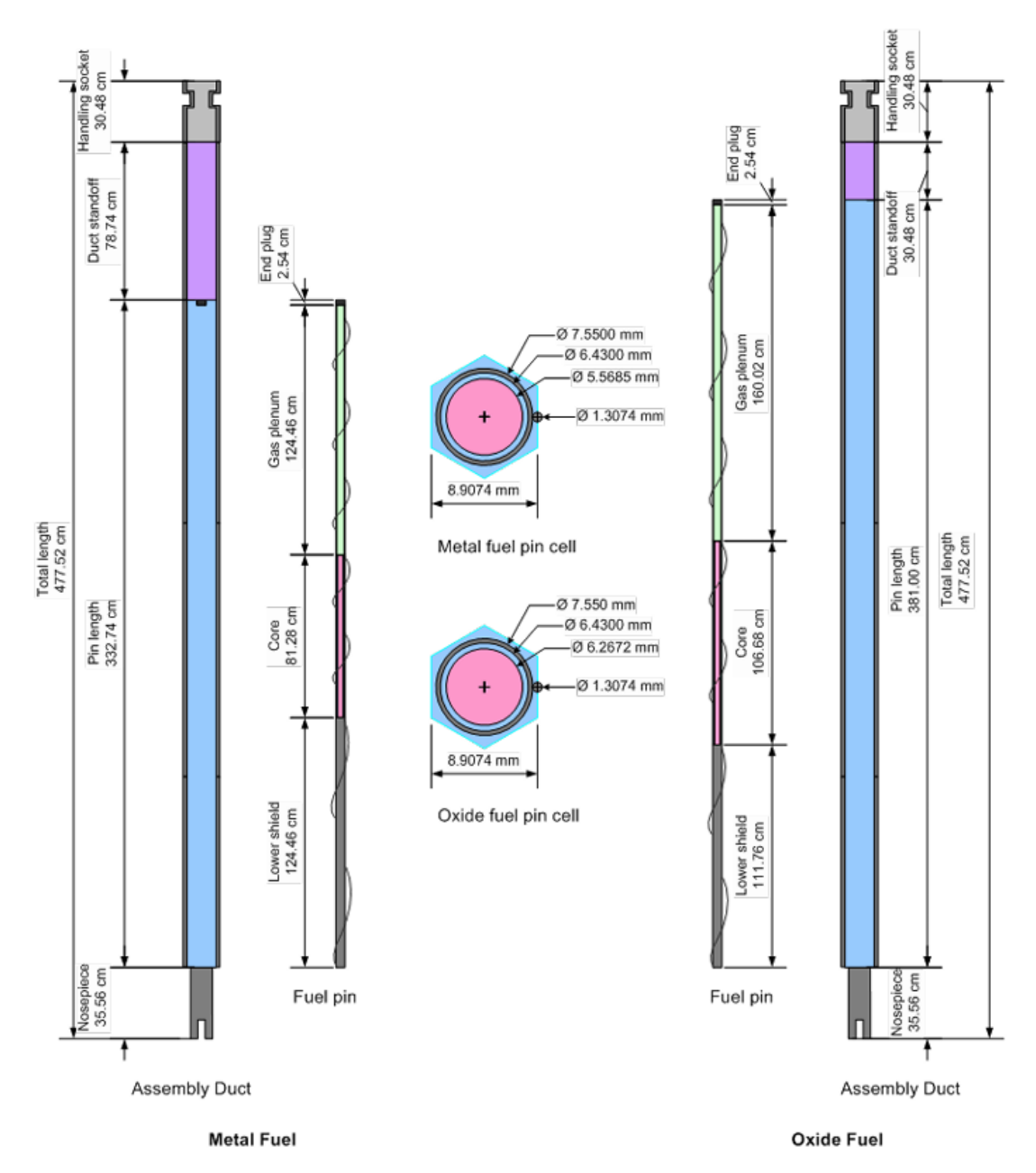


Figure 2.12: Internal layouts of ABR-1000 metal and oxide fuel assemblies

2.3.2 Status and outlook of SFR programs in Europe and Asia

France has a long history of development in SFRs, but currently, none are in operation. The most advanced recent initiative, the ASTRID project (Advanced

Sodium Technological Reactor for Industrial Demonstration), was launched in 2010 by the CEA (French Alternative Energies and Atomic Energy Commission) in collaboration with European and Japanese industrial partners. ASTRID was conceived as a pool-type fast reactor with a thermal power of 1500 MWt and an electric output of 600 MWe. It featured a MOX-fueled core with a specifically engineered low void reactivity effect, designed to enhance safety and allow for extended fuel cycles with stable reactivity control. Despite its promising design, ASTRID was canceled in 2019[19], primarily due to shifting national energy priorities, financial constraints, and a decreased urgency in the short to medium term of large-scale fast reactor deployment. Nevertheless, the expertise and technological advancements developed through ASTRID are now being carried forward by HEXANA, a CEA spin-off established in 2023. HEXANA is currently developing a Small Modular Fast Reactor (SMFR) cooled by sodium, with a projected thermal output of 400 MWt and an expected commercial deployment by around 2035. The reactor builds on the technological legacy of earlier French fast reactor programs and is designed to provide both electricity and high-temperature process heat for industrial applications, particularly in sectors such as chemical manufacturing, hydrogen production, and synthetic fuel generation.

The BN-1200 is a commercial fast reactor under development in Russia, intended for serial construction. Building on the operational experience and engineering success of the BN-600 and BN-800 reactors, the BN-1200 preserves their fundamental design principles while introducing technical and economic optimizations. It also incorporates enhanced safety provisions, aligning with the goals of Generation IV reactor systems. As such, it is considered one of the most promising candidates to enter the Generation IV category. The BN-1200 is a pool-type sodium-cooled fast reactor, designed with a thermal power output of 2800 MW(t) and a net electrical output of approximately 1220 MW(e). The reactor features four primary loops and an equal number of secondary loops. The primary circuit coolant temperature is specified at 550°C at the outlet of the core and 410°C at the inlet. Each primary loop is designed for a coolant flow rate of 3950 kg/s. Construction of the BN-1200 is expected to begin in the coming years(2026/2027), following the completion and regulatory approval of its detailed design documentation and licensing[20].

Despite the setbacks experienced in Japan's fast reactor program, after the failure of the MONJU reactor Japan remains actively engaged in the development of SFRs through long-term planning and international collaboration. The Japan Sodium-cooled Fast Reactor (JSFR) is a conceptual compact loop reactor design developed under the framework of Generation IV reactor goals. Although the JSFR project has not progressed to the construction phase, it remains a significant part of Japan's strategic vision for advanced nuclear energy. Two configurations have been proposed: a medium-scale reactor with an electrical output of 750 MW(e), and a large-scale reactor with an output of 1500 MW(e), corresponding to a thermal

output of 3530 MW(th).

The centerpiece of India's fast reactor program is the Prototype Fast Breeder Reactor (PFBR). This is a pool-type reactor with a two-loop configuration for both the primary and secondary systems, designed for a thermal power of 1250 MWt and a net electrical output of 500 MWe. Fueled with mixed uranium-plutonium oxide (MOX), the PFBR is intended to breed U-233 from thorium, in alignment with India's long-term nuclear strategy that emphasizes the use of its abundant thorium reserves. Although the PFBR has experienced several commissioning delays, it remains a cornerstone of India's future nuclear fleet and is currently expected to begin operation in 2026. Following the PFBR, two new reactors of similar power rating, FBR-1 and FBR-2, are planned to be built at the same site. Construction is anticipated to begin in the second half of this decade. These follow-up units will incorporate significant design improvements based on operational feedback and construction experience gained from the PFBR.

Based on the experience gained from the CEFR, China has advanced to the next stage of development with the CFR-600 (China Fast Reactor-600), a commercial-scale pool-type reactor. The first unit achieved first criticality in mid-2023 and is currently undergoing power ascension tests, with grid connection expected in 2025. A second unit is under construction, with commissioning anticipated around 2026. Each CFR-600 unit is rated at approximately 1500MWt and 600MWe, and designed to support China's long-term goals for a closed nuclear fuel cycle. The reactor features a two-loop design for both the primary and secondary sodium circuits, with an inlet temperature of about 380°C and an outlet temperature of approximately 550°C. The core is engineered to be flexible for both UO₂ and MOX fuel, with future upgrades potentially allowing the use of metallic fuel.

The following tables[21] summarize the past, currently operating and under development reactors cooled with sodium.

SFR: Concepts, Evolution and Prospects

Experimental breeder

Power Rating Project name Organization, Country Timeframe Notes 1.4 MWth EBR-1 Idaho National Laboratory, US 1950 - 1964First SFR, first breeder re-200 kWeactor 20 MWth Sodium Reactor Experiment Atomics International, US 1957-1964 $6.5 \, \mathrm{MWe}$ 1959–1964 (PuO₂) BR-5/BR-10 Soviet Union / Russia 5/10 MWth 1959-2002 1964–1972 (UC core) 1972-2002 (BR-10) DFRUnited Kingdom 60 MWth 1959-1977 Experimental reactor 430 MWth Fermi 1 DTE Energy, US Partial meltdown 1963-1975 150 MWe 62.5 MWth Pool-type, 67% w/o U-235 EBR-2 Argonne National Lab, US 1965-1994 20 MWeRapsodie France 40 MWth1967-1983 Loop-type, prototype 60 MWth 12 MWe (from 1973) 69-2017**BOR-60** RIAR, USSR/Russia Fuel/material testing for SFRs

20 MWth

1969 - 1972

Table 2.4: Historical Sodium-Cooled Fast Reactor Programs (Part 1)

SEFOR

USA

SFR: Concepts, Evolution and Prospects

 $\textbf{Table 2.5:} \ \ \text{Historical Sodium-Cooled Fast Reactor Programs (Part 2)}$

Project name	Organization, Country	Power Rating	Timeframe	Notes		
BN-350	Shevchenko/Aktau, USSR (Kazakhstan)	592 MWth 150 MWe	1972– 1994/1999	Used for desalination $(120,000 \text{ m}^3/\text{day})$		
KNK-II	Germany	58 MWth 17 MWe	1974–1991	Fuel testing facility		
PFR	United Kingdom	N/A	1974–1994	MOX fueled		
Phénix	CEA, EDF, France	22 MWth 9 MWe (start)	1973–2010	264 MWth, Breeding ratio 1.16		
SNR-300	Germany	327 MWth	1985–1991	Never reached criticality		
FFTF	DOE, US	400 MWth	1978–1993	No power generation		
Superphénix	EDF, Enel, France	3000 MWth 1242 MWe	1986–1997	Largest SFR built		
Monju	Japan Atomic Energy Agency	714 MWth 280 MWe	1995 / 2010	Loop-type, 15-year suspension, restarted 2010		

SFR: Concepts, Evolution and Prospects

Table 2.6: SFR projects currently operating

Project name	Organization, Country	Power Rating	Deployment	Notes
Joyo	Japan Atomic Energy Agency, Japan	140–150 MWth	1971– Present	3 core changes: MK-1, MK-2, MK-3
BN-600	Soviet Union, Russia	560 MWe	1980– Present	
FBTR	IGCAR, BARC, India	40 MWth 13.2 MWe	1985– Present	Reached 40 MWth in 2022
CEFR	China Institute of Atomic Energy, China	65 MWth 20 MWe	2012– Present	Built by Russia
BN-800	Russia	2100 MWth 789 MWe	2015– Present	
CFR-600	China National Nuclear Corp., China	1500 MWth 600 MWe	2023– Present	Xiapu-1, Xiapu-2; FBR
PFBR	India	1253 MWth 500 MWe	2024– Present	U-Pu Fuel Cycle

SFR: Concepts, Evolution and Prospec

Project / Program	Country / Org.	Power Rating	Expected Deployment	Notes
BN-1200	Russia	2900 MWth 1220 MWe	Not yet con- structed	Based on BN-600 and BN-800
ASTRID	France	600 MWe	Cancelled (2019)	Gen IV SFR prototype. Cancelled after development phase (2012–2019)
Natrium	TerraPower, US	840 MWth 345 MWe	Licensing	SMR design
4S	Toshiba, Japan	30 MWth 135 MWth	Pre-Licensing	Two configurations; ultra- compact design
ARC-100	ARC Clean Tech, US/Canada	286 MWth	Pre-Licensing	Metallic U alloy fuel; 20-year refueling cycle
HEXANA	Hexana, France	2×400 MWth	TBD	Modular SFR design with molten salt storage; based on CEA expertise
Otrera 300	Otrera Nuclear Energy, France	300 MWth	TBD	Cogeneration and <150°C heat; also targets minor actinide burning

As SFRs continue to evolve, moving from experimental to commercial deployment, the complexity of their thermal-hydraulic behavior demands advanced modeling capabilities. Tools that can accurately capture coolant mixing, temperature distributions, and subchannel phenomena are essential for design optimization and safety assessment. In the following chapter, the focus shifts from the technological development of SFRs to the numerical tools implemented in the DASSH software to analyze their performance.

Chapter 3

Thermal-Hydraulic Modeling of DASSH

Developed at Argonne National Laboratory, the open-source Python implementation of DASSH is a subchannel thermal-hydraulics code designed to simulate steady-state temperature distribution and coolant flow in hexagonal reactor cores with ducted fuel assemblies.

Assuming steady-state, incompressible flow, DASSH is well-suited for rapid thermal analysis during the preliminary phases of reactor design, when geometry and operating parameters are still evolving. This makes it a valuable tool for identifying thermally critical regions early in the design process.

Given the inlet coolant temperature, the power distribution across the core, and either the coolant mass flow rate or outlet temperature rise, DASSH computes the temperature profiles of both the coolant and the duct walls throughout the core.

3.1 System description

Regarding the modeled system, DASSH offers built-in support for ducted fuel assemblies arranged within a hexagonal core configuration. Within this framework, the geometry of the core is defined by a set of parameters that govern the layout and dimensions of each fuel assembly and its surrounding coolant regions.

Each assembly features a bundle of fuel pins arranged in a hexagonal lattice. The pins may include wire wraps, which influence coolant mixing and heat transfer. Surrounding this pin bundle a structural duct forms the outer boundary of the assembly. A schematic representation of the relevant geometric features is provided in 3.1

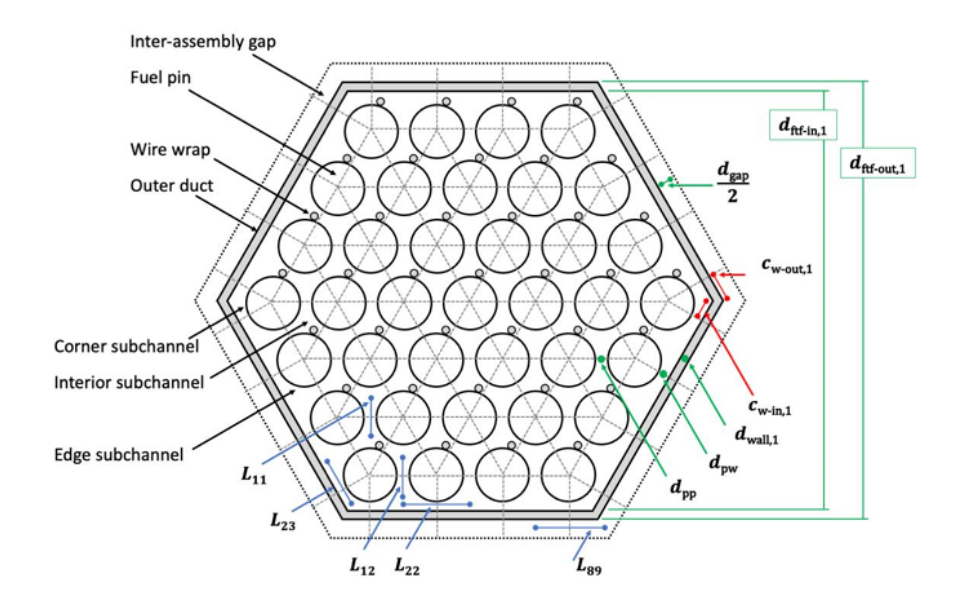


Figure 3.1: Dimensions and definitions applied to single-ducted assembly

To facilitate subchannel-based thermal-hydraulic analysis, DASSH divides each assembly into several flow regions. These include:

- Interior subchannels, located between clusters of three adjacent pins;
- Edge subchannels, situated between the outer pins and the duct wall;
- Corner subchannels, positioned near the assembly corners and bounded by a single pin.

In addition to single-duct designs, the software supports double-ducted assemblies, where a space exists between inner and outer duct walls. This region, referred to as the bypass gap, is also discretized into edge and corner subchannels. The number and arrangement of these subchannels mirror the partition of the adjacent duct wall, ensuring geometric consistency.

In the configuration of the Figure 3.1, the parameters defining subchannel spacing and assembly geometry are as follows:

- L_{11} : distance between two interior subchannel centroids;
- L_{12} : distance between an interior and an edge subchannel centroid;
- L_{23} : distance between an edge and a corner subchannel centroid;
- L_{89} : distance between an edge and a corner subchannel centroid in the interassembly gap;

- d_{pp} : pin-to-pin gap, i.e., minimum distance between the outer surfaces of two adjacent fuel pins;
- d_{pw} : pin-to-wall gap, measured between the pin surface and the inner flat of the duct wall:
- $d_{wall,1}$: thickness of the interior duct wall; if an outer duct is present, this refers to the first outer wall thickness;
- d_{gap} : inter-assembly gap, corresponding to the space between the outer duct walls of neighboring assemblies;
- $c_{w-in,1}$: length of the corner subchannel side adjacent to the **inner** surface of the first duct wall;
- $c_{w-out,1}$: length of the corner subchannel side adjacent to the **outer** surface of the first duct wall.
- $d_{\text{ftf,in,1}}$: flat-to-flat distance of the inner boundary of the first duct (inner duct-to-duct distance along the hexagonal flat);
- $d_{\text{ftf,out,1}}$: flat-to-flat distance of the outer boundary of the first duct (outer duct-to-duct distance along the hexagonal flat).

When modeling a full reactor core, coolant channels must also be defined in the regions between adjacent assemblies. These inter-assembly gaps are likewise divided into edge subchannels, which connect two neighboring assemblies and their associated bypass gaps, and corner subchannels, which interface with three assemblies and the corresponding subchannels in the adjacent gaps.

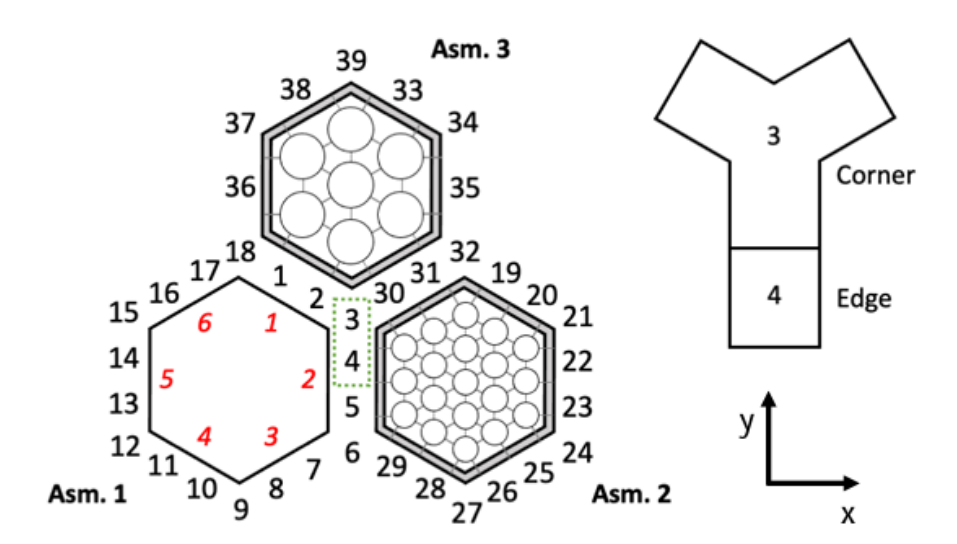


Figure 3.2: Inter-assembly gap subchannel configuration and indexing

The meshing of these outer regions is performed in a way that maintains subchannel alignment with the neighboring assemblies. Specifically, the number of edge and corner subchannels in the inter-assembly coolant region is matched to the assembly with the greatest number of pins.

3.2 Physics Modeled in DASSH

The thermal-hydraulic modeling approach adopted by DASSH is based on a reducedorder formulation. The core physical quantity computed by the code is the coolant temperature, obtained by solving a steady-state energy conservation equation applied to a network of interconnected subchannels. Each subchannel represents a distinct flow region through which the coolant flows axially along the fuel assembly.

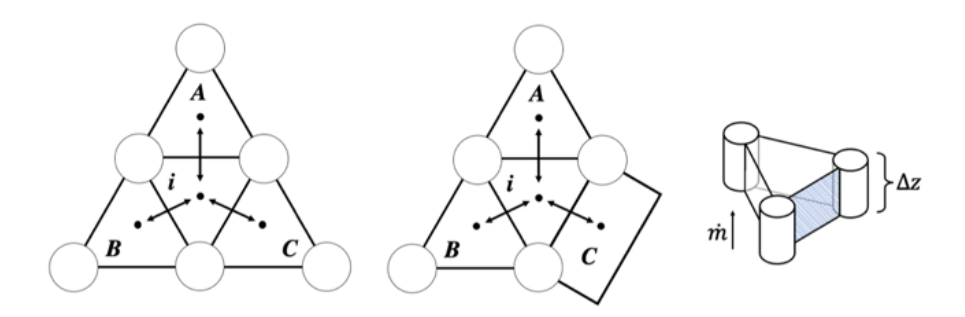


Figure 3.3: Subchannel adjacency for interior-type subchannels, for the other types the approach is the same.

3.2.1 Energy conservation law

DASSH does not solve the complete set of conservation equations for mass, momentum, and energy. Instead, it applies a streamlined methodology that solves only the energy conservation equation as a partial differential equation (PDE), while the effects of momentum and mass conservation are incorporated through algebraic relationships and network constraints.

The starting energy conservation equation, derivable by the general transport equation of any variable, is:

$$\frac{\partial(\rho h)}{\partial t} + \nabla \cdot (\rho h \vec{u}) = q''' + \psi + \nabla \cdot (\rho \alpha \nabla h) + [\text{Compressible fluid terms}] \quad (3.1)$$

where:

- $\rho = \text{material density (kg/m}^3)$
- $\vec{u} = \text{velocity vector (m/s)}$
- h = specific enthalpy (J/kg)
- q''' = volumetric heat generation (W/m³)
- ψ = work done against viscous forces (W/m³)
- α = fluid thermal diffusivity (m²/s)

In the equation 3.1, the first term represents the time-dependent change in enthalpy, while the second accounts for convective transport due to fluid motion. On the right-hand side, it include internal heat generation, viscous dissipation from shear stresses, and diffusive heat transport modeled through thermal diffusivity. For compressible flows, additional terms represent pressure work and energy changes due to fluid compressibility. Altogether, the equation balances all sources, sinks, and transport mechanisms of energy within the system.

Following the formulation of the energy conservation equation, DASSH applies it across the network of subchannels representing the core. Each subchannel, defined both axially and radially, is treated as a control volume with its own independent temperature field. The numerical solution proceeds along the axial direction, using finite difference approximations to evaluate energy exchange between successive axial planes as well as between adjacent subchannels in the radial direction. This discretization strategy allows for an efficient yet sufficiently detailed representation of temperature distributions throughout the coolant domain.

To simplify the model while retaining physical accuracy, the DASSH formulation of the energy equation adopts several assumptions: a steady-state regime, an incompressible coolant, and constant thermophysical properties within each

discretized subchannel. Under these conditions, certain terms in the general energy conservation law can be neglected, such as those related to time-dependence, viscous dissipation, and pressure work. Furthermore, gravitational effects are excluded, as forced convection dominates the flow field.

Additionally, thermal transport is simplified in both axial and radial directions. Heat conduction along the flow direction is assumed negligible compared to axial advection by the coolant. In the radial plane, conductive heat transfer is lumped and approximate considering the effects of turbulent mixing. This enhancement is achieved by increasing the thermal diffusivity with an eddy diffusivity derived from empirical correlations. Heat conduction through wire wraps, is not considered.

Applying these simplifications, the energy equation reduces to the following steady-state form:

$$\rho C_n \nabla \cdot (T\vec{u}) = q''' + \rho C_n \alpha \nabla \cdot \nabla T \tag{3.2}$$

In this reduced form, where the enthalphy is expressed as C_pT , the left-hand side represents advective transport of thermal energy in the axial direction, while the right-hand side incorporates internal heat generation within the fluid and effective radial conduction, which includes contributions from turbulent mixing.

Given the predominance of forced convection in the axial direction, the dominant heat transfer mechanisms in DASSH can be summarized as:

- 1. Axial advection of energy due to the bulk coolant flow;
- 2. Radial conduction within the coolant, enhanced to represent turbulent mixing;
- 3. Radial redistribution of energy driven by flow-induced mixing, particularly from the action of wire wraps.

The presence of wire wraps and duct walls gives rise to two characteristic flow behaviors in the radial plane showed in Figure 3.4. In the core interior, Region I, the helical wire promotes spiral coolant motion around the fuel pins, intensifying local turbulence and enhancing radial mixing. At the periphery, Region II, the same helical structure induces a broader, circumferential flow along the duct wall, encouraging thermal communication between edge subchannels. While these complex flow structures are not resolved explicitly, their net mixing effects are incorporated through empirically derived enhancements to radial diffusivity, ensuring their thermal-hydraulic impact is retained within the reduced-order model.

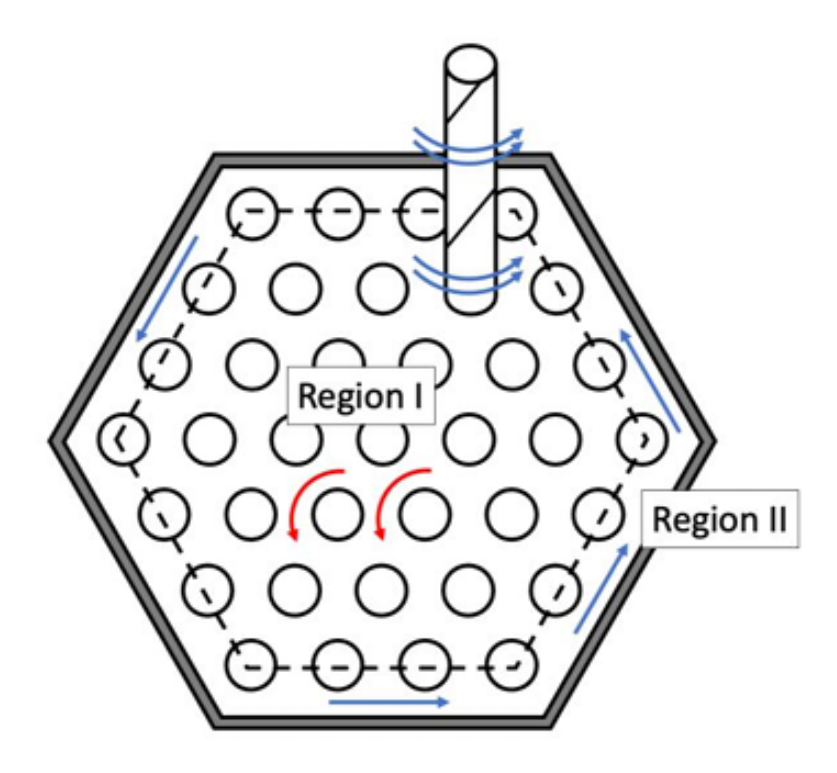


Figure 3.4: Two distinct coolant flow regions in a hexagonal ducted assembly: interior pin bundle and peripheral duct region.

To account for the intensified mixing in Region I, DASSH modifies the coolant's thermal diffusivity by introducing an additional eddy diffusivity term. This modeling approach allows radial convective transport—arising from turbulent mixing around the pins—to be represented as an enhancement to conductive heat transfer, rather than through explicit advection terms. The effective thermal diffusivity is defined as:

$$\alpha^* = \kappa \frac{k}{\rho C_p} + \varepsilon \tag{3.3}$$

where:

- $k = \text{fluid thermal conductivity } (W/m \cdot K)$
- κ = conduction shape factor
- $\varepsilon = \text{eddy diffusivity (m}^2/\text{s)}$

The first term represents the molecular thermal diffusivity of the fluid, multiplied by a geometry-dependent shape factor that adjusts heat conduction according to local configuration. The second term, ε , models the contribution of turbulence-induced mixing, particularly relevant in wire-wrapped regions. Under strong mixing conditions, ε can exceed the molecular term by more than an order of magnitude, making it the dominant mechanism for radial thermal transport.

In the absence of wire wraps, the eddy diffusivity vanishes (ε =0), eliminating the mixing enhancement despite the potential presence of turbulence. When multiplied by ρC_p , the Equation 3.3 yields an effective thermal conductivity, written as:

$$k^* = \kappa k + \rho C_p \varepsilon \tag{3.4}$$

So in Region I, where the described heat transfer regard the interior subchannels, the final governing equation for temperature, accounting for all previously stated assumptions, is given by:

$$\rho C_p v_{i,z} \frac{\partial T_i}{\partial z} = q_i^{\prime\prime\prime} + k^* \nabla_{xy} \cdot \nabla_{xy} T_i$$
(3.5)

where

- $v_{i,z}$ = axial velocity in subchannel i (m/s) defined as the volumetric flow rate divided by the cross-sectional area in the x-y-plane.
- q_i''' = volumetric heat source in subchannel i (W/m³)

To obtain the coolant temperature at each axial step, this equation is discretized using a finite volume approach. Applying the divergence theorem to the transverse conduction term and evaluating heat fluxes at subchannel interfaces using finite differences allows DASSH to compute temperature profiles along the axial direction, step by step. A more detailed description of the numerical implementation can be found in the DASSH theory manual [22].

For Region II, which includes edge and corner subchannels adjacent to the duct wall, coolant behavior is influenced by the continuous helical motion imposed by the wire wraps near the assembly boundary. This helical structure induces a pronounced circumferential component in the flow, commonly referred to as swirl flow. The strength of this rotational motion is characterized by the swirl velocity, defined as the ratio between the circumferential and the mean axial flow velocities.

In addition to swirl-induced mixing, heat transfer in Region II is further complicated by interaction with the solid duct wall. This introduces additional heat transfer mechanisms not present in the interior subchannels, namely, convective coupling with the duct and enhanced radial transport due to circumferential flow.

To account for these effects, the energy conservation equation for Region II is extended from Equation 3.1 to include source terms specific to this peripheral behavior:

$$\rho C_p v_{i,z} \frac{\partial T_i}{\partial z} = q_i^{"'} + q_s^{"'} + q_w^{"'} + k^* \nabla_{xy} \cdot \nabla_{xy} T_i$$
(3.6)

where:

- $v_{i,z} = \text{axial velocity in subchannel } i \text{ (m/s)}$
- q_i''' = volumetric heat source in subchannel i (W/m³)
- q_s''' = heat addition due to swirl-induced mixing (W/m³)
- q_w''' = heat addition from convective interaction with the duct wall (W/m³)

As in Region I, the energy conservation law is solved using the same numerical approach to obtain the temperature distribution axially, maintaining consistency with DASSH's modeling philosophy.

The additional heat transfer effects arising from swirl-induced mixing and duct wall interaction are both treated as convective mechanisms, allowing them to be modeled using heat transfer coefficients. For swirl-induced mixing, the heat exchange is expressed as:

$$q_s = h_s A_s (T_{s,j} - T_{i,j}) = \rho C_p v_s A_s (T_{s,j} - T_{i,j})$$
(3.7)

where:

- h_s = swirl heat transfer coefficient (W/m²K)
- $v_{\rm s} = {\rm swirl\ velocity\ (m/s)}$
- $A_{\rm s} = \text{area of swirl interaction (m}^2)$
- $T_{s,j}$ = temperature of neighbor from which swirl flow comes from (K)
- d_{pw} = distance between the pin and the duct wall (m)

For convection with the duct wall, the heat addition is given by:

$$q_w = h_{w,i} A_{w,i} (T_{w,i} - T_{i,i}) (3.8)$$

where:

- $h_{w,i}$ = coolant-to-duct heat transfer coefficient in subchannel i (W/m²K), obtained from Nusselt number correlations
- $A_{w,i}$ = heat transfer area between subchannel i and the duct wall (m²).

Together, these convective terms complete the energy balance in Region II, capturing the key thermal interactions of the Region II.

What remains to be addressed is the heat transfer in the bypass gap of double-ducted assemblies and the inter-assembly gap between adjacent units. These regions are composed of subchannels that interface with two coolant regions and two duct walls, similar in adjacency definition to edge subchannels in Region II. In the case of corner subchannels, the configuration involves three coolant regions and three duct walls, making the layout slightly more complex.

The governing energy balance remains consistent with that of Region II. However, since wire wraps are not present in the inter-assembly gaps, there is no contribution from swirl-induced mixing, and eddy diffusivity is not introduced. As a result, thermal transport in these gaps relies on the base thermal properties of the fluid, without enhancement.

Coolant flow in the inter-assembly gap is generally minimal and can be nearly stagnant, driven primarily by natural convection. Two modeling approaches can be used to represent this region, both approximating the coolant as stagnant and enabling the use of a significantly reduced axial mesh size requirement to ensure numerical stability:

- Conduction Model: In this approach, heat transfer occurs via conduction from the duct wall surface to the center of the inter-assembly gap. The total heat transfer is computed as the summation of all conduction paths between adjacent duct walls and all conduction connections with adjacent gap coolant subchannels.
- Duct-Average Model: This simplified approach assumes that the coolant temperature in the inter-assembly gap is equal to the average temperature of the adjacent duct walls.

Although these models significantly reduce computational cost, they introduce some errors in the energy balance.

3.2.2 Correlation built in DASSH

Momentum conservation is not solved explicitly in DASSH. Instead of resolving full velocity and pressure fields, DASSH incorporates momentum effects through a set of empirical and semi-empirical correlations. These include frictional pressure loss models, form loss coefficients associated with wire wraps and structural features, and crossflow correlations that approximate lateral mixing between subchannels.

Experimental results have enabled the development of correlations that characterize fluid flow in ducted, wire-wrapped hexagonal fuel bundles. DASSH use these

correlations to improve the prediction of fluid flow behavior and its impact on heat transfer, as summarized in Figure 3.5.

The friction factor is fundamental for evaluating the pressure drop, which is calculated using the Darcy-Weisbach equation:

$$\Delta p = f \frac{\rho v^2}{2} \frac{L}{D_e} \tag{3.9}$$

where:

- f = friction factor
- v = average velocity (m/s) in the rod bundle
- L = length (m) of the rod bundle
- D_e = equivalent hydraulic diameter (m)

DASSH updates the friction factor at each axial step to account for temperaturedependent property changes.

The flow split describes the distribution of flow across individual subchannels relative to the entire bundle. It is defined as the ratio of the axial velocity in a subchannel to the bundle-average axial velocity.

To avoid the coupling of energy and momentum conservation law, the two mixing parameters, swirl velocity and eddy diffusivity, are used to quantify lateral mixing between subchannels, which is critical to predict thermal and hydraulic behavior.

The convective heat transfer between the fluid and the wall is modeled using the Dittus-Boelter correlation, which relates the Nusselt number to the Reynolds and Prandtl numbers, allowing for the estimation of the local heat transfer coefficient within the subchannels.

Mass conservation is also not enforced through a differential form of the continuity equation. Instead, it is applied implicitly via the prescribed inlet flow rates and the subchannel network structure. Flow continuity is ensured by maintaining a balance between the total mass flow entering and exiting each assembly or control volume, even though no explicit solution of the continuity equation is performed.

This reduced-order treatment of the governing equations allows DASSH to perform fast and robust simulations of large reactor cores while retaining the essential thermal-hydraulic behavior needed for analysis. By focusing computational effort on energy transport while using physically grounded correlations for momentum and flow distribution, the code strikes a balance between accuracy and efficiency, making it well suited for design and safety applications in fast reactor systems.

M	lixing	1	Flow spli	t		В	undle frie	ction facto	or	-	
Cheng-Todreas	Chiu-Rohsenow- Todreas	Cheng-Todreas	Chiu-Rohsenow- Todreas	Novendstern	Upgraded Cheng- Todreas (detailed)	Cheng-Todreas (simple)	Cheng-Todreas (detailed)	Engel	Rehme	Novendstern	Investigators
CT/UCT	MIT	CT/UCT	MIT	NOV	UCTD	CTS	CTD	ENG	REH	NOV	ID
	1978		1980		2018	1986	1986	1979	1973	1972	Year
Same as Chen	1.067 – 1.315	Same as Chen	1.063 – 1.28		1.0 – 1.42	1.025 – 1.42	1.0 - 1.42	1.067 – 1.082	1.1 – 1.42	1.06 - 1.42	P/D
g-Todreas (d	4.0 - 52.0	g-Todreas (de	4.0 - 52.0	Same as N	8.0 – 52.0	8.0 – 50.0	4.0 - 52.0	7.7 – 8.3	8.0 – 50.0	8.0 – 96.0	d/H
etailed or up	7-217	etailed or up	7-217	lovendstern	7-217	19 – 217	19 – 217	19-61	7-217	19 – 217	N _r
Same as Cheng-Todreas (detailed or upgraded-detailed) bundle friction factor	Turbulent (?? – f??)	Same as Cheng-Todreas (detailed or upgraded-detailed) bundle friction factor	Transition, turbulent (4500 – 8.1e4)	Same as Novendstern bundle friction factor	Laminar, transition, turbulent (50 – 1e6)	Laminar, transition, turbulent (50 – 1e6)	Laminar, transition, turbulent (50 – 1e6)	Laminar, transition, turbulent (50 – 1e5)	Transition, turbulent (1000 – 3e5)	Transition, turbulent (2600 – 1e5)	Flow regime (Re)
1 factor	No	ı factor	No		Yes	No	Yes	No	No	No	Bare rod

Figure 3.5: Summary of DASSH Correlations [22]

3.2.3 Duct walls treatment

Ducts in both single and double ducted assemblies are bounded by coolant on both sides and modeled using a simplified one-dimensional conduction approach. Ideally, heat transfer between the coolant and duct wall would be resolved at the same axial plane, reflecting the fully coupled thermal system. However, because the duct interfaces with coolant on both sides, solving for wall temperatures simultaneously would overconstrain the system and require a more complex formulation.

To simplify this, DASSH introduces an axial lag: duct wall temperatures at axial plane y+1 are computed only after coolant temperatures at the same plane are known. These wall temperatures are then used in the coolant temperature calculation at plane y+2. This approach reduces computational complexity while maintaining accuracy, especially when the axial mesh is sufficiently fine. Additionally, axial conduction through the duct and conduction between adjacent duct cells are considered negligible and are therefore omitted from the model.

Heat transfer in the assembly corner regions is assigned entirely to the outer surface area associated with corner subchannels. This applies both to the coolant-side corner subchannels and the corresponding duct wall locations. For example, convective heat transfer in a corner subchannel of a pin bundle is applied to the outer-facing corner surface, rather than the interior-facing one. This treatment ensures energy conservation by using the same surface area for heat transfer on both the coolant and duct sides. The effect of this modeling choice on temperature distribution is minimal and does not significantly impact accuracy.

3.2.4 Numerical stability

Ensuring numerical stability in DASSH requires careful treatment of both spatial mesh alignment and axial discretization. One key challenge arises at inter-assembly gaps, where adjacent fuel assemblies may contain different numbers of pins, leading to misaligned subchannel meshes at shared boundaries. To accurately model heat transfer across these nonconforming interfaces, the inter-assembly gap is discretized using the finer of the two adjacent meshes. DASSH resolves the mismatch through a pair of conservative operations: coarse wall temperatures are projected onto the finer inter-assembly gap mesh, while temperatures from the finer mesh are restricted back onto the coarser wall mesh when required. This ensures thermodynamic consistency across interface boundaries without enforcing strict mesh conformity, thus improving computational efficiency and allowing for more flexible assembly configurations. A drawback of these projection and restriction operations, however, is that although they conserve the overall energy balance, they also introduce numerical diffusion, leading to an unphysical spreading of heat across the inter-assembly gap.

Beyond the mesh mismatch shown in Figure 3.6, a more fundamental limitation on stability is introduced by the axial marching scheme employed in DASSH.

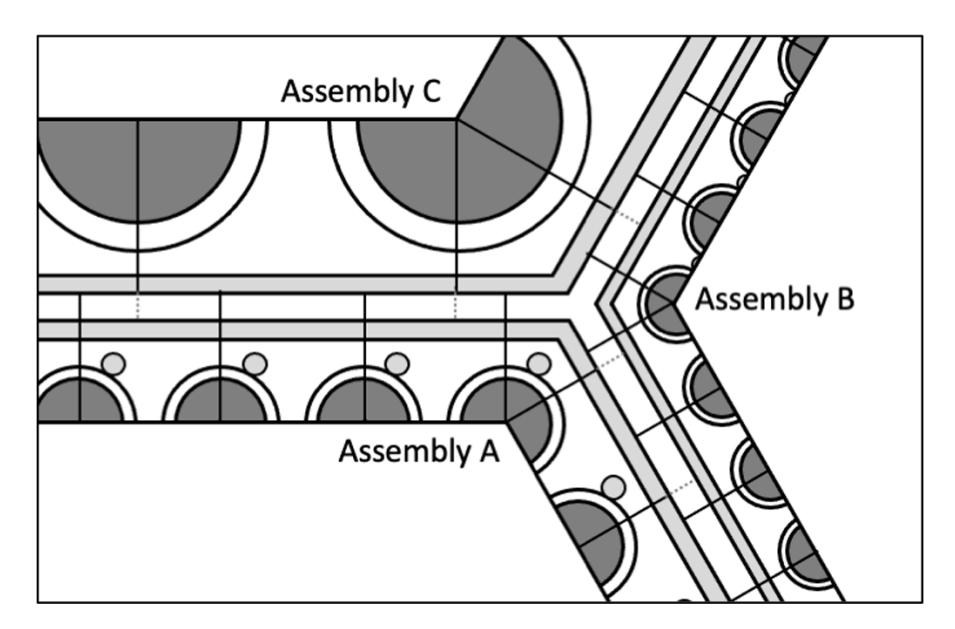


Figure 3.6: Disagreement in meshing schemes between neighboring assemblies

The code advances the solution using a forward differencing method in the axial direction, which is conditionally stable and sensitive to the choice of axial mesh size. In particular, when the mesh is too coarse, unphysical results such as negative coolant temperatures may occur, especially in subchannels experiencing high energy loss and low mass flow. To avoid this, an axial mesh size constraint is imposed across the domain based on an extreme-case assumption: that a subchannel receives no internal heating, and the adjacent fluid temperature are are at zero. The condition that the resulting coolant temperature remains non-negative sets a lower bound on the axial resolution. This constraint is evaluated for all subchannels, and the most restrictive value is applied globally to ensure stability.

The need for fine axial resolution becomes even more pronounced in regions where flow conditions depart from the forced convection regime. DASSH assumes that axial transport is dominated by inertia-driven flow; however, when coolant flow is low and thermal power is high, buoyancy forces driven by temperature-induced density gradients can become significant. In such cases, natural convection may contribute appreciably to axial transport, potentially violating the forced convection assumption on which the marching scheme is based. To assess the risk of this breakdown, DASSH introduces a predictive indicator based on a modified Grashof number, Gr*, defined as:

$$Gr^* = \frac{Gr}{\chi \operatorname{Re}^2} \tag{3.10}$$

where Gr is the classical Grashof number, Re is the Reynolds number based on

the axial velocity and hydraulic diameter of the subchannel, and χ is a correction factor that accounts for power skew within the assembly. When $Gr^* \geq 0.02$, buoyancy effects are considered non-negligible, indicating that natural convection may significantly influence the local flow field and invalidate the forward-marching solution.

To maintain stability and accuracy under the assumptions built into the DASSH framework, users must therefore select an axial mesh size that satisfies two key criteria: (1) it must be small enough to prevent non-physical temperature behavior under extreme thermal gradients, and (2) it must ensure that the flow regime remains safely within the bounds of forced convection, or else trigger appropriate modeling considerations where that assumption fails. This dual requirement emphasizes the importance of resolution in thermal-hydraulic simulation and highlights the limitations of axial-marching approaches in regimes where buoyancy cannot be ignored.

3.2.5 Energy balance modeling

The thermal condition in DASSH is governed also by an energy balance that independently tracks heat contributions within individual subchannels of each assembly and across the inter-assembly gap regions. This approach ensures that all heat sources and transport mechanisms are consistently incorporated throughout the simulation.

Within each assembly, the coolant receives energy primarily from fuel pin heat generation. In subchannels adjacent to duct walls, particularly edge and corner regions, additional energy is exchanged through convective interaction with the surrounding structure. These convective transfers are evaluated at each axial step using standard heat transfer formulations.

Each axial segment of the domain maintains a local energy balance, which is accumulated to form the overall energy amount for each assembly. The total energy balance at the assembly level accounts for contributions from internal heating, convective interactions with duct walls, and the energy required to raise the coolant temperature:

$$Q_{\rm in} + Q_{\rm conv} - Q_{\Delta T} = 0 \tag{3.11}$$

Here, $Q_{\rm in}$ is the energy added from heat generation, $Q_{\rm conv}$ is the net energy exchanged with the duct walls through convection, and $Q_{\Delta T}$ represents the energy required to achieve the resulting coolant temperature rise. The last term is evaluated as:

$$Q_{\Delta T} = c_p \sum_{i=1}^{N} \dot{m}_i \Delta T_i \tag{3.12}$$

where c_p is the average specific heat capacity, \dot{m}_i is the mass flow rate in subchannel i, and ΔT_i is the corresponding temperature rise.

In the inter-assembly region, energy is gained or lost through convection with adjacent duct surfaces. If fluid flow is present in the gap, $Q_{\Delta T,gap}$ is evaluated analogously to quantify the temperature rise of the flowing coolant. Otherwise, energy may accumulate if the gap model does not include flow.

The core-wide energy balance aggregates contributions from all assemblies and the inter-assembly coolant:

$$\sum_{a=1}^{N_{\text{asm}}} Q_{\text{in},a} - \sum_{a=1}^{N_{\text{asm}}} Q_{\Delta T,a} - Q_{\Delta T,\text{gap}} = 0$$
(3.13)

This equation accounts for heating in fuel, duct, and coolant, as well as the thermal response of all coolant regions. Minor deviations from perfect balance (typically below 1% of total core power) can arise due to time lags between coolant and duct wall temperature updates or the use of stagnant-gap models, which prevent immediate heat removal.

3.3 Comparison with CFD: Advantages and Limitations

Benchmarking of DASSH requires comparison with either experimental measurements or CFD simulations. CFD tools such as STAR-CCM+ model fluid flow and heat transfer in great detail, providing insight into the thermal-hydraulic behavior of assemblies. It is important to note, however, that CFD results are themselves approximations and do not constitute absolute reality. In this work, CFD is used as a reference for verification purposes, and DASSH results are compared with STAR-CCM+ across representative system configurations. In this thesis, STAR-CCM+ is used as a detailed benchmark to assess how effectively DASSH's modeling assumptions reproduce the main thermal-fluid behavior in reactor subassemblies.

To ensure a consistent comparison, the CFD simulations were set up as follows: STAR-CCM+ was selected as the CFD platform for this work due to its multiphysics capabilities, automated meshing features, and robust turbulence modeling framework. For each case studied, a high-quality computational mesh was generated to resolve both axial and lateral temperature and velocity gradients within the flow domain.

The simulation domains included all relevant fluid and solid regions, such as coolant passages, fuel pin spacing, and duct structures. Efforts were made to preserve geometric fidelity and minimize simplifications to maintain alignment with the DASSH modeling domain. Mesh refinement was concentrated in wall-bounded

regions and in areas of expected high thermal or velocity gradients, such as near duct walls or between subchannels.

Boundary conditions in STAR-CCM+ were chosen to mirror the DASSH configuration as closely as possible. These included:

- Specified inlet mass flow rate and bulk coolant temperature,
- Uniform or axially distributed heat input representative of fuel pin power,
- Symmetry or adiabatic outer wall conditions as appropriate,
- Temperature-dependent or constant material properties, depending on the case.

Turbulence was modeled using a RANS approach with a suitable closure model, such as the $k-\omega$ SST model. Convergence was assessed using residual trends, mass and energy conservation checks, and mesh independence studies to ensure solution robustness.

Postprocessing focused on extracting area-averaged coolant temperatures in each subchannel, axial temperature profiles, and local wall heat fluxes. These CFD results were resampled to match the spatial resolution used in DASSH, enabling direct comparison for benchmarking purposes. This setup provides a consistent reference to evaluate the accuracy and range of applicability of DASSH's modeling assumptions.

3.3.1 Fundamental Differences Between DASSH and CFD

DASSH and CFD tools like STAR-CCM+ differ significantly in their modeling philosophies, mathematical formulations, and computational strategies. Understanding these distinctions is essential for interpreting the results of benchmarking exercises and identifying where agreement is expected or where discrepancies may arise.

Governing Equations and Solution Approach. CFD tools solve the full, three-dimensional Navier–Stokes and energy equations, providing detailed modeling of fluid dynamics, including pressure gradients, turbulence, and thermal boundary layers. To represent turbulence, a range of modeling approaches is available, each with varying levels of accuracy and computational demand.

At the highest accuracy, Direct Numerical Simulation (DNS) resolves all scales of turbulence without any modeling assumptions. However, DNS is computationally prohibitive for engineering applications due to the fine spatial and temporal resolution required.

Large Eddy Simulation (LES) provides a compromise by resolving large-scale turbulent structures explicitly while modeling the smaller, sub-grid-scale eddies. LES offers improved accuracy over time-averaged models but still demands significant computational resources.

For practical engineering use, especially when high-performance computing (HPC) resources are limited, Reynolds-Averaged Navier–Stokes (RANS) models are widely adopted. RANS approaches time-average the Navier–Stokes equations, modeling the effects of turbulence through additional transport equations (e.g., the k- ϵ or k- ω models). This allows for the simulation of complex flows with significantly reduced computational cost and is the approach used in this work.

Dimensionality and Spatial Resolution. STAR-CCM+ models the system geometry in full three dimensions, capturing local flow fields, cross-channel mixing, and thermal stratification. DASSH, on the other hand, employs a one-dimensional axial discretization for each subchannel, with lateral coupling to account for crossflow and energy exchange between neighboring channels. This reduced-order approach lowers spatial resolution but enables rapid analysis of core-wide behavior.

Turbulence Modeling. CFD simulations include turbulence models that aim to capture eddy-driven transport and local flow disturbances. In DASSH, lateral mixing and turbulence effects are represented using empirical or semi-empirical mixing coefficients, which are often tuned to match experimental data. While effective on average, this approach may miss localized phenomena unless carefully calibrated.

Geometry and Boundary Detail. In CFD, complex features like spacer wires, detailed pin bundles, or duct wall conduction can be explicitly modeled. In DASSH, such effects are homogenized through model assumptions and correlation-based adjustments. This results in faster simulation times but reduced accuracy in regions with geometric discontinuities.

Computational Efficiency. A major strength of DASSH lies in its computational efficiency: it can simulate full-core thermal-hydraulic conditions within minutes on standard computers. CFD simulations, especially for large or high-resolution domains, may require hours to days of runtime on high-performance computing systems.

Typical Applications. DASSH is well suited for design studies, safety margin evaluations, and parametric sweeps. CFD is typically reserved for studies, verification work, or exploration of local phenomena where modeling assumptions in

reduced-order tools may break down.

These fundamental differences frame the context for all benchmarking efforts. The objective is not to expect perfect agreement between DASSH and CFD, but rather to understand the sources of deviation and improve confidence in the applicability of DASSH.

3.3.2 Limitations

Although CFD tools like STAR-CCM+ offer a higher accuracy view of thermal-hydraulic phenomena, several limitations must be considered when using CFD for benchmarking purposes.

First, despite solving nearly the full governing equations, CFD results remain sensitive to turbulence modeling, wall functions, and mesh resolution particularly in duct regions and near spacer wires if present. These aspects may introduce discrepancies between CFD results and experimental data, or between different CFD tools themselves.

Second, matching DASSH and CFD inputs exactly is challenging. While effort is made to align boundary conditions, geometry interpretation, and material properties, differences in how subchannel boundaries are defined or how mixing is treated can lead to divergence in results that do not strictly originate from model accuracy.

Third, CFD simulations are resource-intensive and impractical for full core or large-scale parametric studies. As a result, benchmarking is limited to selected configurations, and conclusions must be cautiously extrapolated.

On the other hand, DASSH's reduced order assumptions impose known limitations: the mixing coefficients are empirical, the momentum conservation equations are not solved, and duct wall conduction is simplified. However, DASSH's speed and scalability make it highly useful for reactor analysis, provided its range of validity is understood.

By comparing DASSH predictions with detailed CFD data, this benchmarking study aims to:

- Identify systematic biases in DASSH predictions,
- Verify its subchannel energy balance formulation,
- Determine scenarios where the simplified physics yield acceptable results,
- Highlight regions where model refinement or correction factors may be necessary.

The ultimate goal is not to replace CFD with DASSH or vice versa, but to define their complementary roles in advanced reactor analysis. CFD provides detailed insight into local flow and heat transfer, while DASSH enables rapid evaluation of system-wide behavior across a broad design space.

Chapter 4

Benchmarking of DASSH: Case Studies

In this chapter, the benchmarking work is presented and reproduced. For each case, the results obtained with DASSH are compared against those from STAR-CCM+ in order to verify DASSH. Each model is organized into a section that first provides a description of the system under study, followed by a presentation of the results from both software tools, and finally a discussion of the differences and relative errors observed.

4.1 Case Study 1

The first case study consists of the reproduction of a benchmark already performed and reported in the literature by ANL [23]. The system modeled was designed to test the limits of DASSH accuracy under unfavorable conditions, particularly in regimes characterized by strong temperature gradients. This case was selected to assess the reliability of DASSH predictions in situations where accurate modeling of thermal stratification and flow redistribution is essential.

4.1.1 System Description

The system analyzed consists of a central fuel assembly of the VTR(Versatile Test Reactor)¹type with 217 pins, surrounded by six shield assemblies, each of the 61-pin type. The main geometric features of the two types of assemblies are summarized

in the table 4.1.

Table 4.1: Geometric parameters for Type 1 and Type 2 assemblies.

Parameter	Type 1	Type 2	
Number of pins	217	61	
Pin pitch (cm)	0.7432	1.3625	
Pin diameter (cm)	0.6282	1.2620	
Duct inner flat-to-flat (cm)	11.154	11.154	
Duct outer flat-to-flat (cm)	11.757	11.757	
Wire wrap	No	one	
Assembly pitch (cm)	12.078		
Inter-assembly gap width (cm)	0.32055		
Core length (cm)	384	1.50	

In the system, the outer domain is isolated through a boundary condition applied at the edge. No power generation in the pins is present. Instead, an inlet coolant temperature of 800 °C is imposed at the central assembly, with a sodium mass flow rate of 1 kg/s. The surrounding assemblies are each supplied with an inlet coolant temperature of 350 °C and a flow rate of 0.25 kg/s. The flow rate in the inter-assembly gap is imposed as 10% of the total system flow, corresponding to 0.278 kg/s.

For the present study, constant, temperature-independent thermophysical properties were adopted for both the coolant and structural materials. The selected values are summarized in Table 4.2.

Table 4.2: Thermophysical properties of sodium and HT9.

Property	Value	Units
Density (sodium)	850.25	${\rm kg/m^3}$
Viscosity (sodium)	2.7127E-4	$Pa \cdot s$
Thermal conductivity (sodium)	70.426	$W/m \cdot K$
Heat capacity (sodium)	1274.2	$J/kg \cdot K$
Thermal conductivity (HT9)	26.468	$W/m \cdot K$

¹The VTR is thermal-hydraulics test facility developed to generate experimental measurements on a full-scale assembly with prototypic axial reflectors, fuel, and plena in USA [24]

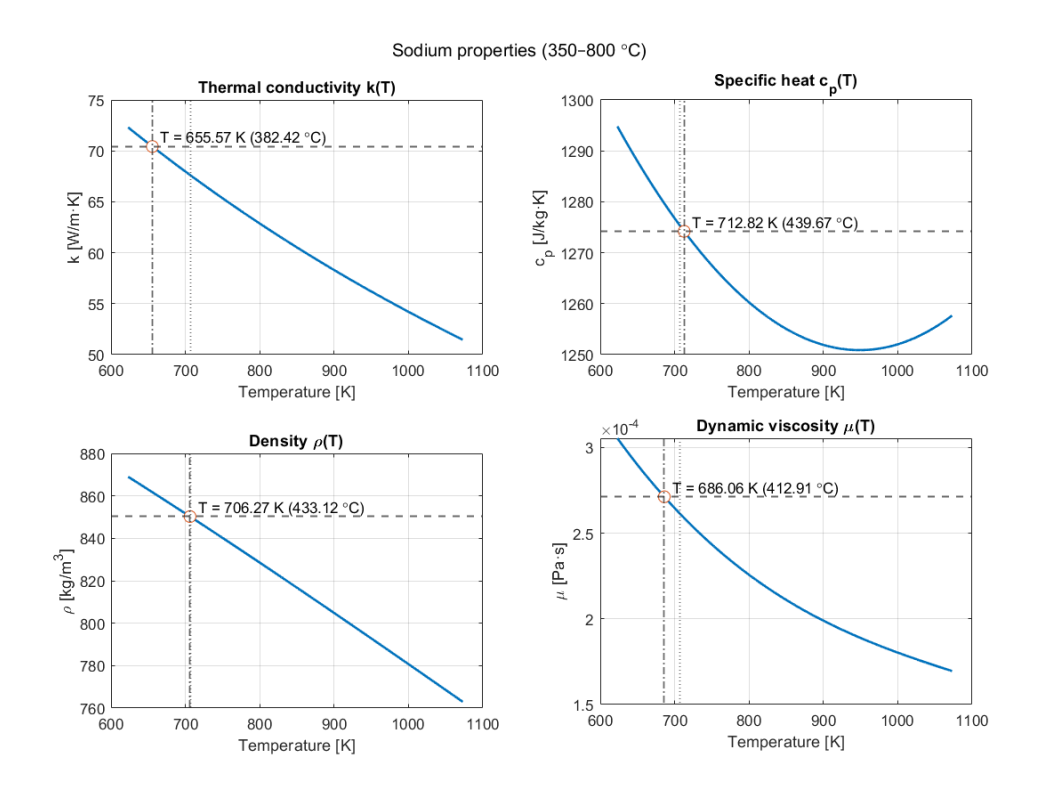


Figure 4.1: Temperature-dependent sodium properties compared with the constant reference values used in the study. The equation used are the 4.13,4.14, 4.15 and 4.16

The thermophysical properties of sodium (density, viscosity, thermal conductivity, and specific heat) were considered constant with temperature. This assumption is justified because the present case study reproduces the conditions and modeling approach of the reference work [23], where the same simplification was adopted to ensure consistency with the published results.

Over the investigated temperature range (350–800 °C), the distance of the constant properties from the minimum and maximum values of each property is as follows:

- Thermal conductivity k [W/m·K]: Constant value = 70.426 Minimum = 51.453, Maximum = 72.297 Distance from minimum = 36.87% Distance from maximum = 2.59%
- Heat capacity c_p [J/kg · K]: Constant value = 1274.2 Minimum = 1250.9, Maximum = 1294.8

Distance from minimum = 1.86%Distance from maximum = 1.59%

• Density ρ [kg/m³]: Constant value = 850.25 Minimum = 762.91, Maximum = 868.97 Distance from minimum = 11.45% Distance from maximum = 2.15%

• Viscosity μ [Pa·s]: Constant value = 2.7127×10^{-4} Minimum = 1.6951×10^{-4} , Maximum = 3.0532×10^{-4} Distance from minimum = 60.03%Distance from maximum = 11.15%

The distances of the constant properties from the minimum and maximum values over the investigated temperature range are calculated as:

$$\delta_{\min} = \frac{P_{\text{ref}} - P_{\min}}{P_{\min}} \times 100\%, \quad \delta_{\max} = \frac{P_{\max} - P_{\text{ref}}}{P_{\max}} \times 100\%$$
 (4.1)

where P_{ref} is the constant property used in the study, and P_{min} and P_{max} are the minimum and maximum values of the property over the temperature range 350–800 °C.

These variations primarily affect local temperature predictions. For the narrower 350–550 °C range often considered in reference studies, the errors are moderate; however, over the full 350–800 °C range, the assumption of constant properties could introduce solution errors if a real simulation were performed.

Nevertheless, adopting constant properties provides several advantages in this study:

- 1. Faithfully reproduces the conditions and results of the reference study;
- 2. Reduces numerical complexity, allowing focus on the main thermo-hydraulic behavior of the system;
- 3. Ensures direct comparability between the present results and the literature data.

The same approach was applied to the structural material HT9. The thermal conductivity k(T) of HT9 varies between approximately 24.5 and 26.3 W m⁻¹ K⁻¹ over the considered temperature range (350–800 °C). The constant value adopted in this work, k = 26.468 W m⁻¹ K⁻¹, slightly overestimates the property by about 7.9% relative to the minimum and by only 0.6% relative to the maximum of the temperature-dependent correlation.

This moderate overestimation is acceptable for the purposes of the present study, as it simplifies the thermal analysis while introducing only a limited deviation

from the detailed temperature-dependent behavior of HT9. Nevertheless, for high-precision heat-transfer or materials modeling, the full temperature-dependent expression should be preferred.

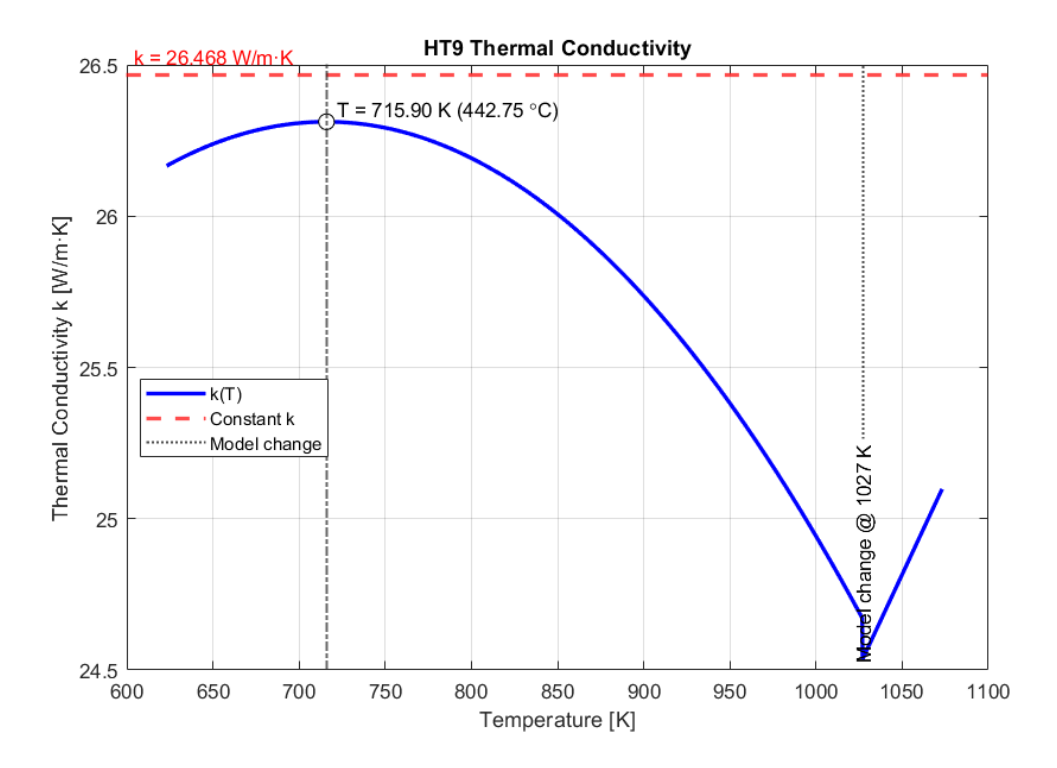


Figure 4.2: Thermal conductivity profile depending on temperature

In summary, using temperature-independent properties does not compromise the validity of the model but preserves methodological consistency and enables a clearer comparison with the original study.

4.1.2 DASSH model

After defining the geometrical features of the system in DASSH, it was necessary to specify the correlations used to model coolant behavior. The resistance to flow along the subchannels, which governs the axial pressure drop, was captured using a friction factor correlation based on the improved Cheng–Todreas approach. The distribution of coolant among the subchannels, ensuring realistic flow splitting, was also represented using the upgraded Cheng–Todreas methodology. Crossflow and turbulent mixing effects, which have a minor impact in this case since no wirewrap spacers are present, were incorporated through the original Cheng–Todreas correlation. Finally, the convective heat transfer between the coolant and the

cladding was determined using a Nusselt number correlation, specifically through the Lyon-Martinelli equation. In addition, a shape factor was applied to account for geometry-dependent effects on coolant mixing due to the arrangement of the pins. The correlation proposed by Shih-Kuei Cheng was adopted [25], expressed as:

$$k = 0.66 \frac{P}{D} \left(\frac{c}{D}\right)^{-0.3} \tag{4.2}$$

where c is the gap between rods (mm), D is the rod diameter (mm), and P is the rod pitch. This correlation is valid only for rod bundles without wire-wrap spacers. Using this formulation, the shape factor values obtained were 1.2995 for the Type 1 assembly and 1.5223 for the Type 2 assembly.

The mesh disagreement that can arise in DASSH, already discussed in Chapter 3.2.4, is the main issue to monitor during this case study and the following ones. In particular, the reference model system is challenging because of several factors that enhance the impact of numerical diffusion. The large thermal contrast between the central fuel assembly and the neighboring shields tends to exaggerate the spreading of temperature fields across the interfaces. Moreover, since the flow rates are relatively small and no wire-wrap spacers are present, the coolant within the assemblies undergoes only limited internal mixing, which would otherwise help smooth temperature differences. Finally, the low flow regime makes cross-assembly heat exchange comparatively more relevant; the flow levels here are one to two orders of magnitude lower than in typical fast reactor fuel assemblies, thereby magnifying the role of numerical diffusion in the predictions.

4.1.3 STAR CCM+ model

To verify the impact of numerical diffusion in DASSH, a complementary model was developed in STAR-CCM+. The system geometry was first created in SolidWorks and subsequently imported into STAR-CCM+, where the CFD setup was implemented. This approach offers a high accuracy reference solution that can be used to benchmark DASSH predictions in the absence of experimental data.

The hydraulic and thermal behavior of the system was investigated through a conjugate heat transfer calculation, enabling energy conduction within the solid regions by applying the Segregated Solid Energy model under steady-state conditions. The solid pins in the fuel and shield assemblies were not modeled explicitly; instead, their surfaces were treated with adiabatic boundary conditions, consistent with the assumptions adopted in of no power generation. In addition, wire-wrap spacers were omitted from the geometry.

For the coolant domain, the flow was modeled as steady-state, with the governing RANS equations solved using the $k-\omega$ Shear Stress Transport (SST) turbulence model, which offers superior accuracy for fuel assembly simulations.

The k- ω SST model is an advanced formulation derived from the standard k- ω model, which itself is an evolution of the k- ε model. In the k- ε approach, two additional transport equations are solved for k, the turbulent kinetic energy defining the velocity scale, and ε , the dissipation rate of turbulent eddies defining the length scale. This model generally performs better in the free-stream (bulk) flow regions. Conversely, the k- ω model solves for k and ω , the turbulence frequency, inversely proportional to the turbulence time scale and related to ε by $\varepsilon = k \cdot \omega$. Turbulent viscosity links k and ω , ensuring a consistent characterization of turbulence, and this formulation performs best near walls.

The SST variant combines the strengths of both models: it behaves like a $k-\varepsilon$ model in the bulk flow region, where the $k-\varepsilon$ formulation is more accurate, and switches to a $k-\omega$ formulation near walls, where the $k-\omega$ model is superior in resolving boundary layers. This blending is achieved by adding a cross-diffusion term to the RANS equations, allowing accurate prediction of near-wall effects, which are critical for modeling the complex coolant flow inside fuel assemblies.

It is also important to note that, while the recommended number of prism layers for wall-resolved turbulence modeling is typically between 8 and 12, in this study it was necessary to reduce the number of prism layers to 2. This adjustment was required due to the high mesh density, which would otherwise result in an unmanageably large computational file for practical computer resources, without significantly compromising the accuracy in the context of this fuel assembly simulation. The $Segregated\ Flow\$ and $Segregated\ Fluid\ Temperature\$ solvers were employed, assuming constant sodium properties. Near-wall behavior was captured using all y^+ wall treatment.

For the coolant domain, mass flow rate and temperature were specified at the inlet, while the outlet was defined with a standard outflow boundary condition, without imposing additional constraints. For solid walls, adiabatic conditions were applied everywhere except at the symmetry planes used for domain reduction. The outermost surfaces delimiting the system were also treated as adiabatic.

To reduce computational cost, the symmetry of the problem was exploited and only one-quarter of the full domain was modeled. The mesh was generated using the directed meshing operation. For the inlet region, an automated meshing approach was applied with the parameters summarized in Table 4.3.

Table 4.3: Meshing parameters for the inlet region.

Parameter	Value
Mesher	Polygonal
Base size	$1 \mathrm{mm}$
Target surface size	100% of base size
Minimum surface size	10% of base size
Number of prism layers	2
Total prism layer thickness	$0.3 \mathrm{\ mm}$

The resulting prism layer configuration produced wall y^+ values of 3.7 for the Type 1 assembly, 1.5 for the Type 2 assembly, and 1.1 for the inter-assembly gap channel. Since the viscous sublayer is well-resolved when $y^+ \approx 1$, these values confirm that the steep property gradients at the walls were adequately captured.

Along the axial direction, the mesh was refined using 240 layers, ensuring an appropriate distribution of volumes along the full height of the model.

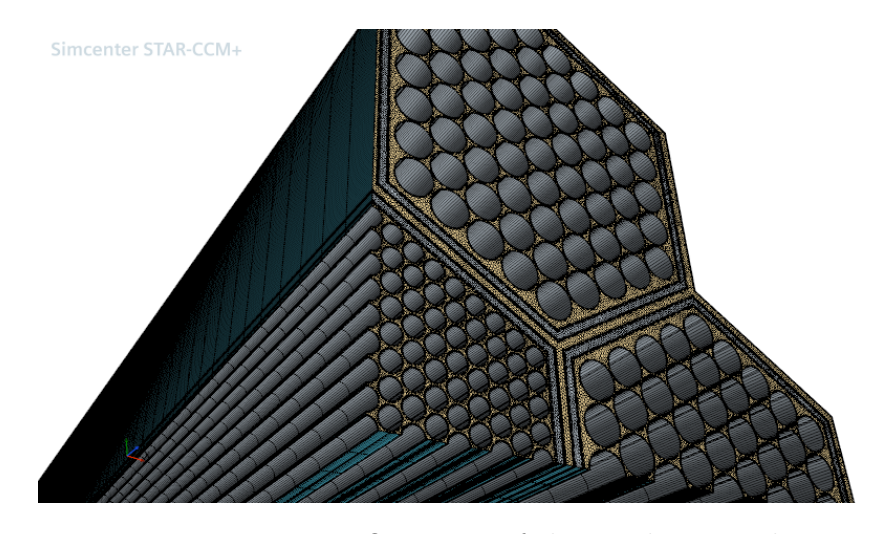


Figure 4.3: Overview of the resulting mesh

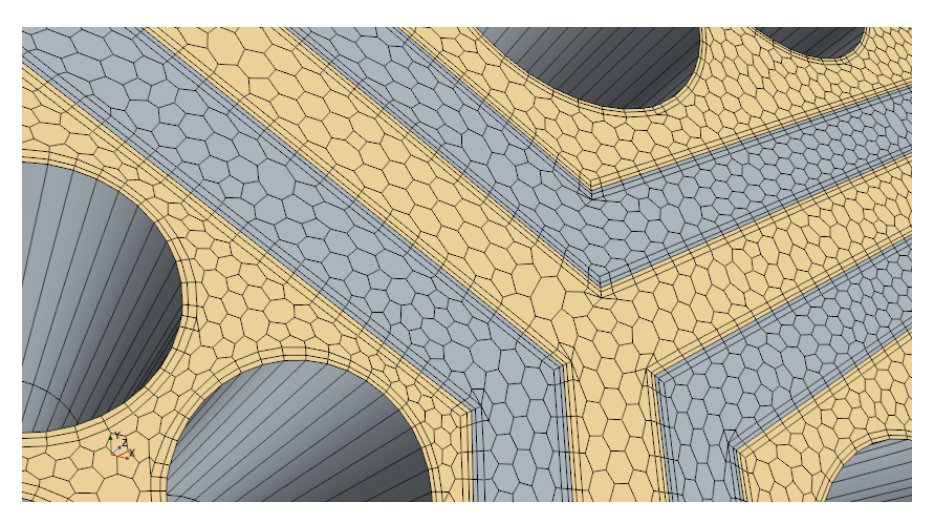


Figure 4.4: Mesh focus

Grid Independence Analysis

A numerical study was carried out to assess the sensitivity of the numerical solution to mesh refinement, using as reference the outlet average temperature of the Type 1 assembly. Three mesh resolutions were evaluated—coarse, medium, and fine. As expected, refining the mesh increases the total number of computational cells, which in turn raises the computational cost. The main mesh characteristics and convergence metrics are summarized in Table 4.4.

Table 4.4: Grid independence results for the first case study

Mesh Type	Base size [m]	# Fluid cells	Ou	Continuity
Coarse	1×10^{-2}	3.70×10^{6}	4.80×10^{-13}	7.70×10^{-11}
Medium	5×10^{-3}	6.70×10^{6}	4.20×10^{-13}	3.10×10^{-11}
Fine	1×10^{-3}	9.87×10^{6}	1.97×10^{-13}	1.26×10^{-11}

The objective of this analysis was to quantify the numerical error and evaluate the overall uncertainty of the computed results. Richardson extrapolation was employed to estimate the asymptotic value of the quantity of interest, i.e., the average outlet temperature.

A directed mesh was used, maintaining a fixed axial spacing of 16 mm while refining the grid in the x-y plane by varying the base size. This configuration produces an anisotropic mesh, with differing element sizes along the axial and lateral directions. For the three meshes used here we take the characteristic sizes proportional to the base sizes, so

$$h_1 = 1 \times 10^{-3}, \quad h_2 = 5 \times 10^{-3}, \quad h_3 = 1 \times 10^{-2},$$

and hence the refinement ratios are

$$r_{21} = \frac{h_2}{h_1} = 5.0, \qquad r_{32} = \frac{h_3}{h_2} = 2.0.$$

The characteristic mesh size was computed as the geometric mean of the grid spacings:

$$h_{\text{char}} = (\Delta x \, \Delta y \, \Delta z)^{1/3}. \tag{4.3}$$

Since Δz is constant, variations in h_{char} reflect lateral refinement.

The observed order of convergence p was determined iteratively from the differences between solutions on successive meshes:

$$p = \frac{1}{\ln(r_{21})} \left[\ln\left(\frac{\varepsilon_{32}}{\varepsilon_{21}}\right) + q(p) \right], \quad q(p) = \ln\left(\frac{r_{21}^p - s}{r_{32}^p - s}\right), \tag{4.4}$$

with

$$\varepsilon_{21} = \phi_2 - \phi_1, \qquad \varepsilon_{32} = \phi_3 - \phi_2, \qquad (4.5)$$

$$s = \operatorname{sign}\left(\frac{\varepsilon_{32}}{\varepsilon_{21}}\right). \tag{4.6}$$

The Richardson extrapolated value is:

$$\phi_{\text{conv}} = \phi_1 + \frac{\phi_1 - \phi_2}{r_{21}^p - 1}.$$
(4.7)

Relative errors and the Grid Convergence Index (GCI) were computed as:

$$\varepsilon_{\rm rel}^{21} = \frac{|\phi_1 - \phi_2|}{\phi_1},\tag{4.8}$$

$$GCI_{\text{fine}}^{21} = \frac{F_s \,\varepsilon_{\text{rel}}^{21}}{r_{21}^p - 1},\tag{4.9}$$

with safety factor $F_s = 3$. The numerical uncertainty was taken as

$$u_{\text{num}} = \frac{\text{GCI}}{k}, \qquad k = 2. \tag{4.10}$$

The results obtained for the directed anisotropic mesh configuration, using h_{char} , are presented in Table 4.5.

Table 4.5: Grid convergence and extrapolated results for the first case study

Quantity	Value
$T_{\text{avg,outlet}}$ (Fine), ϕ_1	641.44 °C
$T_{\text{avg,outlet}}$ (Medium), ϕ_2	$640.50~^{\circ}{\rm C}$
$T_{\text{avg,outlet}}$ (Coarse), ϕ_3	$639.91~^{\circ}{\rm C}$
Observed convergence order, p	1.25
Extrapolated temperature, ϕ_{conv}	$641.67~^{\circ}{\rm C}$
GCI_{21}	0.13~%
GCI_{32}	0.35~%

The observed order $p \approx 1.25$ is positive and indicates that the solution is converging, though not at a very high formal order, which is reasonable for complex anisotropic meshes. The GCI values are small (GCI₂₁ $\approx 0.13\%$, GCI₃₂ $\approx 0.35\%$), indicating that mesh refinement has a minor effect on the predicted outlet temperature. Based on these results, the fine mesh was selected for all subsequent results comparison, as it provides a solution within the quoted numerical uncertainty. The two GCI estimates, obtained from the fine–medium and medium–coarse pairs, provide a conservative bracket for the discretization error.

4.1.4 Results

The benchmarking comparison focuses on the outlet, evaluating the average temperature at the surface of the assemblies. Figures 4.5 and 4.6 present the outlet temperature distributions obtained with DASSH and STAR-CCM+, respectively.

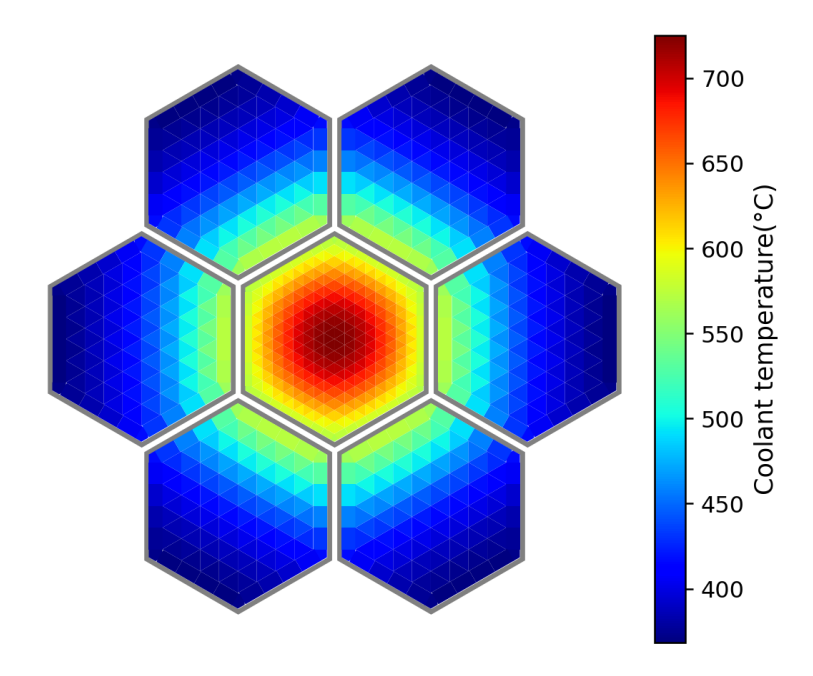


Figure 4.5: Outlet temperature distribution obtained with DASSH.

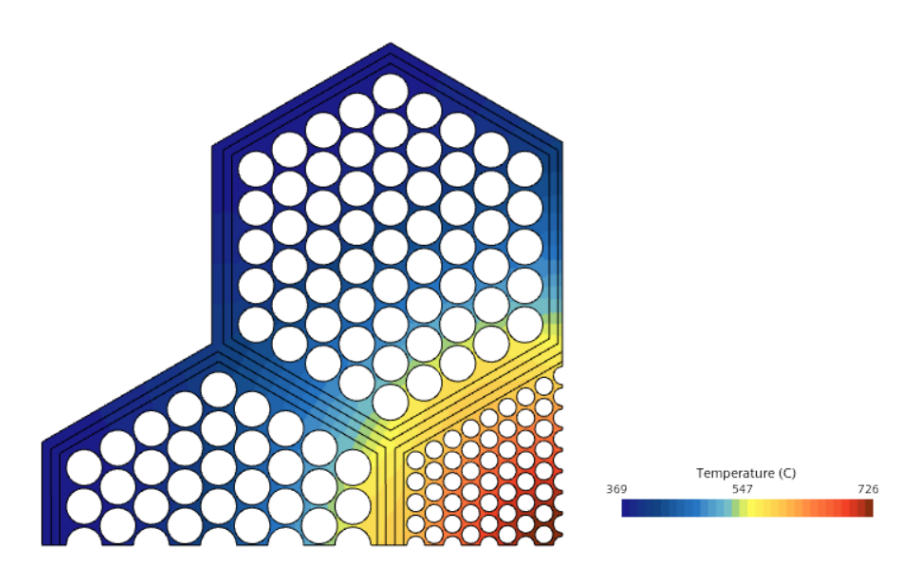


Figure 4.6: Outlet temperature distribution obtained with STAR-CCM+.

These global views confirm the expected trend: the central assemblies reach higher outlet temperatures, while the peripheral ones remain cooler. To better illustrate this, detailed outlet distributions for assemblies 1 and 2 are shown next.

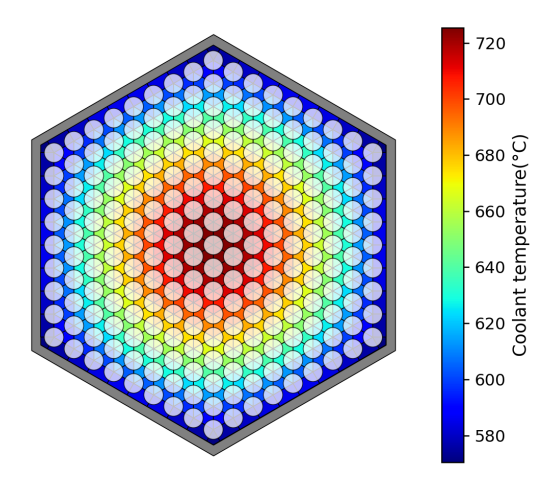


Figure 4.7: Outlet temperature distribution in assembly 1 obtained with DASSH.

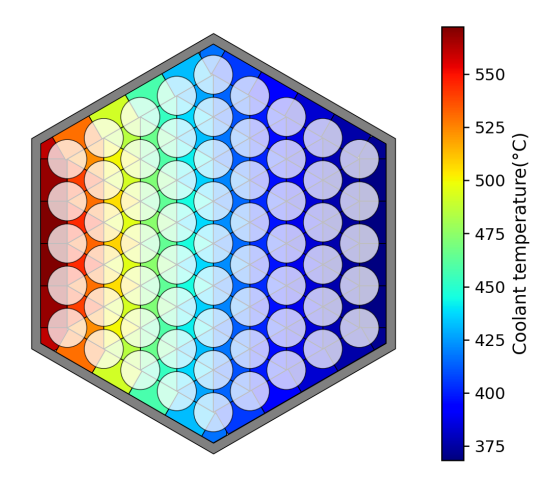


Figure 4.8: Outlet temperature distribution in assembly 2 obtained with DASSH.

For the DASSH solution, assembly 1 exhibits outlet temperatures between $570.44\,^{\circ}\text{C}$ and $725.40\,^{\circ}\text{C}$, while assembly 2 ranges from $368.28\,^{\circ}\text{C}$ to $572.35\,^{\circ}\text{C}$.

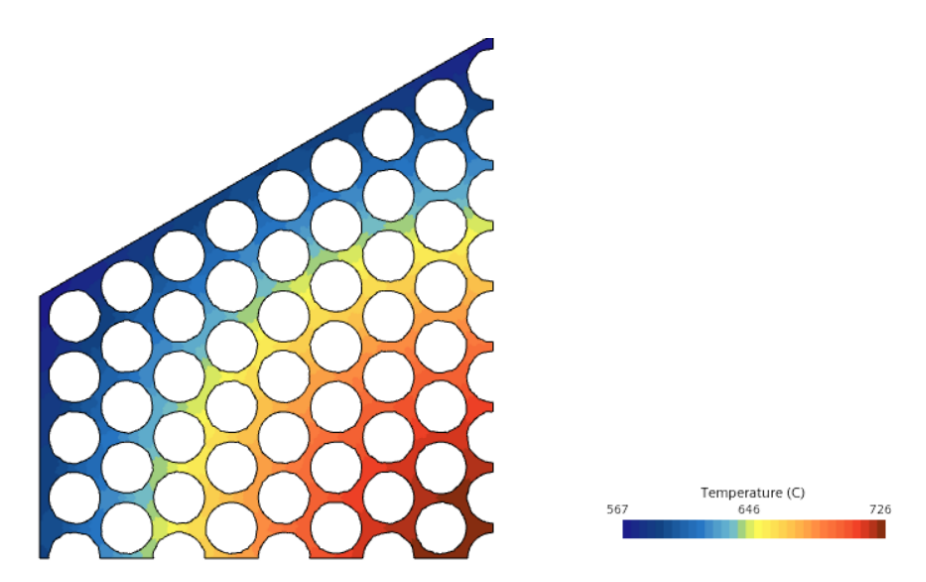


Figure 4.9: Outlet temperature distribution in assembly 1 obtained with CFD.

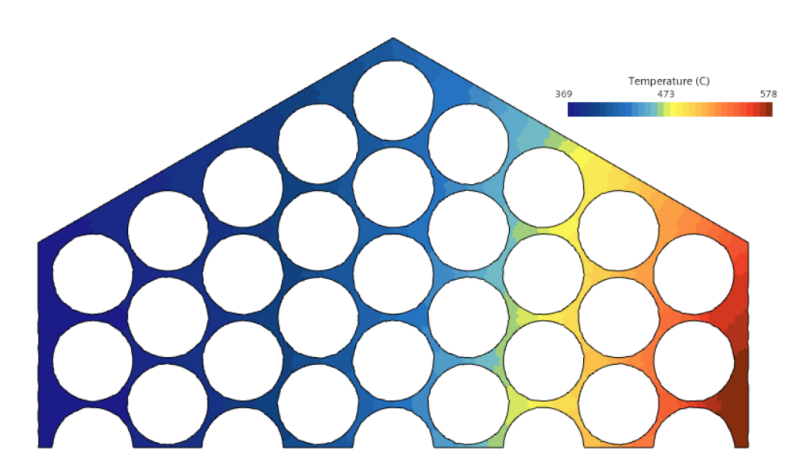


Figure 4.10: Outlet temperature distribution in assembly 2 obtained with CFD.

Similarly, the CFD results show outlet temperatures in assembly 1 ranging from 566.53 °C to 725.51 °C, and in assembly 2 from 368.58 °C to 578.41 °C.

This comparison, even without a detailed subchannel-by-subchannel analysis, highlights that differences between DASSH and CFD predictions arise primarily near the interface between assemblies. Away from this interface, the results remain in very close agreement, as reflected in the minimum (assembly 2) and maximum (assembly 1) values. This observation indicates that the observed discrepancies are largely due to the different numerical approaches of the two methods: DASSH employs a lower-order subchannel-based model, which inherently smooths steep temperature gradients, whereas CFD resolves the full 3D flow and thermal fields. Consequently,

differences are most noticeable in regions with sharp thermal gradients at assembly interfaces.

At the outlet, the expected temperature values from the reference DASSH paper were 635.46 °C for the type 1 assembly and 442.98 °C for assemblies of type 2 to 7. The results obtained in this work are summarized in Table 4.6.

Table 4.6: DASSH outlet temperature.

Assembly type	Outlet temperature (°C)
Type 1	636.25
Type 2–7	442.42

The relative error, calculated as

Relative error (%) =
$$\frac{|T_{\text{DASSH}} - T_{\text{CFD}}|}{T_{\text{CFD}}} \times 100,$$
 (4.11)

is 0.124% for the type 1 assembly and 0.126% for the other assemblies, confirming excellent agreement. These differences are comparable to the numerical uncertainty associated with the chosen mesh and are therefore within the expected discretization error, meaning they cannot be further reduced by refining the grid. Moreover, the shape factor was observed to influence accuracy: adjusting it brings the outlet temperature values closer to the reference solution, suggesting it is the main parameter responsible for small discrepancies.

For the total inter-assembly heat transfer, the expected values were -209.66 kW for the type 1 assembly and 29.62 kW for the other assembly types. The results obtained in this work are very close to these references: type 1 yielded -208.65 kW, while assemblies 2–7 showed 29.44 kW. The total inter-assembly heat transfer was determined using the energy balance formula:

$$Q = \dot{m} c_p \Delta T, \tag{4.12}$$

where \dot{m} is the coolant mass flow rate, c_p the specific heat capacity, and ΔT the temperature rise across the assembly. The relative errors with respect to the reference were 0.48% for type 1 and 0.61% for the other assemblies.

For STAR-CCM+, the reference outlet temperatures were 636.00 °C for type 1 and 438.75 °C for type 2 assemblies. The CFD model developed in this work produced outlet temperatures of 641.44 °C for type 1 and 438.62 °C for type 2. Relative errors are 1.01% for type 1 and 0.03% for type 2. Assembly 3 exactly matches the reference (438.75 °C), but assembly 2 is used as representative for consistency with the original case study [23].

The corresponding total inter-assembly heat transfer values from the CFD simulations were -202.04 kW for type 1 and 28.23 kW for type 2, with relative

errors of 3.32% and 0.14%, respectively. The slightly higher error observed for type 1 assemblies remains well within acceptable limits, whereas the very low error for type 2 assemblies further confirms the robustness and accuracy of the CFD predictions.

Tables 4.7 and 4.8 summarize the averaged outlet temperatures and interassembly heat transfer.

Table 4.7: Case study comparison of outlet temperatures.

Assembly	Axial position	DASSH (°C)	CFD (°C)	Diff. (°C)	Rel. Diff. (%)
Assembly 1	Top	636.25	641.44	-5.19	-0.82
Assembly 2	Top	442.42	438.62	3.80	0.87

Table 4.8: Case study comparison of inter-assembly heat transfer.

Assembly	Axial position	DASSH (kW)	CFD (kW)	Diff. (kW)	Rel. Diff. (%)
From Assembly 1	Top	-208.65	-202.04	-6.61	-3.17
To Assembly 2	Top	29.44	28.23	1.21	4.28

The comparison highlights that DASSH tends to slightly overpredict heat transfer from the central assembly, resulting in a slightly lower temperature for the central assembly and slightly higher temperatures in surrounding assemblies. Despite these differences, overall agreement remains very good, with relative errors below 5%.

It is important to note that even small discrepancies in outlet temperature can produce larger deviations in calculated heat transfer. This amplification arises because the temperature difference ΔT across the assembly is much smaller than the absolute temperatures. Consequently, a minor error in the outlet temperature can propagate into a significant relative error in heat transfer, explaining why the relative errors in heat transfer are larger than those for outlet temperatures.

Midplane comparisons for temperature and inter-assembly heat transfer are reported in Tables 4.9 and 4.10.

Table 4.9: Midplane temperature comparison between DASSH and CFD.

Assembly	Axial position	DASSH T (°C)	CFD T (°C)	Diff. (°C)	Rel. Diff. (%)
Assembly 1	Midplane	674.19	681.28	-7.09	-1.04
Assembly 2	Midplane	420.32	414.94	5.38	1.30

Table 4.10: Midplane heat transfer comparison between DASSH and CFD.

		DASSH Power (kW)	CFD Power (kW)	Diff. (kW)	Rel. Diff. (%)
Assembly 1	Midplane	-160.31	-151.28	-9.03	-5.97
Assembly 2	Midplane	22.40	20.69	1.71	8.26

The overprediction of heat transfer by DASSH is also evident at the midplane, consistent with outlet trends. The discrepancy is larger here, likely due to steep temperature gradients near the inlet, which enhance numerical diffusion effects.

In terms of maximum and minimum, the DASSH results show midplane temperatures in assembly 1 ranging from $578.67\,^{\circ}\text{C}$ to $784.11\,^{\circ}\text{C}$, and in assembly 2 from $352.05\,^{\circ}\text{C}$ to $581.40\,^{\circ}\text{C}$. For the CFD solution, assembly 1 ranges from $572.38\,^{\circ}\text{C}$ to $784.31\,^{\circ}\text{C}$, while assembly 2 spans from $351.87\,^{\circ}\text{C}$ to $590.39\,^{\circ}\text{C}$.

The two approaches therefore agree very well on minimum and maximum temperatures overall, with differences of only a few degrees. As already observed at the outlet, the largest discrepancies occur near the assembly interfaces, where steep thermal gradients amplify the impact of numerical diffusion in DASSH.

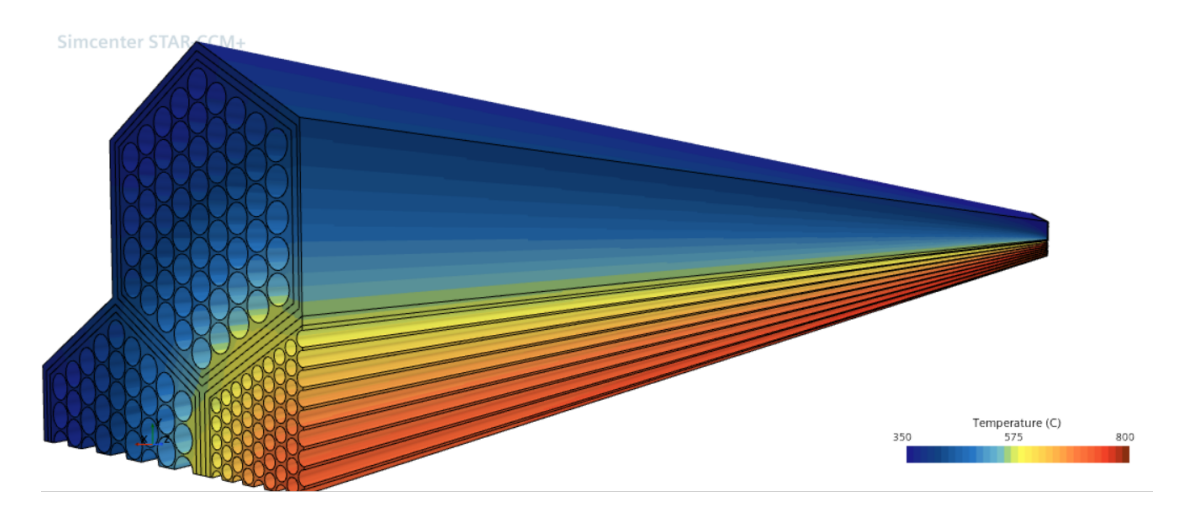


Figure 4.11: Axial temperature profile along the assemblies obtained with STAR-CCM+.

4.1.5 Conclusion

Although the case study developed in this work did not exactly reproduce the reference results, the overall trends and limits of the system were successfully captured. The DASSH approach introduces some numerical diffusion due to its underlying assumptions and simplifications, which tends to slightly overpredict heat transfer, if compared with STAR CCM+, from the central type 1 assembly to the surrounding assemblies (type 2–7).

It is important to note that CFD was considered as a reference solution in this study. However, CFD is inherently affected by modeling approximations; for example, the k- ω SST turbulence model was used here, which may differ from results obtained with more accurate but computationally expensive approaches such as Direct Numerical Simulation or Large Eddy Simulation. Nevertheless, the Grid Convergence Index (GCI) provides an estimate of the numerical uncertainty, indicating that the observed differences remain within acceptable limits.

The main advantage of DASSH remains its computational efficiency. Reliable results are obtained within approximately one minute, depending on the level of axial discretization, whereas STAR-CCM+ required nearly 30000 iterations to reach convergence, corresponding to many hours of runtime on a HPC system in this case, provided by Politecnico di Torino.

In accordance with the findings reported in the DASSH study, it is evident that the system was originally designed to assess code limits, particularly under conditions of high temperature gradients. In practical reactor applications, such extreme conditions are unlikely because the inlet temperature is generally fairly homogeneous, the power distribution is smoother, and wire wraps promote thermal mixing. Under these more realistic conditions, DASSH is expected to perform very well.

In the subsequent case study, DASSH was tested under conditions closer to a realistic reactor system to evaluate its performance in a more practical configuration.

In summary, the present case study demonstrated that DASSH reproduces outlet temperature and heat transfer results within 1–5% of CFD predictions, while achieving a speedup of several orders of magnitude in computational cost. This balance between accuracy and performance suggests that DASSH is particularly well suited for starting design analyses and for uncertainty quantification studies, i.e., investigations in which many simulations are performed to assess how variations in input parameters (such as inlet temperature, power distribution, or coolant properties) affect the overall thermal-hydraulic response. In such cases, the low computational cost of DASSH makes it possible to explore a wide range of operating conditions within practical timeframes. Conversely, CFD remains the preferred tool when detailed local flow and temperature fields are needed or when validation against experimental data must be carried out.

4.2 Case Study 2

This second case study was developed to assess the capability of DASSH in reproducing the thermal—hydraulic behavior of a realistic single fuel assembly. The objective is to evaluate DASSH's reliability under conditions closer to practical research applications, extending beyond the benchmark configuration of the previous

case study. The predictions obtained with DASSH were further verified using a CFD model to ensure their accuracy and consistency.

4.2.1 Fuel Assembly Description

The selected fuel assembly is metallic, based on the ABR-1000 design developed for studies on advanced fast reactor concepts. The main geometrical and design parameters are summarized in Table 4.11.

Table 4.11:	Main geor	netrical fe	atures of	the sel	lected fue	l assembly.
-------------	-----------	-------------	-----------	---------	------------	-------------

Parameter	Value
Number of fuel pins	271
Assembly pitch	$161.42~\mathrm{mm}$
Duct flat-to-flat distance	$157.10~\mathrm{mm}$
Duct wall thickness	$3.94~\mathrm{mm}$
Fuel pin total length	$3327~\mathrm{mm}$
Active core length	813 mm
Fuel pin outer diameter	7.55 mm
Pin pitch-to-diameter ratio (P/D)	1.180
Wire wrap	Not modeled

Temperature-dependent properties are used for both the coolant (sodium) and the structural material (HT9). All correlations are expressed as polynomials of temperature T in Kelvin:

$$\phi(T) = a_0 + a_1 T + a_2 T^2 + a_3 T^3$$

where $\phi(T)$ represents the property of interest (e.g., thermal conductivity, specific heat, density, or viscosity).

For sodium[26]:

$$k(T) = 124.53 - 0.1134 T + 5.474 \times 10^{-5} T^2 - 1.167 \times 10^{-8} T^3$$
 (4.13)

$$c_p(T) = 1592.26 - 0.6696 T + 2.738 \times 10^{-4} T^2 + 5.556 \times 10^{-8} T^3$$
 (4.14)

$$\rho(T) = 983.67 - 0.1355 T - 9.524 \times 10^{-5} T^2 + 2.778 \times 10^{-8} T^3$$
(4.15)

$$\mu(T) = 0.001213 - 2.573 \times 10^{-6} \, T + 2.207 \times 10^{-9} T^2 - 6.667 \times 10^{-13} T^3 \quad (4.16)$$

For HT9 steel [27], the thermal conductivity is defined as a two functions of

temperature:

$$k(T) = \begin{cases} 17.622 + 2.428 \times 10^{-2}T - 1.696 \times 10^{-5}T^{2}, & T \le 1027 \text{ K} \\ 12.027 + 1.218 \times 10^{-2}T, & T > 1027 \text{ K} \end{cases}$$
(4.17)

The inlet temperature was set to 350°C, with mass flow rate and power distribution taken from [18]. The assembly corresponds to the high-power configuration, operating at $7.31~\mathrm{MW_{th}}$ with a mass flow rate of $32.6~\mathrm{kg/s}$. The axial power distribution follows a parabolic shape along the active core length, with power dropping to zero at both the top and bottom of the core.

This setup does not exactly represent a realistic operating scenario, as detailed neutronic information, such as local power variations within the fuel, were not available. Consequently, axial extrapolated boundary effects and fine-scale power variations are not modeled. The primary purpose of this setup is to compare the thermal-hydraulic behavior predicted by DASSH with reference CFD results. The peak power occurs at the midplane of the parabolic profile, as shown in Figure 4.12.

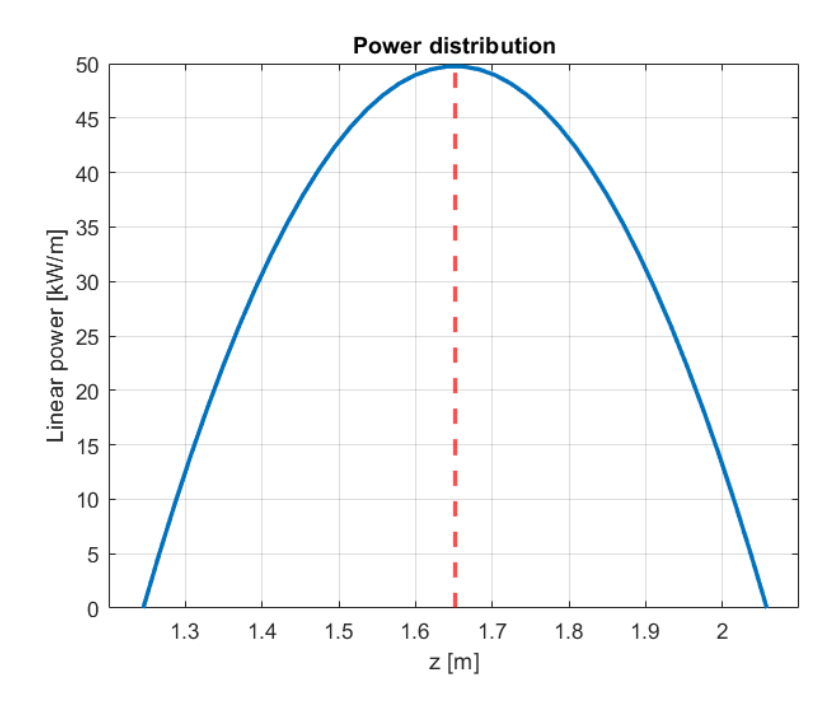


Figure 4.12: Applied parabolic power distribution along the active core length.

4.2.2 DASSH Model

The DASSH model applies the most up-to-date and validated empirical correlations, consistent with those adopted in the initial analyses. The main modeling features

are summarized below:

- Axial Hydraulic Resistance: The axial pressure gradient is determined using the friction factor expression from the upgraded Cheng–Todreas methodology, which incorporates the influence of subchannel geometry on flow resistance.
- Flow Distribution Among Subchannels: Coolant flow allocation within the bundle is evaluated according to the enhanced Cheng—Todreas flow-split formulation, ensuring accurate representation of geometric effects.
- Inter-Subchannel Exchange: Lateral flow and turbulent intermixing between adjacent subchannels are captured using the original Cheng-Todreas correlation. These contributions remain minor in the absence of wire-wrap spacers.
- Convective Heat Transfer: The convective heat transfer coefficient is obtained from a Nusselt number correlation derived from the Lyon–Martinelli relationship.
- Geometric Correction Factor: The hexagonal pin lattice effect is represented by a shape factor of 1.3027, following the Shih–Kuei Cheng correlation.

The axial discretization was 1 mm. The power distribution was normalized between -0.5 and 0.5 according to DASSH requirements obtaining:

$$q(z) = -194169.47 z^2 + 48542.37$$

4.2.3 STAR-CCM+ Model

The CFD model was generated from a SolidWorks CAD import where to reduce computational cost, only 1/6 of the assembly was modeled with periodic boundary conditions then imposed. Using a conjugate heat transfer approach at steady state, solid fuel pins were not modeled explicitly; instead, a field function was used to impose the axial power distribution in the fluid.

For the solid domain, a segregated solid energy solver was used with temperature-dependent properties as previously described. The fluid domain employed the k- ω SST turbulence model with segregated temperature solution and appropriate wall treatment to ensure accurate near-wall resolution, the y+ value obtained has been around 1.1 on average.

Boundary conditions were set as follows: an inlet temperature of 350°C, adiabatic duct walls, and zero outlet pressure. The mesh was generated using the directed mesh approach with a 1 mm base size of polygonal and two prism layers totaling $1 \times$

 10^{-5} m to adequately resolve the viscous sublayer. Axially, 169 layers were adopted to ensure the power distribution was accurately represented and no information was lost due to discretization.

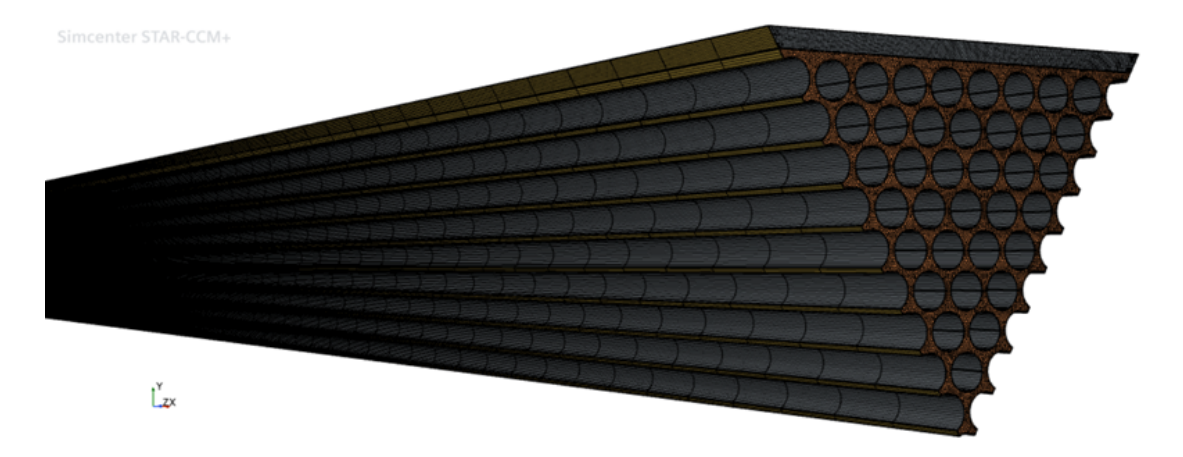


Figure 4.13: Mesh of the fuel assembly used for CFD simulations.

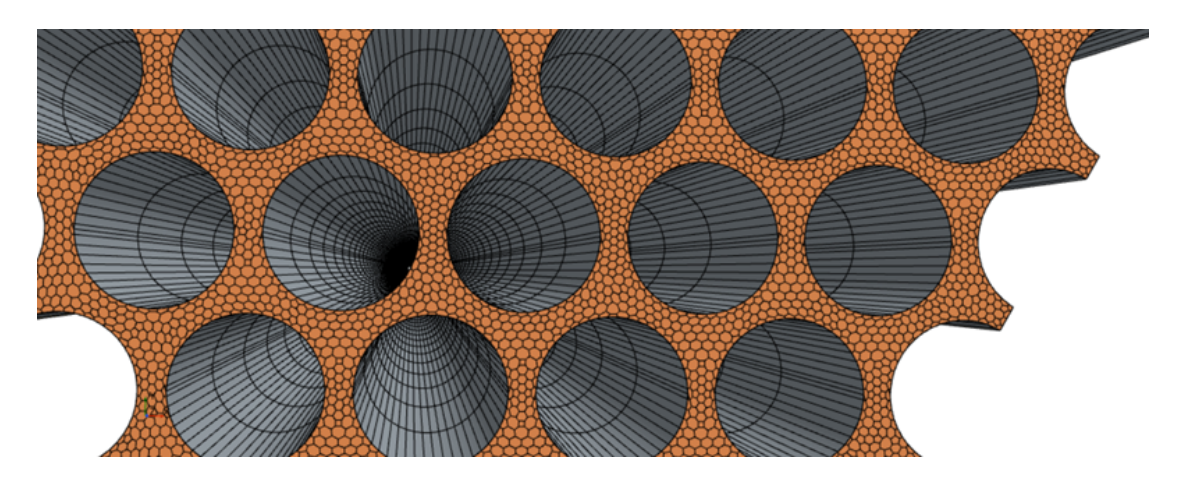


Figure 4.14: Front mesh result

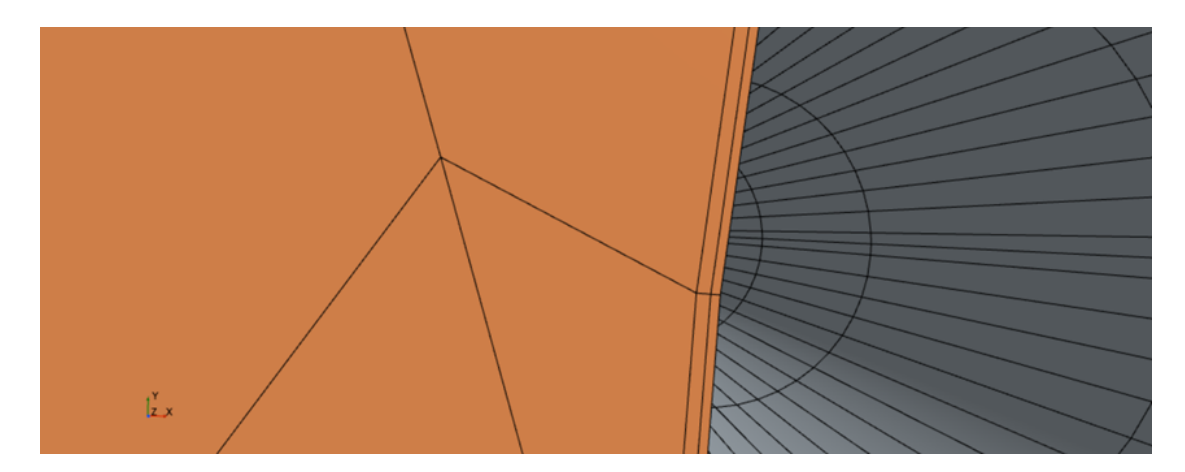


Figure 4.15: Detailed view of the prism layer mesh

Due to discretization effects, the imposed heat flux resulted in a value slightly below the target, which for a 1/6 geometry was approximately 1.22 MW_{th}. The obtained value was slightly lower by 0.12%. This discrepancy should be noted, although the resulting heat loss can be considered negligible over the overall fluid and fuel assembly along its length.

Grid Independence Study

Fine

The analysis was performed by evaluating the numerical results obtained with different mesh resolutions. Three meshes were tested: a coarse, a medium, and a fine mesh. As the mesh base size decreases, the number of cells increases, leading to a higher computational cost. Table 4.12 reports the main parameters and results obtained for each mesh.

Mesh Type	Base size [m]	# Fluid cells	Energy	Continuity
Coarse	5×10^{-3}	1.474694e + 6	0.000135	0.000122
Medium	1×10^{-3}	1.521000e+6	0.00016	0.000142

2.538042e+06

0.000112

0.000131

 5×10^{-4}

Table 4.12: Grid independence results

The analysis focused on evaluating the model error and the overall numerical uncertainty. Richardson extrapolation was employed to estimate the asymptotic values of the scalar quantity of interest, in this case the average outlet temperature.

Since a directed mesh was employed, the grid spacing along the z direction was fixed at 20 mm for all cases (related to the 169 axial layers), while the refinement was applied only in the x-y plane through the base size variation. This configuration leads to an anisotropic mesh, where the characteristic element size differs between

directions. To properly account for this anisotropy, the characteristic mesh size h_{char} was defined as the geometric mean of the local grid spacings:

$$h_{\text{char}} = (\Delta x \, \Delta y \, \Delta z)^{1/3} \tag{4.18}$$

Given that Δz remained constant, variations in h_{char} mainly reflect the refinement in the x-y directions. This definition ensures that the mesh ratios between successive grids correctly represent the effective global refinement. The mesh ratios are defined as:

$$r_{21} = \frac{h_2}{h_1}, \qquad r_{32} = \frac{h_3}{h_2} \tag{4.19}$$

where $h_1 < h_2 < h_3$ are the characteristic mesh sizes of the fine, medium, and coarse grids, respectively.

The observed order of convergence p is evaluated iteratively as:

$$p = \frac{1}{\ln(r_{21})} \left[\ln\left(\frac{\varepsilon_{32}}{\varepsilon_{21}}\right) + q(p) \right], \quad q(p) = \ln\left(\frac{r_{21}^p - s}{r_{32}^p - s}\right)$$
(4.20)

with

$$\varepsilon_{21} = \phi_2 - \phi_1, \qquad \qquad \varepsilon_{32} = \phi_3 - \phi_2, \qquad (4.21)$$

$$s = \operatorname{sign}\left(\frac{\varepsilon_{32}}{\varepsilon_{21}}\right) \tag{4.22}$$

The Richardson extrapolated value is then obtained as:

$$\phi_{\text{conv}} = \phi_1 + \frac{\phi_1 - \phi_2}{r_{21}^p - 1} \tag{4.23}$$

The relative error between successive meshes and the Grid Convergence Index (GCI) are computed as:

$$\varepsilon_{\rm rel}^{21} = \frac{|\phi_1 - \phi_2|}{\phi_1},\tag{4.24}$$

$$GCI_{\text{fine}}^{21} = \frac{F_s \, \varepsilon_{\text{rel}}^{21}}{r_{21}^p - 1}$$
 (4.25)

where $F_s = 3$ is a safety factor for conservative estimates. The numerical uncertainty is then calculated as:

$$u_{\text{num}} = \frac{\text{GCI}}{k}, \quad k = 2 \tag{4.26}$$

The results for the directed anisotropic mesh, considering h_{char} , are summarized in Table 4.13.

Table 4.13: Results for grid independence analysis (directed mesh, h_{char} considered)

	$T_{\text{avg,outlet}}$ [°C]
ϕ_1 (Fine)	526.02
ϕ_2 (Medium)	525.81
ϕ_3 (Coarse)	525.30
\overline{p}	1.28
$\phi_{ m conv}$	526.17
GCI_{21}	0.44%
GCI_{32}	0.25%

A positive and realistic convergence order (p=1.28) confirms that the solution is in the asymptotic range of convergence. The small GCI values indicate that mesh refinement has a negligible influence on the computed outlet temperature, demonstrating that the results are grid independent within the estimated numerical uncertainty.

4.2.4 Results

Outlet temperature results obtained from DASSH and STAR-CCM+ are presented in Figures 4.16 and 4.17.

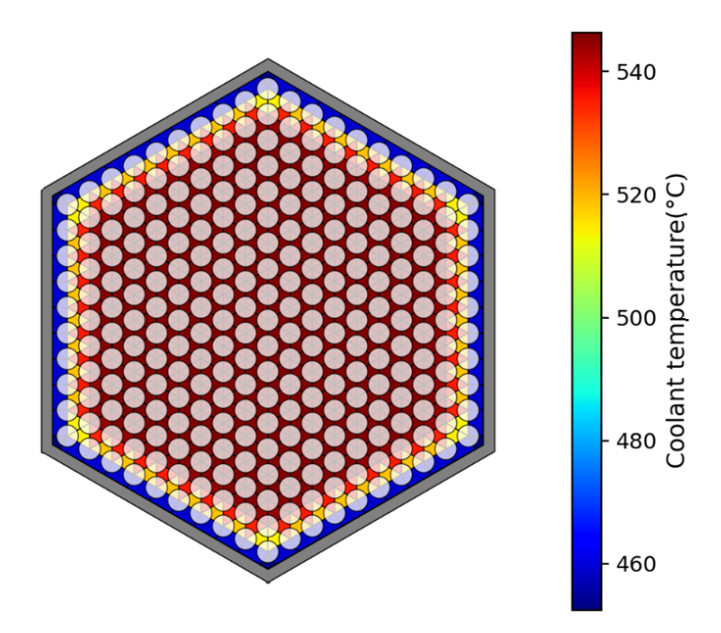


Figure 4.16: Outlet temperature distribution predicted by DASSH.

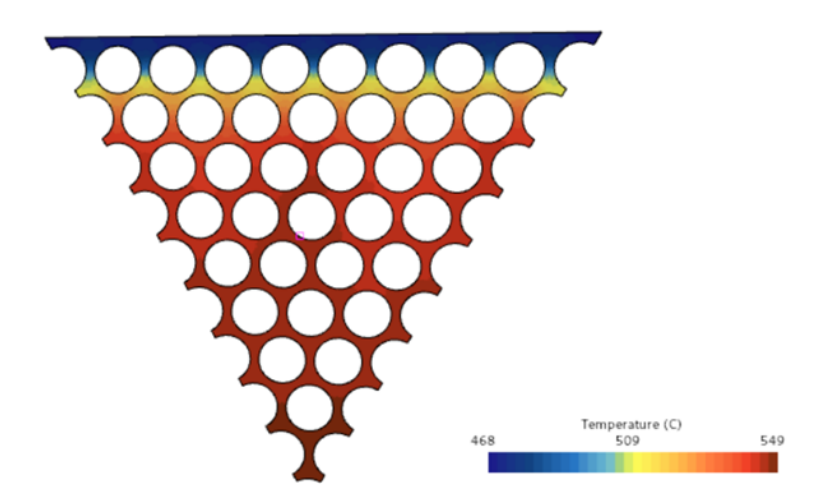


Figure 4.17: Outlet temperature distribution predicted by STAR-CCM+.

Table 4.14: Comparison of outlet temperature results between DASSH and CFD (STAR-CCM+).

Parameter	DASSH	CFD	Relative Error (%)
Average outlet temperature (°C)	525.46	526.02	0.11
Minimum temperature (°C)	452.57	467.81	3.26%
Maximum temperature (°C)	546.46	549.23	0.50%

The average outlet temperatures predicted by both codes are in close agreement, with a difference of only 0.56°C (0.11% relative error). This indicates that DASSH and the CFD simulation produce comparable overall thermal predictions for the assembly. The temperature ranges obtained by the two approaches show minor differences, which may be attributed to the different spatial resolutions: DASSH uses a coarser subchannel discretization, while the CFD model employs a finer mesh with full 3D resolution of turbulence effects. These differences illustrate the expected variations between the two modeling approaches, indicating that, overall, DASSH provides a reliable representation of the assembly's thermal—hydraulic behavior while capturing the key trends predicted by the more detailed CFD.

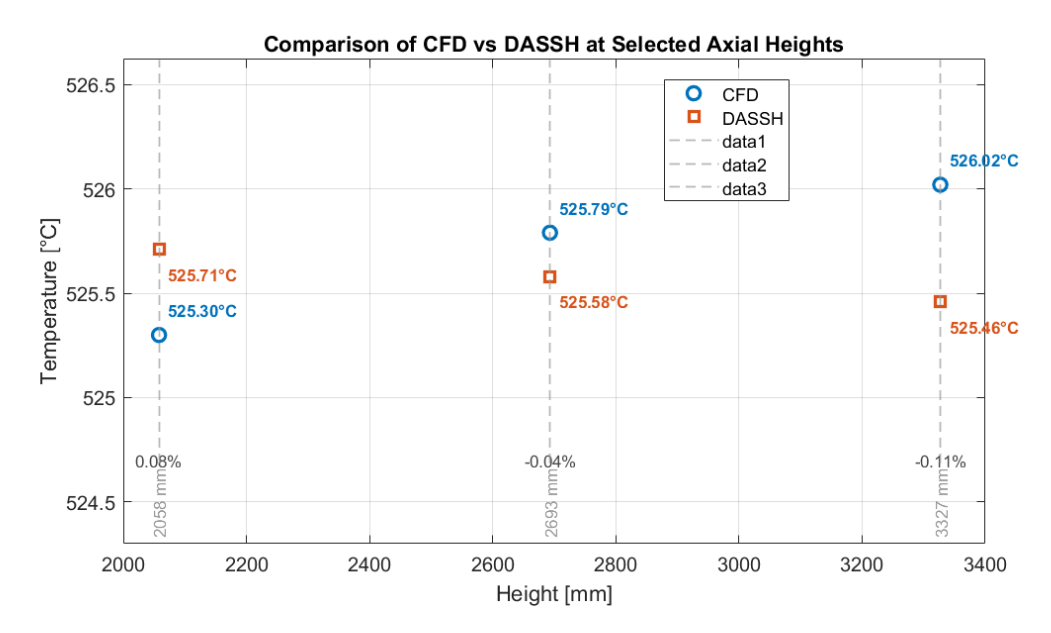


Figure 4.18: Comparison of temperature profiles at heights of 2.058 m, 2.693 m, and 3.327 m.

Figure 4.18 compares the axial evolution of the outlet temperature predicted by DASSH and STAR-CCM+ at three representative heights along the fuel assembly: immediately after the end of the active core pins (z=2.058 m), at the midpoint between the pin end and the outlet (z=2.693 m), and at the assembly outlet (z=3.327 m). The figure shows that the temperature predictions from both codes are in close agreement at all heights, with only minor differences.

Overall, both models exhibit excellent agreement, with temperature differences remaining below 0.6 °C at all axial positions. However, a small but systematic discrepancy in the temperature trend can be observed. In the DASSH results, the outlet temperature shows a slightly decreasing trend along the channel, whereas the STAR-CCM+ predictions indicate a modest increase.

This difference can be attributed to the distinct thermal modeling approaches used in the two codes. DASSH employs a subchannel formulation in which the convective heat transfer and axial conduction are simplified, leading to an averaged temperature field that can slightly underestimate heat accumulation in the upper region of the channel. Conversely, the CFD model resolves the three-dimensional velocity and temperature fields and accounts for local turbulent mixing, which promote a gradual upward transport of thermal energy. As a result, STAR-CCM+predicts a slight temperature rise toward the outlet, consistent with the continuous accumulation of heat from the fuel pins and the more effective downstream advection of energy in the main flow direction.

In addition to the axial temperature evolution, the radial temperature profile at

the outlet is also consistent between the two models as showed in Figure 4.16 and 4.17. Both DASSH and STAR-CCM+ predict the highest temperatures near the central region of the assembly, where the power density and heat generation are greatest, while the temperature gradually decreases toward the outer subchannels. This trend reflects the expected radial heat transfer behavior, in which coolant near the periphery experiences enhanced heat removal due to greater contact with the assembly duct wall. The agreement confirms that DASSH correctly reproduces the location of the hot spot at the assembly center and captures the overall radial temperature distribution, although CFD provides finer resolution of local gradients near the boundary. The temperature difference between the central and outermost subchannels, estimated from the maximum and minimum outlet temperatures, is approximately 93.9°C in DASSH and 81.4°C in STAR-CCM+, representing relative differences consistent with the expected trends for subchannel-level predictions.

The radial temperature variation at the outlet was quantified using the following formula:

Radial variation (%) =
$$\frac{T_{\text{max}} - T_{\text{min}}}{T_{\text{avg}}} \times 100$$
 (4.27)

where $T_{\rm max}$ and $T_{\rm min}$ are the maximum and minimum outlet temperatures, respectively, and $T_{\rm avg}$ is the average outlet temperature. Using this expression, the radial temperature variation is approximately 17.9% for DASSH and 15.5% for STAR-CCM+, with the highest temperatures at the assembly center and the lowest near the outer subchannels. This indicates that DASSH predicts a slightly wider temperature spread, consistent with its coarser subchannel discretization and reduced resolution of local thermal mixing.

From a benchmarking perspective, these results confirm that DASSH reliably captures the global and local thermal behavior of the fuel assembly. The subchannel-based predictions reproduce the same physical trends observed in the CFD results—both axially and radially—with only minor deviations associated with turbulence modeling and geometric effect simplification. The overall agreement supports the suitability of DASSH as a fast-running tool for even detailed thermal analysis, offering a substantial reduction in computational cost while preserving predictive accuracy for engineering applications.

Chapter 5

Conclusions

This thesis presented a benchmarking study aimed at verify the thermo-hydraulic reliability and predictive capabilities of the DASSH software in comparison with CFD simulations performed using STAR-CCM+. The overarching goal was to verify the extent to which DASSH can reproduce key thermal and hydraulic parameters in ducted hexagonal fuel assemblies, which are typical of advanced reactor designs, while maintaining a reasonable balance between computational efficiency and physical accuracy.

DASSH was developed at Argonne National Laboratory as an subchannel code intended to simulate steady-state temperature distributions and coolant flow within hexagonally ducted fuel assemblies. Its primary advantage lies in its computational efficiency and scalability, which make it particularly suitable for corewide analyses and design optimization. However, its simplified treatment of certain flow and turbulence effects, as well as its empirical correlations, necessitates careful verification against more detailed methods such as CFD. This thesis addressed that need through two representative case studies.

In the first case study, a configuration characterized by steep temperature gradients at inlet was examined to challenge the code's robustness and to assess the influence of numerical diffusion on its thermal predictions. The results demonstrated very good agreement between DASSH and STAR-CCM+, with only minor deviations in outlet temperature and flow parameters. This confirmed that DASSH can accurately reproduce the overall thermal field even under demanding conditions, where strong gradients might otherwise amplify diffusion-related errors.

The second case study investigated a more realistic fuel assembly configuration, in which a representative axial power distribution was imposed. The objective was to evaluate DASSH performance in simulating the temperature field within an operationally relevant environment. The comparison again revealed excellent consistency between DASSH and CFD, with average outlet temperature differences below 1 °C and a relative error of approximately 0.1%. Minor discrepancies were

attributed to the different levels of spatial resolution and turbulence modeling inherent in the two approaches.

A qualitative comparison of axial temperature trends further clarified these differences. While STAR-CCM+ predicted a slight temperature increase toward the outlet, DASSH exhibited a modest decreasing trend. This contrast was explained by the different modeling philosophies: CFD explicitly resolves local velocity and temperature fields, capturing three-dimensional turbulent transport and secondary flows, whereas DASSH employs a subchannel formulation that simplifies axial conduction and mixing. Despite this, the two codes displayed a consistent global thermal pattern, confirming that DASSH's simplified approach remains reliable for steady-state assessments.

The findings of this benchmarking study demonstrate that DASSH can effectively reproduce the main thermo-hydraulic behaviors predicted by CFD, while offering a much lower computational cost. This makes it an attractive option for early-stage reactor design studies, parametric analyses, and system-wide evaluations where rapid feedback and iterative optimization are required. CFD, on the other hand, remains indispensable for detailed investigations of local flow features, turbulence, and high temperature gradients.

Looking forward, several possible improvements to DASSH could further enhance its performance and accuracy. Future development may focus on optimizing computational speed by refactoring the solver to perform grouped calculations for assemblies of the same type, improving the treatment of homogenized regions to better represent cross-assembly heat transfer, and refining the flow split model for control assemblies to more accurately capture hydraulic behavior. Implementing these upgrades would strengthen DASSH's numerical stability and accuracy, making it even more competitive with higher accuracy CFD tools while preserving its computational efficiency. Additionally, future work could extend the benchmarking to experimental datasets and explore the coupling of DASSH with neutronics solvers, enabling integrated reactor system analyses and further validating its predictive capabilities.

In conclusion, this thesis successfully verify the performance of DASSH against CFD simulations, confirming its capability to provide accurate, consistent, and computationally efficient thermal-hydraulic predictions for ducted fuel assemblies. The results underline the complementary nature of DASSH and CFD: while CFD remains the reference tool for detailed local studies, DASSH offers a fast and reliable platform for global system analyses. Together, they form a robust and synergistic framework for the design and safety evaluation of future nuclear systems.

Bibliography

- [1] Milos Atz, Micheal A. Smith, and Florent Heidet. «DASSH software for ducted assembly thermal hydraulics calculations overview and benchmark». In: (Nov. 2020). URL: https://www.researchgate.net/publication/357575432_DASSH_software_for_ducted_assembly_thermal_hydraulics_calculations_-_overview_and_benchmark.
- [2] A.P. Sorokin, A.D. Efanov, Yu.S. Yuriev, A.V. Zhukov, P.A. Ushakov, and G.P. Bogoslovskaya. *Methods and codes for modeling thermohydraulic of fast reactor core subassemblies under nominal and non-nominal operating conditions*. Tech. rep. Institute of Physics and Power Engineering, Obninsk, Kaluga Region, Russian Federation, June 2000. URL: Available%20at:https://inis.iaea.org/records/azthr-mvk85.
- [3] Generation IV International Forum. Generation IV Official Website. URL: https://www.gen-4.org/.
- [4] Dave Van Haaften, Sue Turner, Ivonne Ingvarsson, Kirby Whitham, and Dick Blackledge. «Experimental Breeder Reactor I Idaho National Engineering Laboratory». In: *The American Society of Mechanical Engineers* (June 1979). URL: https://www.asme.org/wwwasmeorg/media/resourcefiles/aboutasme/who%20we%20are/engineering%20history/landmarks/39-experimental-breeder-reactor-i-1951.pdf.
- [5] Leonard J. Koch. Experimental Breeder Reactor-II (EBR-II)—An Integrated Experimental Fast Reactor Nuclear Power Station. Tech. rep. Argonne National Laboratory, 2004. URL: https://publications.anl.gov/anlpubs/2004/03/49168.pdf.
- [6] T. Sumner and T.Y.C. Wei. Benchmark Specifications and Data Requirements for EBR II Shutdown Heat Removal Tests SHRT-17 and SHRT-45R. Tech. rep. Argonne National Laboratory, May 2012. URL: https://publications.anl.gov/anlpubs/2012/06/73647.pdf.

- [7] G.L. Lentz, H.W. Buschman, R.N. Smith, and Argonne National Lab. «EBR-II: twenty years of operating experience». In: *International symposium on fast breeder reactors -experience and future trends* (1985). URL: https://inis.iaea.org/records/jd1d0-rmh11.
- [8] A. Mohamed T. Fei and T. K. Kim. Neutronics Benchmark Specifications for EBR-II Shutdown Heat Removal Test SHRT-45R Revision 1. Tech. rep. Argonne National Laboratory, Jan. 2013. URL: https://publications.anl.gov/anlpubs/2018/05/143362.pdf.
- [9] Joël Guidez, Bruno Fontaine, and Marc Vanier. Fast Reactor Operation and Reactivity Control: Report on the Phenix Experience. Tech. rep. Sept. 2008. URL: https://www.researchgate.net/publication/272484972_Fast_Reactor_Operation_and_Reactivity_Control_Report_on_the_Phenix_Experience.
- [10] et al Catherine Andrieux François Baqué. Sodium-Cooled Nuclear Reactors. Tech. rep. Commissariat à l'énergie atomique et aux énergies alternatives, 2013. URL: https://www.cea.fr/english/Pages/resources/nuclear-energy-monographs/sodium-cooled-nuclear-reactors.aspx.
- [11] V.I. Matveev, A.N. Chebeskov, and I.Y. Krivitsky. «Core concept of fast power reactor with zero sodium void reactivity». In: *IAEA* (1991). URL: https://inis.iaea.org/records/1s9ve-mmx08.
- [12] Takashi Ashida, Yoji Gondai, Masaki Inoue, and et al. «2 Experimental reactor Joyo». In: Sodium-cooled Fast Reactors. Ed. by Masaki Morishita and Hiroyuki Ohshima. Vol. 3. JSME Series in Thermal and Nuclear Power Generation. Academic Press, 2022, pp. 9–85. DOI: https://doi.org/10.1016/B978-0-12-824076-2.00002-X. URL: https://www.sciencedirect.com/science/article/pii/B978012824076200002X.
- [13] Stephen Neethu Hanna, G Raghukumar, N Manimaran, G Shanmugam, and K.V. Suresh Kumar. «A STUDY ON THE POWER VARIATION OF FUEL SUBASSEMBLIES CLOSER TO THE SOURCE SUBASSEMBLY OF THE 40MWT FBTR CORE». In: Nuclear and Particle Physics Proceedings 342 (2024), pp. 7–9. URL: https://www.sciencedirect.com/science/article/pii/S2405601423002638.
- [14] H. Chen et al. «OVERVIEW ON NEW RESEARCH REACTORS IN CHINA» In: (). URL: https://www-pub.iaea.org/MTCD/publications/PDF/P1575_CD_web/datasets/papers/C2%20Chen.pdf.

- [15] C.E. Till, Y.I. Chang, and W.H. Hannum. «The intergral fast reactor-an overview». In: *Progress in Nuclear Energy* 31.1 (1997). The Technology of the Integral Fast Reactor and its Associated Fuel Cycle, pp. 3–11. ISSN: 0149-1970. DOI: https://doi.org/10.1016/0149-1970(96)00001-7. URL: https://www.sciencedirect.com/science/article/pii/0149197096000017.
- [16] ERIC P. LOEWEN BRIAN S. TRIPLETT and BRETT J. DOOIES. «PRISM: A COMPETITIVE SMALL MODULAR SODIUM-COOLED REACTOR». In: 178 (2012). URL: https://www.gevernova.com/content/dam/gevernova-nuclear/global/en_us/documents/prism-technical-paper.pdf.
- [17] TerraPower. THE NEXT GENERATION OF POWER IS HERE. 2025. URL: https://www.terrapower.com/natrium/.
- [18] J. Cahalan et al. Advanced Burner Reactor 1000MWth Reference Concept. Tech. rep. Argonne National Lab. (ANL), Argonne, IL (United States), Sept. 2007. DOI: 10.2172/1349893. URL: https://publications.anl.gov/anlpubs/2017/04/134264.pdf.
- [19] Carriean Stocks. «France cancels ASTRID fast reactor project». In: Nuclear Engineering International (2019). URL: https://www.neimagazine.com/news/france-cancels-astrid-fast-reactor-project-7394432/.
- [20] Iurii ASHURKO. «Implementation of Safety Design Criteria in the Large Power Size Sodium Cooled Fast Reactor BN-1200 Design». In: 2018. URL: https://inis.iaea.org/collection/NCLCollectionStore/_Public/49/059/49059971.pdf.
- [21] IAEA. STATUS OF INNOVATIVE FAST REACTOR DESIGNS AND CON-CEPTS. 2013. URL: https://aris.iaea.org/Publications/booklet-fr-2013.pdf.
- [22] Milos Atz, Micheal A. Smith, and Florent Heidet. *Ducted Assembly Steady-State Heat Transfer Software (DASSH) Theory Manual.* Nuclear Engineering Division, Argonne National Laboratory. Aug. 2021. URL: https://publications.anl.gov/anlpubs/2021/08/169971.pdf.
- [23] Milos Atz and SuJong Yoon. Summary of DASSH-CFD Inter-Assembly Heat Transfer Comparison. Nuclear Science and Engineering Division, Argonne National Laboratory with Idaho National Laboratory. Aug. 2021. URL: https://publications.anl.gov/anlpubs/2022/12/176053.pdf.
- [24] et all A. Grannan D. Lisowski. Final Report on Full Length Assembly Testing in PELICAN. Tech. rep. U.S. Department of Energy (DOE), 2022. URL: https://publications.anl.gov/anlpubs/2023/02/181073.pdf.

- [25] Shih-Kuei Cheng. Constitutive correlations for wire-wrapped subchannel analysis under forced and mixed convection conditions. Technical Report. Cambridge, MA: Massachusetts Institute of Technology, 1984. URL: https://dspace.mit.edu/handle/1721.1/15343.
- [26] J K Fink and L Leibowitz. Thermodynamic and transport properties of sodium liquid and vapor. Tech. rep. Argonne National Laboratory (ANL), Argonne, IL, Jan. 1995. URL: https://cardinal.cels.anl.gov/source/fluidproperties/SodiumProperties.html.
- [27] L. Leibowitz and R. A. Blomqui. hermal Conductivity and Thermal Expansion of Stainless Steels DO and HT9. Tech. rep. Argonne National Laboratory. URL: https://inis.iaea.org/records/shxw8-s8538.
- [28] Milos Atz, Micheal A. Smith, and Florent Heidet. Ducted Assembly Steady-State Heat Transfer Software (DASSH) – User Guide. Nuclear Engineering Division, Argonne National Laboratory. Aug. 2021. URL: https://publications.anl.gov/anlpubs/2021/08/169972.pdf.
- [29] Micheal A. Smith. DASSH-F: Subchannel Based Thermal Analysis. Nuclear Engineering Division, Argonne National Laboratory. Dec. 2024. URL: https://publications.anl.gov/anlpubs/2025/01/193632.pdf.
- [30] Milos Atz and Florent Heidet. Implementation of an Orificing Optimization Algorithm in the DASSH Subchannel Analysis Code. Nuclear Science and Engineering Division Argonne National Laboratory. Mar. 2022. URL: https://publications.anl.gov/anlpubs/2022/11/178011.pdf.
- [31] International Atomic Energy Agency. Small Modular Reactors: Advances in SMR Developments 2024. Tech. rep. International Atomic Energy Agency, Oct. 2024. URL: https://www-pub.iaea.org/MTCD/Publications/PDF/p15790-PUB9062_web.pdf.
- [32] Idaho National Laboratory. Experimental Breeder Reactor-I. URL: https://inl.gov/ebr/.
- [33] IAEA. From Obninsk Beyond: Nuclear Power Conference Looks to Future. July 2017. URL: https://www.iaea.org/newscenter/news/obninsk-beyond-nuclear-power-conference-looks-future.
- [34] IAEA. LIQUID METAL COOLED REACTORS: EXPERIENCE IN DESIGN AND OPERATION. Tech. rep. IAEA, 2007. URL: https://www-pub.iaea.org/MTCD/publications/PDF/te_1569_web.pdf.
- [35] G. Shanmugam, A. Babu, and K.V. Suresh Kumar. «Operating Experiences of FBTR». In: (2017). URL: https://inis.iaea.org/records/j1a89-qxk54.
- [36] HEXANA. Technology. 2025. URL: https://www.hexana.com/technology/.

BIBLIOGRAPHY

[37] Generation IV International Forum. Sodium Fast Reactor (SFR). 2024. URL: https://www.gen-4.org/generation-iv-criteria-and-technologies/sodium-fast-reactor-sfr.